DEVELOPMENT OF SILICA BASED NANOPARTICLES FOR MULTIMODAL THERAPEUTIC DELIVERY

by

Hemapriyadarshini Vadarevu

A dissertation submitted to the faculty of
The University of North Carolina at Charlotte
in partial fulfillment of the requirements
for the degree of Doctor of Philosophy in
Nanoscale Science

Charlotte

2022

Approved by:

_____
Dr. Juan L. Vivero-Escoto

_____
Dr. Kirill Afonin

_____
Dr. Jerry Troutman

_____
Dr. Richard Chi

_____
Dr. Susan Trammell

_____
Dr. Yuri Nesmelov

ABSTRACT

HEMAPRIYADARSHINI VADAREVU.

Development of Silica Based Nanoparticles for Multimodal Therapeutic Delivery

(Under the direction of Dr. JUAN L. VIVERO-ESCOTO)

Chronic diseases like cancer are characterized by complex interactions between multiple pathways leading to treatment resistance and invasiveness. Repeated cycles of cytotoxic monotherapies are susceptible to drug resistance induced by the upregulation of cytoprotective genes. Some common mechanisms that promote sustenance of cancer include hypoxia, antioxidant response, anti-apoptotic protein synthesis, angiogenesis, and metastatic potential. Combinations that rely on different therapeutic approaches such as chemo, photodynamic and gene therapy with independent mechanisms of action remarkably enhance the therapeutic efficacy against cancer. In addition, downregulation of survival mechanisms alongside administration of mainstay cytotoxic treatments is a promising strategy for combination therapy.

The main challenge behind the use of combination therapy is the lack of efficient delivery systems that allows the spatiotemporal release required for co-delivery of multiple therapeutic agents. Recently, nanoparticulate delivery system have become a successful alternative for making stable formulations of multiple drugs and for the protection of nucleic acid therapeutics against enzymatic degradation. In particular, silica-based nanoparticles (SiNP) can be engineered to carry different types of therapeutic agents, to enhance the target-specificity and to avoid side effects associated with the drugs. The design, synthesis and characterization of mesoporous silica and hybrid organosilica nanoparticles comprising bimodal combinations of small molecule drugs, photosensitizers (PSs), and/or siRNA, are discussed in this Thesis. The therapeutic performance of the synthesized nanomedicines is evaluated in cancer cell lines.

ACKNOWLEDGEMENTS

I express my gratitude to Dr. Juan Vivero-Escoto for supporting my PhD study. I also would like to thank Dr Mubin Tarannum for her patience while I was learning the ropes and her remarkable mentorship ever since I joined V-lab. To my lab mates who became good friends Mubin, Paolo, and Zaneta; thanks for sharing the agonies of failed experiments and celebrating small successes every so often. Many thanks to the faculty and staff of the Chemistry Department the UNC Charlotte. I would like to thank Dr. Afonin, Dr. Chi, Dr. Troutman, Dr. Trammell, and Dr. Nesmelov for serving as my dissertation committee.

Thanks to the financial support from the National Science Foundation (EAGER-NSF #1835688), UNC Research Opportunities Initiative, Livingstone Endowment and Thomas Reynolds Graduate Research Award. Thanks also to UNC Charlotte Graduate School for GASP support.

A big thank you to my mother Vani, father Venkataramana and my sister Swetha for being my constants and supporting me. My friends Vinita, Jagathshree, Purti, Medha and Bhargav for just being there patiently and lifting my spirits every time I needed a push. Thank you Christopher Cook and Erina Cook, for being my home away from home. This work is dedicated to my uncle, T V K Raju Bharatam. Thanks for being an inspiration.

TABLE OF CONTENTS

LIST OF FIGURES

LIST OF TABLES

LIST OF ABBREVIATIONS

AFM	Atomic Force Microscopy
Ago2	Argonaute 2
AOT	Aerosol-T
APS	1-(2-aminopropyl) silatrane
APTES	3-aminopropyl triethoxysilane
ATF	Activating Transcription Factor
ATG	Autophagy related gene
Bcl2	B-cell lymphoma 2
BET	Brunauer–Emmett–Teller
BJH	Barrett, Joyner, and Halenda
Cas9	CRISPR-associated protein 9
cDNA	complementary DNA
Ce6	Chlorin e6
CLSM	Confocal Laser Scanning Microscopy
cNA	cube nucleic acid nanoparticle
CRISPR	Clustered regularly interspaced short palindromic repeats
CTAB	cetyltrimethylammonium bromide
DCF	Dichlorodihydrofluorescein
DCFDA	Dichlorodihydrofluorescein diacetate
DCM	Dichloromethane
DHA	dehydroalanine
DIPEA	N, N-Diisopropylethylamine

DLS	Dynamic Light Scattering
DMA	9,10-dimethylanthracene
DMEM	Dulbecco's Modified Eagle Medium
DMF	Dimethylformamide
DMSO	Dimethyl Sulfoxide
DNA	Deoxyribonucleic acid
DOX	Doxorubicin
Dp44mT	2,2′-Dipyridyl-N,N-dimethylsemicarbazone
dsDNA	Double-stranded DNA (dsDNA)
dsRNA	Double-stranded RNA (dsRNA)
DTT	Dithiothreitol
ECM	Extra cellular matrix
EDC	1,2-dichloroethane
EGFR	Epidermal growth factor receptor
EPR	enhanced permeability and retention effect
FBS	Fetal bovine serum
FITC	Fluorescein isothiocyanate
fNA	Fiber Nucleic acid nanoparticle
GADPH	Glyceraldehyde 3-phosphate Dehydrogenase
GEM	Gemcitabine
GFP	Green Fluorescent Protein
GpX	Glutathione peroxidase
GSH	Glutathione

GSSG	oxidized glutathione
HEK	Human embryonic kidney
HIF 1α	Hypoxia-inducible factor 1-alpha
HSF1	Heat shock factor 1
IFN	Interferon
LED	Light Emitting Diode
LMP	Lysosomal membrane permeabilization
MALDI	Matrix-assisted laser desorption/ionization
MDA	Malondialdehyde
MDR	Multi-Drug Resistance
MFI	Mean Fluorescence Intensity
miRNA	micro-RNA
mRNA	messenger RNA
MSN or	
MSNP	Mesoporous silica nanoparticle
MTS	3-(4,5-dimethylthiazol-2-yl)-2,5-diphenyl tetrazolium bromide
NADPH	Reduced nicotinamide adenine dinucleotide phosphate
NHS	NHS (N-hydroxysuccinimide)
NIR	Near-infrared
NMR	Nuclear Magnetic Resonance
NP	Nanoparticle
NRF2	nuclear transcription factor
p62/SQSTM1	sequestosome 1

PBS	Phosphate Buffer Saline
PdI	Polydispersity index
PDT	Photodynamic Therapy
PEG	Polyethylene Glycol
PEI	Polyethylenimine
PPC	Particles per cell
PpIX	Protoporphrin IX
PS	Photosensitizer
PSilQ	Polysilsesquioxane
PTT	Photo thermal therapy
PTX	Paclitaxel
RFP	Red Fluorescence Protein
RISC	RNA induced silencing complex
RNA	Ribonucleic acid
rNA	ring nucleic acid
ROS	Reactive oxygen species
RPMI	Roswell Park Memorial Institute medium
RT-PCR	Reverse Transcriptase Polymerase Chain Reaction
SCM	Succinimidyl Carboxymethyl Ester
SD	Standard deviation
SEM	Scanning electron microscopy
SiNP	Silica nanoparticles
siRNA	short interfering RNA

SMAD	small Mothers Against Decapentaplegic of of genes in Drosophila
TBE	Tris/Borate/EDTA
TEM	Transmission electron microscopy
TEOS	Tetraethyl orthosilicate
TMOS	Tetramethyl orthosilicate
TESPIC	3-(Triethoxysilyl)propyl isocyanate
TGA	Thermogravimetric Analysis
THPMP	3-(Trihydroxysilyl)propyl methylphosphonate, monosodium salt solution
TLR	Toll like receptor
TRAIL	Tumor necrosis factor (TNF)-related apoptosis-inducing ligand
TRITC	Tetramethylrhodamine
UHPLC	Ultra-High-Performance Liquid Chromatography
UPS	Ubiquitin proteasome system
VEGF	Vascular endothelial growth factor

1. Introduction

1.1. Introduction to silica nanoparticles used in drug delivery

The rise of nanomaterials for cancer research and other biomedical applications comes from the unique ability to control the characteristics and outcome of the particles in biological conditions. Designing multifunctional nanomaterials with tailored physico-chemical properties using bottom-up chemistry enables bioimaging, sensing, and therapeutic applications. The design and synthesis of inorganic-organic hybrid materials with well-defined structures have attracted great interest in drug delivery systems [1]. Nanomaterials with specific structures comprising organic and inorganic building blocks can combine their individual characteristics and utilize the resultant synergy in enhancing bioavailability of drugs [2]. The combination of silicate precursors and organic species have been used to form hybrid materials characterized by large specific surface areas and tunable uniform pore sizes. Silicate materials with well-ordered hexagonal mesopores were first reported by employing quaternary ammonium cationic surfactant (cetyltrimethylammonium bromide (CTAB)) as pore template in the mesoporous order [3]. This formed the basis of mesoporous silica nanoparticles (MSN) synthesis which was further coupled with efficient surfactant etching techniques to maintain the mesoporous framework intact wherein cargo can be loaded and stored until release is prompted by external stimuli [3]. MSNs are a class of silica nanoparticles formed using classical silica precursors such as tetraethoxysilane (TEOS) or tetramethoxysilane (TMOS). Drug loading or functionalization of MSNs occurs after the base material is synthesized and purified. This is the difference between MSNs and other commonly known lipid and polymer-based nanocarriers. Alternately, polysilsesquioxane matrices are formed by hydrolysis and condensation reactions of bridged organosilica precursors (also known as bridged organosilane or organo-bridged silane or bridged silsesquioxane) in a synthesis method commonly known as sol-gel process aided by the co-

operative self-assembly of structure directing agents [4, 5]. Polysilsesquioxane nanoparticles make another class of silica-based nanoparticles used for drug delivery. Drug molecules conjugated to two or more (n) mono-functional silane, e.g, (3-Aminopropyl)triethoxysilane (APTES), 3-(Triethoxysilyl)propyl isocyanate (TESPIC) molecules form the bridged (n=2) or pendant (n>2) precursors that are subsequently added to the sol-gel process along with a structural template like microemulsion or surfactant. Unlike MSNs, drugs are chemically embedded into polysilsesquioxane nanoparticles during the sol-gel process. Silica and organosilica nanoparticles offer controllable size, composition, morphology, porous structure and pore size, surface chemistry, and dispersibility. Myriads of reports in the literature have shown that silica nanoparticles can robustly transport imaging or therapeutic contents in vivo [6].
The following sections will focus on some therapeutic strategies under research for cancer treatment, their mechanisms of cytotoxicity against cancer cells and the role of nanoparticles, also including silica based formulations as effective drug delivery systems.

1.2. Introduction to RNA interference (RNAi) therapy

RNA interference (RNAi) is a sequence-specific, post-transcriptional gene silencing mechanism mediated by double-stranded RNA (dsRNA) with sequences homologous to the target gene. The phenomenon of RNAi was first reported in *Caenorhabditis elegans*, where the injected dsRNA molecules caused silencing of complementary messenger RNA (mRNA) and blocked function of the target gene much effectively than single stranded antisense oligonucleotides [7]. Further studies in mammalian cells showed sequence specific gene silencing in mammalian cells mediated by double stranded siRNA duplexes without inducing interferon [8]. As seen in *Figure 1*, RNAi is initiated by dsRNAs processed by an endonuclease enzyme called Dicer. This enzyme cleaves dsRNA into duplexes with approximately 19 nucleotide (nt) base pairs and 2 nt

overhangs at the two 3´ends [9]. These duplexes are referred to as short interfering RNA (siRNA) that associate with the RNA-induced silencing complex (RISC), a large protein complex comprised of Argonaute (Ago) proteins. In humans, Ago2 protein of the Ago family specifically possesses an active catalytic domain for cleavage activity [10]. Within the RISC, the sense strand of the siRNA is degraded by nucleases. The antisense strand directs the RISC to the target mRNA. At the cleavage site, Ago2 breaks the phosphodiester bond on the mRNA and releases the fragments, which manifests as gene silencing. The siRNA loaded RISC sustains its gene silencing activity for a long time in the cell, making RNAi an attractive targeted therapeutic mechanism [11]. Proof of concept studies employing RNAi showed that human diseases with a gain of function genetic mutation or overexpression of disease-causing genes are suitable targets for RNAi based therapeutics [12, 13]. Two decades after RNAi was discovered, the first siRNA based drug Patisiran was approved by FDA in August 2018 for the treatment of polyneuropathy [14]. Givosiran is the second siRNA drug to be approved in November 2019 for the treatment of acute hepatic porphyria. Recently, the third siRNA-based therapy (lumasiran) was approved in November 2020 for the treatment of primary hyperoxaluria type 1 (PH1) [14] [15].

RNAi is useful for the treatment of diseases harboring non-druggable aberrant pathways. Preclinical studies of RNAi therapeutics for the treatment of hypercholesterolemia, viral hepatitis, Huntington's disease, and cancer have revealed great translational potential [16] [17] [18] [19]. Initially, RNAi-based clinical trials focused on direct localized delivery of siRNA to well-known therapeutic targets such as vascular endothelial growth factor (VEGF). For instance,

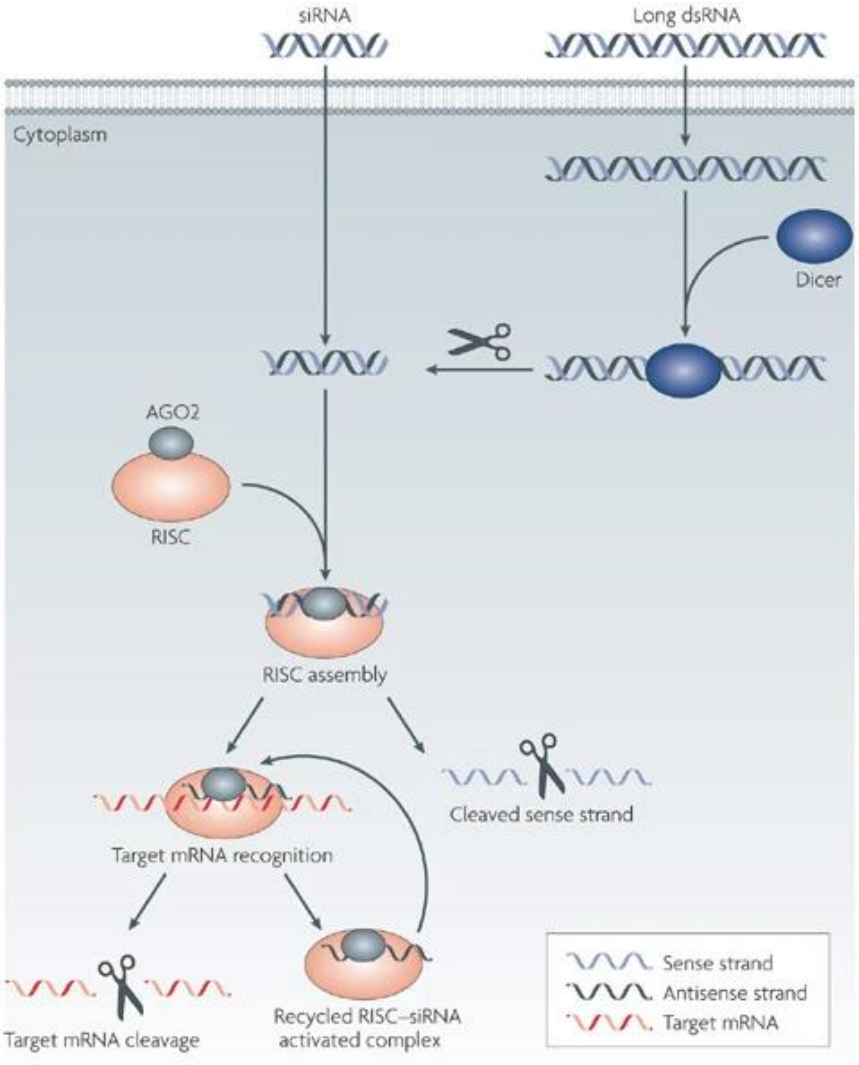

Figure 1. Mechanism of RNAi in vitro. Processing of long dsRNA by RNase III Dicer into small interfering RNA (siRNA) duplexes, loading of one of the siRNA strands on an Argonaute protein possessing endonucleolytic activity, target recognition through siRNA basepairing, and cleavage of the target by the Argonaute's endonucleolytic activity.

Image from [20]

VEGF-specific siRNA is administered directly into the vitreal cavity of the eye to treat age-related macular degeneration [21]. RNAi-based genetic medicine for the treatment of respiratory syncytial virus (RSV) is locally delivered to the lungs [22]. However, RNAi therapy development for systemic delivery to target diseases like cancer necessitate the search for robust delivery systems.

1.2.1. Prospects of RNAi in cancer therapy

Heterogeneity associated with cancer across different stages and subtypes, offers several targets for RNAi. Oncogenes, mutated tumor suppressor genes, and genes contributing to tumor progression are some common examples of target classes amenable to gene silencing by RNAi [23], which are discussed in this section. In addition to cancer therapy, RNAi has been applied in drug discovery settings to silence the expression of dominant mutant oncogenes, gene amplifications, translocations, and viral oncogenes to determine their influence on critical cellular pathways [24]. The understanding obtained from such studies has led to improvement in the efficacy of existing cancer therapies by specifically silencing resistance associated genes. To better appreciate the prospects of RNAi therapy for cancer, potential targets are described below:

Biomolecules involved in carcinogenesis.

mRNAs expressed from mutated oncogenes are primary targets for RNAi intervention. In corollary, gene products that negatively regulate the function of endogenous tumor suppressors also make attractive targets for RNAi. For instance, proteins involved in oncogenesis such as Bcr-Abl [25], EGFR [26], Her-2/neu [27], HIF-1, SMAD [28], loss or delay of cellular senescence (hTER) [29], cell cycle regulation (pRb, p53 family) [30] and anti-apoptotic proteins such as FLIP [31], Bcl-2 , Bcl-xL [32], Mcl-1 [33], and survivin [34] have been targeted by RNAi.

Target proteins involved in tumor-host interactions.

Cancer cells adapt to host environments with ever changing physio-chemical factors. Therefore, neoplastic cells develop multiple survival strategies to gradually take control of the host environment through angiogenesis, invasion/metastasis and immune evasion. Some examples of RNAi technology to target proteins involved in tumor-host interactions are: anti-VEGF [35], anti-cell adhesion molecule-1 (CEACAM1) [36], heparinase for reduced vascularization [37], CXCR4 in breast cancer cells [38], and EphA2-specific in pancreatic adenocarcinoma [39]. Moreover, RNAi targeting interleukin-10 (IL-10) and other immunosuppressive cytokines represents a plausible approach for addressing tumor immune evasion [40]. Finally, RNAi targeting Galectin-1 was found to stimulate antitumor T-cell-mediated responses in mice [41].

Target proteins involved in tumor resistance to chemotherapy and/or radiotherapy.

RNAi targeting of multi-drug resistant (MDR) genes such as ABCB1, 4 and 5 sensitize several chemo resistant cancer cells in vitro [42]. RNAi technology has been used in these settings to downregulate DNA repair genes such as the excision repair cross-complementing 1 (ERCC1), DNA double-stranded break repair protein endo-exonuclease, ribonucleotide reductase, double-strand break signaling/repair proteins ATM and DNA-dependent protein kinase catalytic subunit, and enhance the sensitivity of cancer cells to chemotherapeutic agents or irradiation [43]. These biomolecules serve as potential targets for RNAi intervention in combination with chemotherapy or radiotherapy [44].

1.2.2. Limitations of RNAi therapy

Several concerns related to the use of RNAi therapy have been reported in literature. RNAi could trigger unforeseen immune responses *in vivo* by activating toll-like receptors that recognize foreign nucleic acids including dsRNA resulting in danger signals from the cells to trigger

proinflammatory responses [45]. RNAi may remain inaccessible to some gene products due to physical hindrance posed by RNA-binding proteins or secondary structures. Therefore, RNAi therapy for cancer should consider multiple sequences per target [46]. Moreover, RNAi is effective only for proteins with rapid turnover. Targeting proteins with a long half-life may result in therapeutic failure because silencing at the transcript level does not impact the pre-existing levels of proteins [24]. Finally, the translation of RNAi from a research tool to an effective therapeutic strategy is prevented by the lack of efficient delivery methods to efficiently target cells through systemic and cellular barriers while avoiding degradation [47]. For a sustained inhibitory effect, viral vectors that can stably integrate into the genome and mediate long-term knockdown of transcripts have been used [48]. Retrovirus, lentivirus, adeno-associated and adenovirus are some examples of gene delivery systems used to transfer siRNA. However, one the use of viral vectors is the restricted by dose-limiting toxicity [49]. Recently, exosome mimetic gene carriers produced from engineered cells and expressing specific surface carriers have been under development to promote target specificity, efficient siRNA loading and siRNA release mechanisms [50].

1.2.3. siRNA delivery using nanoparticles

Nanoparticles have received considerable attention as vectors for gene delivery. Advantages of non-viral gene delivery methods like nanoparticles include- high loading capacity, easier synthesis, and purification methods than viruses, animal component free synthesis methods, lower overall cost of production, ease of handling/processing such as freeze drying and resuspension at point of use while virus lots must be maintained in liquids buffers at all times [51]. Nanoparticles are particulate dispersions or solid particles with sizes in the range of 10–1000 nm. Nanocarriers can protect RNAi molecules from enzymatic degradation and immune recognition, have much higher

transportation efficiency across the cell membrane compared to other carriers and can prevent premature excretion if the carrier size and surface coating are appropriate [46]. At the cellular level, mechanism of siRNA release into the cytoplasm is dictated by charge-based destabilization of endosomal membranes in the case of lipid based nanocarriers. Osmotic swelling induced by an influx of protons is another mechanism of siRNA release for RNAi demonstrated by surface functionalized nanocarriers bearing amine or other cationic groups endowing a pKa between 5 and 7 [52]. Nanocarriers applied to RNAi can be classified as organic and inorganic nanoparticles.

Organic nanoparticles can incorporate drugs by means of chemical bonding or physical embedding. Organic nanocarriers fabricated from cationic polymers like polyethyleneimine (PEI), poly-L-lysine (PLL), and natural polymers like chitosan have been used to carry siRNA [43]. PEI polyplexes have shown high transfection efficiencies, but these systems have not succeeded been translated to clinical application *in vivo* for systemic delivery due to extreme toxicity and instability [53]. However, polyethylene glycol (PEG)-PEI siRNA polyelectrolyte nanocomplexes have shown to reduce vehicle associated cytotoxicity [44]. For instance, these PEGylated polyplexes containing vascular endothelial growth factor (VEGF)-targeted siRNA were accumulated in tumor regions, and the knockdown of VEGF suppressed micro vessel formation, thereby inhibiting tumor growth [45]. Further, Patil and co-workers showed Bcl2 gene silencing and successful apoptosis induction in A2780 ovarian carcinoma cells using polymeric micelles assembled from a multifunctional triblock co-polymer (PAMAM-PEG-PLL) [54]. Han et al also demonstrated PLDCX1 gene silencing and consequent inhibition of tumor growth in an orthotopic in vivo model of ovarian cancer using Arg-Gly-Asp (RGD) peptide-labeled chitosan nanoparticle (RGD-CH-NP) as a novel tumor targeted delivery system [55].

In addition to polymers, lipids constitute another class of organic nanomaterials for siRNA delivery. Philip Felgner pioneered the use of synthetic cationic lipids to bind lipids to nucleic acids to enable their transfection into cells [56]. This formed the basis of lipid nanoparticle (LNP) design for nucleic acid delivery. LNP formulations encapsulating siRNA have been applied to the treatment of viral infections. A multicomponent LNP system comprising a mixture of amino lipids (DLin-MP-DMA), PEG lipids (PEG-CDMA), and neutral lipids (cholesterol and dipalmitoyl phosphatidylcholine) was described for fully encapsulating short synthetic hairpin RNAs (sshRNAs) that target the internal ribosome entry site of the hepatitis C virus (HCV) [57] [58]. This system showed the efficacy of sshRNA against the HCV genome in reducing HCV infection *in vivo*. The suitability of LNPs for nucleic acid delivery was evidenced by the world through the success of SPIKEVAX (COVID-19 Vaccine, mRNA) made by ModernaTX Inc, and the Pfizer–BioNTech COVID-19 vaccine to prevent Coronavirus Disease 2019 (COVID-19) caused by SARS-Cov-2. Stable nucleic acid-lipid particles (SNALPs) were synthesized by Geisbert et al to deliver antiviral siRNA constructs to prevent viral infections of Zaire Ebola virus (ZEBOV) and Marburg virus (MARV) [59]. A combination of modified siRNAs targeting the ZEBOV L polymerase (Lpol), viral protein (VP) 24 (VP24), and VP35 formulated in SNALPs were able to protect the tested non-human primate model from lethal ZEBOV infection [60]. In the realm of cancer therapy, siRNA encapsulated in neutral liposomes for RNA interference reported by Sood et al is a successful example of 1,2-dioleoylsn-glycero-3-phosphatidylcholine based liposomal siRNA, which induced repression of EphA2 oncogene and proangiogenic cytokine interleukin 8 (IL-8) [19]. This strategy was highly effective in reducing *in vivo* target gene expression in an orthotopic mouse model of ovarian cancer.

In addition to organic nanoparticles, there is ongoing research for robust inorganic carriers of siRNA that permit high loading capacity of siRNA and can also be selectively surface functionalized to enable specific targeting applications without compromising the stability of the nano formulation. MSNs surface coated (outer) or functionalized (inner pores) with cationic moieties are commonly used inorganic nanoparticles for siRNA delivery because of their unique properties such as uniform mesopores, easy functionalization, biocompatibility, high surface to volume ratio, large pore volume to hold siRNA therapeutics [61-63]. Spherical mesoporous silica nanoparticles (MSNs) with core size range from 50 to 200 nm and modified with polyethyleneimine (PEI) or PEI- polyethylene glycol (PEG) or polyamidoamine (PAMAM) are applied for siRNA binding [64]. For instance, MSNs loaded with siRNA in the amine modified inner pores and outer surface coated with PEI and fusogenic peptide KALA (~30 amino acids) inhibited VEGF expression and tumor angiogenesis, leading to tumor growth suppression [65]. A nanoparticle construct was engineered by Ngamcherdtrakul and co-workers for the targeted delivery of siRNA to tumors. The construct comprised of MSNs coated with cross-linked PEI-PEG copolymer, carrying HER2 specific siRNA, and coupled to the anti-HER2 monoclonal antibody (trastuzumab) [66]. The construct was designed to enhance tumor-specific cellular uptake and maximize siRNA knockdown efficacy. One dose of the siHER2 MSNs reduced HER2 protein levels by 60% in trastuzumab-resistant HCC1954 (HER2+) xenografts [66]. Multiple doses administered intravenously significantly inhibited tumor growth. In terms of immunocompatibility, the siHER2-loaded MSNs demonstrated an excellent safety profile in terms of blood compatibility and low cytokine induction, when exposed to human peripheral blood mononuclear cells. A similar PEI-PEG functionalized MSN platform, surface conjugated to trastuzumab antibodies was also used for the targeted delivery of PLK1 siRNA for metastasis

inhibition in triple negative breast cancer. Where PLK1 pharmacological inhibitors have shown to impart adverse side effects and siPLK1 encapsulated in lipid nanoparticles without a targeting agent only provided a narrow therapeutic window in clinical trials, the sequence specificity of siPLK1 when combined with the tumor targeting ability of the trastuzumab-MSN platform improved treatment efficacy for metastatic breast cancer [67].

In addition to surface functionalized mesoporous silica nanoparticles, gold-thiol chemistry has been utilized for siRNA binding and targeting antibody conjugation to gold nanoparticles and subsequent targeted siRNA delivery to cancer cells [68]. Wang et al reported a gold nanorod (GNR) platform where the citrate-stabilized GNRs were first coated with a zwitterionic amphiphile moiety with low cytotoxicity, which produced stable dispersions at high ionic strength. Amine-modified siRNA duplexes were converted into dithiocarbonate (DTC) ligands and adsorbed onto the modified GNR surfaces, simplifying the charge screening process [69]. The DTC anchors were effective at minimizing premature siRNA desorption and release, a common but often overlooked problem in the use of inorganic nanoparticles as oligonucleotide carriers [69].

So far, only synthetic nanoparticles or bioprocessed viral vectors have been discussed as siRNA delivery vehicles. Despite advances made towards safe and targeted siRNA delivery in preclinical studies, charge based loading of siRNA onto external surface of inorganic nanoparticles has its disadvantages. Premature release of siRNA due to their interaction with proteins, lipoproteins, and the extracellular matrix is a notable limitation of inorganic siRNA carriers [7].

Recently exosome mimetic bio-harvested carriers have also been applied for siRNA delivery specifically to harness the non-immunogenic delivery capabilities of the platform [50]. Alvarez-Erviti and group harvested exosomes from self-derived dendritic cells to reduce immunogenicity of the carriers [70]. Further, brain tissue targeting was achieved by engineering the dendritic cells

to express Lamp2b, an exosomal membrane protein fused to neuron specific RVG peptide [71]. Produced exosomes were electroporated for loading with BACE1 siRNA (a therapeutic target in Alzheimer's disease). The therapeutic potential of this platform was evidenced by effective (~60%) gene silencing in wild type mice. The RVG-targeted platform also prevented non-specific accumulation in other tissues. Zhang et al. used serum-derived exosomes (EXOs) as vehicles to deliver Myd88 siRNA to the lung [72]. siRNAs were first loaded into serum EXOs through calcium-mediated transfection and then were intratracheally instilled in LPS-induced mouse model. The siRNA-carriers were efficiently internalized by alveolar macrophages and achieved specific gene silencing and modulated LPS-induced inflammation. The serum derived EXOs themselves were neither inflammatory nor immunogenic when delivered into the lung [72].

RNA nanoparticles (RNA NPs) present a class of rationally designed multistranded RNA constructs that simultaneously incorporate various functionalities with promising therapeutic capabilities [73-75]. Using natural or artificially selected RNA motifs and modules, RNAs are programmed to form a wide variety of stable 3D nanostructures such as cubes, rings and fibers [76-78].

Therapeutic nucleic acids, proteins, or small molecules can be individually attached to the programmed RNA monomers, which form RNA NPs. The assembly of the monomers brings the desired functionalities together, thus providing precise control over their structure, composition, and modularity [79]. The use of functional RNA NPs in vivo provides a higher concentration and desired stoichiometry of therapeutic moieties locally [80]. RNAi is progressively investigated for possible treatment of various diseases through the functionalization of RNA NPs with siRNAs [77, 81].

Simultaneous use of multiple different RNA therapeutics is expected to have significant synergistic effects [82]. One well-known example is a combinatorial RNAi (co-RNAi) used for highly effective simultaneous multiple gene suppression preventing the possibility of mutation-assisted escape from RNAi [81, 83]. For example, nanocubes and nanorings were modified to package multiple siRNAs that simultaneously target different regions of the HIV-1 genome, limiting viral escape due to mutations [74, 84]. The therapeutic composition of RNA NPs can be easily altered by swapping the functionalized monomers [77] .

1.3. Photodynamic therapy.

Photodynamic therapy (PDT) is a form of non-invasive therapy based on the local, systemic, or topical application of a photosensitive drug which accumulates in pathological tissues [85]. PDT relies on photosensitizer molecules to generate reactive oxygen species (ROS), which will damage cells. Phototoxicity occurs only in the areas where photosensitizer localizes, enabling selective destruction [86]. PDT is used in the treatment of inflammatory conditions and bacterial infections related to dermatology, oncology, gynecology and urology [87]. In the context of cancer therapy, PDT is generally applied as an adjuvant therapy to kill residual tumor cells post-surgery or pre-surgery to shrink tumors [88]. In the past few years, the field of PDT has seen a surge in the number of endogenous PSs developed using synthetic methods [89].

1.3.1 Mechanisms in PDT

PDT depends in three components; a photosensitizer (PS), light and oxygen. First, the PS molecules absorb light at the right wavelength, which activates the PSs to a singlet state. Part of the energy gained is dissipated as fluorescence and the remaining energy is transferred to the excited triplet state through an intersystem crossing process [86]. Once the PS is in the triplet state,

two photochemical mechanisms can happen, Type I or Type II (Figure 2). In type I mechanism, radical species are formed by hydrogen abstraction or electron transfer to cellular oxygen molecules. This leads to the formation of ROS, initially in the form of superoxide radicals ($O_2^{\cdot -}$) then forming H_2O_2 catalyzed by superoxide dismutase. The accumulated H_2O_2 transforms into highly cytotoxic hydroxyl radicals ($OH^{\cdot}$), causing cell death by oxidative stress [90]. In Type II mechanism, the energy in the triplet state is transferred to oxygen to afford singlet oxygen, which is a highly oxidizing molecule. Singlet oxygen will quickly react with molecules in the environment to afford cytotoxicity. Contribution by each mechanism to phototoxicity depends on the tissue, oxygen levels and the photosensitizer [91].

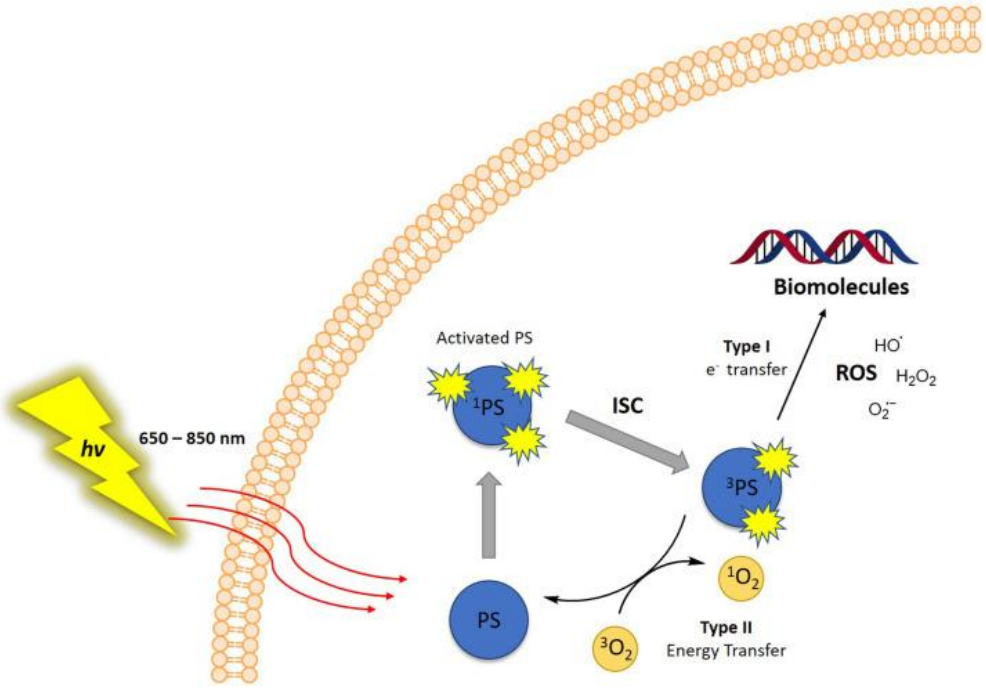

Figure 2. Mechanism of Photodynamic therapy. Photoactivation of PS to an excited triplet state through intersystem crossing triggers the generation of singlet oxygen ($^1O_2$) by direct energy transfer to cellular oxygen natively found in triplet state. Alternate type I mechanism involving electron transfer to cellular oxygen leads to the generation of ROSs.

Image from [92]

Although primary ROS are short-lived, from ns to ms depending on the specific ROS, PDT induces long term oxidative stress in treated cells due to irreversible oxidation of cellular lipids and proteins [92]. The products of PDT initiate a cascade of damaging events to the cell such as DNA damage (8-hydroxydeoxyguanosine) or impair RNA-protein translation (8-oxo-7,8-dihydro-2′-guanosine) [93]. Additionally, oxidation of phospholipid membrane constituents by PDT is also a likely cause of cell death [94]. Proteins, specifically the ones involved in energy metabolism are highly susceptible to PDT-generated ROS. Rupture of polypeptide backbone or crosslinked protein aggregates are some of the toxic products generated by PDT [95]. Collectively, the oxidative modification of biologically relevant biomolecules (proteins, DNA/RNA and lipids) disrupts the redox balance inside the cells, which is better known as oxidative stress. In case of excessive damage, cell death occurs usually via apoptosis or necrosis depending on which intracellular substrates are affected [92]. In the clinic, necrotic cell death is not a desired pathway for therapy because it can trigger inflammatory responses [92]. However, there are reports claiming contribution of necrosis or necrosis-like cell death in triggering anti-tumor immune response mediated by antigen-specific T-cells [92, 96]. A major advantage of this PDT-triggered immunological response is the therapeutic targeting of distant tumor cells (metastasis) that were not subjected to PDT, also known as abscopal effect [97]. A cell death mechanism that has been recently associated to PDT is ferroptosis , which is an iron-dependent cell death mechanism caused by extreme lipid peroxidation [98]. Mechanistically, PDT stimulates secretion of IFN-γ which further downregulates the expression of Xc- (cysteine transporter) and initiates ferroptosis [99].

In addition to PS concentration and light fluence (PDT dose), subcellular localization of the PS in the specific organelles plays a major role in the type of cell death mechanism that dominates [85, 100]. Apoptotic cell death in PDT is commonly observed for PS molecules that localize in the

mitochondria or lysosomes [101]. Plasma membrane localization of PS molecules causes necrotic cell death and apoptotic cell death together with elevated expression of autophagy markers is observed in the case of PS localization in endoplasmic reticulum and Golgi apparatus of PDT treated cells [100, 102]. Blocking apoptosis and ferroptosis with zVAD-fmk and Ferrostatin-1 respectively, showed that therapeutic efficacy of PDT is negatively affected for lysosome localized PS molecules [103]. On the other hand, inhibition of necrosis using necrostatin-1 did not impact PDT efficacy [103]. Further, PS molecules localized in the ER and Golgi apparatus were found sensitive only to apoptosis inhibition [86].

Tumor cells subjected to sublethal oxidative damage or those in the vicinity of PDT treated cells can activate cell survival mechanisms, which produces resistance to PDT [104]. For example, surviving cells may activate antioxidant response to reinstate intracellular homeostasis, which is regulated by NRF2 [105]. Another survival mechanism in response to PDT is the facilitation of refolding or degradation of carbonylated proteins via proteotoxic stress response (e.g. HSF1, XBP1, ATF6, ATF4) [106, 107]. Autophagy stimulated because of mitochondrial, or ER stress may prevent apoptotic cell death and by that means promote survival in sub-lethally damaged tumor cells following PDT [108]. Autophagy is an independent outcome in PDT protocols characterized by up-regulated LC3B, Atg7, Beclin-1, mostly reported to exert a pro-survival role by catabolizing the damaged organelles and biomolecules[109]. Autophagy came to be identified as an index for health and disease when Yoshinori Ohsumi was awarded the Nobel Prize for Physiology or Medicine (2016) for characterizing morphological changes associated with autophagic mechanisms, that are evolutionarily conserved from yeast to higher eukaryotes [110]. As lysosomal catabolic processes, selective and non-selective autophagy play pivotal roles in maintaining cellular homeostasis by metabolizing intracellular stressors like damaged organelles,

oxidized biomolecules, and their aggregates. ROS production by PDT primarily results in the oxidation of biomolecules, thereby leading to protein misfolding or formation of protein aggregates [111]. These forms of proteotoxic stress initiate degradation-recycling mechanisms by sequential addition of ubiquitin chains to the damaged substrates[109]. Ubiquitinylation is a downstream effect of proteotoxicity through which terminally misfolded proteins and protein complexes are tagged for proteasomal and autophagic degradation, eventually reducing proteotoxic stress[112]. It can be inferred that, when the adaptive responses to misfolded and aggregated proteins are constitutively active in tumor cells, the threshold for the PDT mediated induction of cell death will be higher [104]. Disrupting the cytoprotective effects of the ubiquitin proteasomal and autophagy systems by interfering with the function of chaperones has shown to enhance proteotoxic stress and stimulate cell death after PDT[113]. Thus, the proteotoxic stress pathway is seemingly an important target for pharmacological interventions to enhance the therapeutic efficacy of PDT [104].

Autophagic activity is known to be upregulated beyond basal levels in response to stressful stimuli induced by several human metabolic and inflammatory diseases (hypoxia, nutritional deprivation), also notably by some methods used to treat these conditions (ROS, DNA damage)[114-116]. Partly, what appears to be PDT resistance is contributed by autophagy promoted cell survival [117, 118]. The rationale for combining autophagy inhibitors with PDT is to enable higher sensitivity of cells to apoptosis[119]. Increase in cell death by autophagy inhibition is reported to be a stage of pathway and context dependent occurrence. For example, negative regulation of autophagy at different stages of the cellular process, such as genetic knockdown of autophagy inducers, prevention of autophagosome maturation, and blocking lysosome fusion evince different responses in some instances [114]. The dissimilarities in the interaction of autophagy inhibitors

with different therapies based on the stage and type (chemical or genetic) of intervention, highlights the premise of context dependent co-activity [120, 121]. Identification of the stage of autophagic intervention that yields a therapeutic benefit with PDT helps in designing effective treatment protocols.

1.3.3 Delivery strategies for photosensitizers.

One of the main issues limiting the clinical use of PDT is the lack of accumulation of PSs at optimal concentrations in the targeted tissues [122]. Nanoplatforms enable precise drug delivery to the desired location to improve the therapeutic effect against cancer and other disease. Nanoparticles have been used extensively as carries for PSs to improve the PDT outcome [123]. PS molecules can be immobilized to nanoplatforms by covalent or non-covalent interactions. Since most PSs are highly hydrophobic substances that aggregate in aqueous environments, their encapsulation in nanoparticles has a major impact on their colloidal stability and bioavailability in vivo. This phenomena has been demonstrated by several reports [123-125]. Organic nanoparticles have been exercised for the delivery of PSs. For instance, an increase in PDT efficiency with the use of water-soluble polymer polyacrylamide (PAA) to carry photosensitizers like methylene blue (MB) and porphyrins was observed in the treatment of C6 glioma cells [126]. Another polymer, N-2-hydroxypropylmethylacrylamide (HPMA) was used in PDT protocol for the treatment of neuroblastoma and ovarian cancer [127]. Inorganic nanoparticles have also been used as carriers for PSs. Platforms such as gold NPs and silica nanoparticles can be used to create photosensitive conjugates as a potential way to increase colloidal stability and selectivity of PDT [128, 129].

Bouramtane and co-workers synthesized core-shell hybrid nanoparticles formed by a silica core and carbohydrate xylan-based shell carrying a 5-(4-hydroxyphenyl)-10,15,20-triphenylporphyrin (TPPOH), and evaluated their anticancer activity in colorectal cancer cells [130]. The xylan-

TPPOH conjugate (PX) was used to coat the silica nanoparticles (PX SNPs). The obtained nanoparticles were characterized and their therapeutic potential for PDT evaluated against colorectal cancer cell lines. The phototoxic analysis showed that PX SNPs were 40-fold and 10-fold more effective against HCT116 cells and HT-29 cells respectively compared to free TPPOH [130]. Hui Lin et al demonstrated ease of functionalization and resultant stability of hydroxylated benzene-bridged periodic mesoporous organosilica nanoconjugates with PpIX [131]. The platform showed improved PDT efficacy in metabolic inactivation of tumor cells and for anti-bacterial applications compared to free PpIX.

Hone et al demonstrated that gold nanoparticles (AuNP) functionalized with phthalocyanine boost singlet oxygen generation (SOG) capacity of the photosensitizer [132]. Compared with the free photosensitizer, the composites of photosensitizer, gold and phase transfer reagent were demonstrated to achieve a higher singlet oxygen generation (SOG). They showed that the AuNPs could be used to efficiently deliver photosensitizer in PDT to improve the cytotoxic efficacy of photosensitizer against HeLa cells in vitro. Irradiation of the nanoparticle composite treated HeLa cells resulted in a decrease in cell viability to 43% as compared to the free phthalocyanine and 50% increase of SOG observed for the phthalocyanine-nanoparticle composite as compared to the free photosensitizer [132]. Wang et al. used biocompatible AuNPs as a vehicle to deliver 5-aminolevulinic acid (5-ALA) for photodynamic therapy, and they demonstrated that tumor cells can be effectively killed by 5-ALA-conjugated nanoparticles, while fibroblasts were minimally damaged, showing promise of selective killing of tumor cells and sparing healthy cells [133].

Next generation of nanoparticulate PSs are under development to improve the absorption of light in the NIR to overcome issues related to light tissue penetration [91].

Lanthanide-doped upconversion nanoparticles (UCNPs) present one such platform developed to achieve NIR-triggered PDT. As an anti-stokes shifting material, UCNPs are the most efficient materials for converting NIR light to UV and visible light [134, 135]. The emitted high energy radiation can in return activate attached PS molecules to produce singlet oxygen and kill cancer cells [136]. Therefore, UCNPs are applied as transducers to activate a conventional photosensitizer that is sensitive to visible light by using a NIR light source. Additionally, the use of NIR photons minimizes phototoxicity, which is beneficial for bioimaging, diagnosis, and therapy [137]. UCNP-based theranostic agents have been reported for simultaneous diagnosis and treatment of diseases. NIR-responsive PDT agents with dual photosensitizers were prepared by Yuel Lee and co-workers [138]. They selected 808 nm wavelength excitation instead of the 980 nm wavelength for irradiation to minimize overheating by the light source. For efficient photosensitizer activation using the 808 nm NIR wavelength excitation, $NaYF_4$:Yb,Er,Nd@$NaYF_4$:Yb,Nd was selected as Nd-doped UCNPs with a core-shell structure [139]. The dual photosensitizers, Chlorin e6 and Rose Bengal, were activated by the red and green emission of UCNPs. The dual photosensitizer system showed a synergistic ROS generation as compared to the single photosensitizer system [140]. The ROS production achieved by NIR, and PDT induced apoptosis in cancer cells [140].

A major issue for cancer treatment is the precise delivery of the therapeutic agent in the tumor tissue. Nanoparticle-based delivery systems have two interrelated mechanisms to target tumors, passive, and active accumulation [141]. Passive accumulation of nanoparticles relies on the fenestration and leaky vasculature characteristic of primary tumor tissues, also known as enhanced permeability and retention effect (EPR) [142]. Active accumulation involves the use of targeting agents such as antibodies, peptides, or small molecules [141, 142]. Nanoparticles carrying PSs have used different cell surface binding groups such as folic acid, antibodies, polysaccharides like

pectin, amylose, inulin, dextran, etc [1]. Zinc phthalocyanine containing upconversion liposomes conjugated to folic acid showed excellent PDT activity for tumor treatment through folate receptor targeting [143]. A 4-component antibody-phthalocyanine-polyethylene glycol-gold nanoparticle conjugate is described by Stuchinskaya and group for use as a potential drug for targeted photodynamic cancer therapy [144]. AuNPs (4 nm) were stabilized with a self-assembled layer of a zinc-phthalocyanine derivative as the PS and a heterobifunctional polyethylene glycol. Anti-HER2 monoclonal antibodies were covalently bound to the nanoparticles via a terminal carboxy moiety on the polyethylene glycol. The nanoparticle conjugates were stable towards aggregation, and under irradiation with visible red light efficiently produced cytotoxic singlet oxygen. Cellular experiments demonstrated that the nanoparticle conjugates selectively target breast cancer cells that overexpress the HER2 epidermal growth factor cell surface receptor [144]. Bharatiraja and co-workers synthesized chlorin e6 (Ce6)-conjugated and folic acid (FA)-decorated silica nanoparticles (silica-Ce6-FA) for targeted delivery of photosensitizer to the cancer cells [145]. The formulated particles were efficiently taken up by folate receptor-positive MDA-MB-231 cells, which was confirmed by comparative analysis with folate receptor-negative HepG2 cells [145]. The folate receptor-targeted silica-Ce6-FA was highly accumulated inside the MDA-MB-231 cells than free Ce6. The cell-killing effect of silica-Ce6-FA was higher when compared with free Ce6 under PDT treatment. The PDT-induced mitochondrial damage and apoptotic cell death were detected in silica-Ce6-FA-treated cells [145].

1.4. Nanoparticle mediated combination therapies for cancer.

Current clinical approaches to treat cancer involved the use of two or more therapeutic agents [146]. However, two main challenges are associated with that approach; first, the different

pharmacokinetic (PK) and pharmacodynamic (PD) profile of the drugs that makes complicated to find the optimal administration regimen; and second, the increase in side-effects due to the combination. Nanotechnology has played an important role in the improvement of PK and PD of single therapeutic agents. In the case of combination therapy, by carrying two or more drugs in the same nanoparticles, this strategy ensures their delivery at the same location with spatiotemporal controlled release [147]. Below, there is a description of the three main categories for combination therapy.

1.4.1 Combination of multiple chemotherapy agents.

In clinical settings, this therapy is also known as drug cocktail therapy. This type of combination therapy is preferred for patients in an advanced stage of cancer [146]. Combination therapy involves two or more chemotherapy agents, which can be delivered simultaneously or sequentially. The interaction of anticancer drugs with different mechanisms of action creating synergistic or additive therapeutic effects are ideal candidates for combination therapy [148]. Combinations of anticancer agents are administered to cancer patients to reduce dose-associated toxicity and to minimize the risk of developing multidrug resistance. One of the most important parameters in combination chemotherapy is the molar ratio between the drugs being administered, which has shown to influence the overall outcome of the cancer therapy [148]. These are some examples of nanoparticles formulated for loading two or more chemotherapy agents: liposomal formulation CPX 351 which contains cytarabine and daunorubicin at a molar ratio of 5:1 [149]; liposome CPX 571 loaded with irinotecan and cisplatin at a molar ratio of 7:1 [150]; and polymeric nanoparticles loaded with paclitaxel (PTX) and gemcitabine (GEM) at a molar ratio of 7:1 [151]. Lipid bilayer coated mesoporous silica nanoparticles (LB MSNs) were used to co-deliver PTX and GEM for the treatment of human pancreatic cancer in mice. PTX was incorporated in a lipid bilayer coating the

MSNs [152]. The ratiometric PTX incorporation and delivery by LB-MSNP could suppress GEM-inactivating, cytidine deaminase (CDA) expression, contemporaneous with induction of oxidative stress as the operating principle for PTX synergy. To demonstrate the in vivo efficacy, mice carrying subcutaneous PANC-1 xenografts received intravenous (IV) injection of PTX/GEM-loaded LB-MSNP [152]. Drug co-delivery provided more effective tumor shrinkage than GEM-loaded LB-MSNP, free GEM, or free GEM plus Abraxane (commercial PTX). Comparable tumor shrinkage required coadministration of 12 times the amount of free Abraxane. IV injection of MSNP-delivered PTX/GEM in a PANC-1 orthotopic model effectively inhibited primary tumor growth and metastasis. The enhanced in vivo efficacy of the dual delivery carrier was achieved with no trace of local or systemic toxicity.

1.4.2 Combination of chemotherapy and gene/protein therapy.

The primary goal of this combinational approach is to sensitize the cells or the immune system to interfere in the different cancer signal pathways and processes. By disrupting cancer signals and pathways, it is possible to trigger the concatenation of chemical responses in the cell [57]. Some of the strategies involve the combination of drugs with genes/proteins that allow to: 1) increase vascular permeability and facilitate drug penetration, 2) inhibit angiogenesis in tumor, 3) induce apoptosis, 4) efflux transporter inhibitors, and 5) target tumor cells at the molecular level [153, 154]. The chemical responses to these approaches tamper angiogenesis or proteasomes to improve therapeutic efficacy or raise the genetic barriers to minimize the potential risk of multi drug resistance (MDR) development, thus attaining a synergistic therapeutic efficacy [155].

Wang et al. developed a core–shell biodegradable nanoparticles system through self-assembly of cationic amphiphilic copolymers for simultaneous delivery of drugs and DNA or siRNA [156]. PTX, indomethacin, or pyrene were loaded in the hydrophobic core of nanoparticles, whereas

plasmid DNA was assembled on the surface of the nanoparticle [156] . The co-delivery of paclitaxel with an interleukin-12-encoded plasmid using these nanoparticles suppressed cancer growth more efficiently than the delivery of either paclitaxel or the plasmid in a 4T1 mouse breast cancer model [157]. Moreover, the co-delivery of paclitaxel with Bcl-2-targeted small interfering RNA (siRNA) increased cytotoxicity in MDA-MB-231 human breast cancer cells [156].

Therapeutic proteins tend to be attached at the surface of the nanoparticle carrier to facilitate specific recognition by the targeted cellular pathways. For example, liposomes were decorated with a cell penetrating peptide (CPP-RH83) to target cancer cells [158]. Dox was loaded in the liposomes core and the tumor necrosis factor related apoptosis-inducing ligand (TRAIL) was encapsulated within the PAMAM dendrimer nanoparticles [159]. The results showed DOX-loaded M-PAMAM complexed with TRAIL plasmid showed much stronger antitumor effect than M-PAMAM containing DOX or TRAIL plasmid. Further, the treatment of mice bearing C26 colon carcinoma with this developed co-delivery system significantly decreased tumor growth rate [159]. Similarly, Zhou and group developed a MSN-based codelivery system for targeted simultaneous delivery of doxorubicin (DOX) and Bcl-2 small interfering RNA (siRNA) into breast cancer cells [160]. The multifunctional MSNs (MSNs-PPPFA) were prepared by modification of polyethylenimine–polylysine copolymers (PEI-PLL) via the disulfide bonds, to which a targeting ligand folate-linked poly(ethylene glycol) (FA-PEG) was conjugated [161]. The multifunctional nanocarrier has the ability to encapsulate DOX into the channels of MSNs, while simultaneously carrying siRNA via electrostatic interaction between cationic MSNs-PPPFA and anionic siRNA. The folate-conjugated MSNs showed enhanced cellular uptake in folate expressing MDA-MB-231 breast cancer cells. The delivery of Bcl-2 siRNA downregulated the Bcl-2 protein expression, and

thus targeted codelivery of DOX and Bcl-2 siRNA by DOX@MSNs-PPPFA/Bcl-2 siRNA in MDA-MB-231 cells induced greater cell apoptosis than singular DOX therapy [161] .

Multifunctional mesoporous silica nanoparticles (MSNPs) has been developed to overcome doxorubicin (DOX) resistance in a multidrug resistant (MDR) human breast cancer xenograft by co-delivering DOX and siRNA that targets the P-glycoprotein (Pgp) drug exporter. The Pgp siRNA selection from among a series of drug resistance targets was achieved by performing high throughput screening in a MDR breast cancer cell line, MCF-7/MDR. Following the establishment of an MDR xenograft model in nude mice, Meng et al demonstrated that a 50 nm MSNPs, functionalized by a polyethyleneimine-polyethylene glycol (PEI-PEG) copolymer, provides protected delivery of stably bound DOX and Pgp siRNA to the tumor site [162]. Compared to free DOX or the carrier loaded with either drug or siRNA alone, the dual delivery system resulted in synergistic inhibition of tumor growth in vivo. Analysis of multiple xenograft biopsies demonstrated significant Pgp knockdown at heterogeneous tumor sites that correspond to the regions where DOX was released intracellularly and induced apoptosis [162].

1.4.3. Combination of chemotherapy and photodynamic therapy.

With the development of new photosensitizers, this combinational approach has surfaced in past few decades. PDT has been reported to reinforce chemotherapy or re-sensitize resistant tumors to chemotherapy [163]. Wang and co-workers reported a chemo-PDT combinatorial therapies such as hollow mesoporous silica nanocages loaded with DOX and hematoporphyrin [164]. Hematoporphyrin molecules doped in the nanoparticles and allowed for PDT in addition to DOX induced chemotherapy. The combination therapy combining exhibited synergy and high therapeutic efficacy for cancer therapy in vitro [165].

Juneja and co-workers demonstrated the ability of a stimuli-responsive polysilsesquioxane (PSilQ)-based platform to co-deliver protoporphyrin IX (PS) and curcumin (chemotherapy agent) and RNA interference inducers inside human cells [166]. This multimodal delivery system showed a synergistic performance for the combined phototherapy and chemotherapy in triple-negative breast cancer cells. The platform also demonstrated efficient transfection of nucleic acids and constituted the first instance of using the PSilQ platform for the combined phototherapy and chemotherapy and gene delivery. Zhang et. al. also reported a chemo-PDT platform using MSNs co-loaded with Ce6 and cisplatin [167]. After 660 nm light irradiation (10 mW/cm^2), the cellular reactive oxygen species (ROS) level combination treated cells was elevated. As a result of these properties, the chemo-PDT platform exhibited very potent anticancer activity against A549R cells, giving a half-maximal inhibitory concentration (IC_{50}) value for the combination therapy much lower than that of cisplatin or PDT alone [167].

1.5. Outline of the dissertation

This thesis work describes three independent research articles dealing with the use of silica-based nanoparticles (MSNs or PSilQ nanoparticles) for the effective treatment of cancer using chemo, photodynamic, gene therapy or their combination.

Chapter 1 gives as an introduction to the different types of silica-based nanoparticles, explores the basic concepts behind RNAi and photodynamic therapies, and describes different combine therapies where nanoparticles have play an important role.

Chapter 2 depicts the design, synthesis, and therapeutic performance of NANP-loaded mesoporous silica nanoparticles (NANP-MS-NPs). This project took advantages of the capability of NANPs to carry therapeutic siRNA and the ability of MSNs to transport anticancer drugs and genes. In particular, the chemotherapeutic drug (Doxorubicin) and gene therapy (anti-Bcl2 dsRNA

functionalized NANPs) were tested in this work. Feasibility of the combine therapy was evaluated in cancer cells. Overall, this chapter shows the development of an MSN based gene silencing platform and its extended applications.

Chapter 3 describes the synthesis, characterization, and cell death mechanism investigation of protoporphyrin-loaded PSilQ NPs (PpIX-PSilQ NPs). The project explores the effect of PpIX-PSilQ NPs in the cell death mechanism of cancer cells. Apoptosis and necrosis were investigated as common mechanisms; however, a special emphasis was made on ferroptosis as a novel cell death mechanism for PDT. This chapter demonstrated that cancer cells treated with PpIX-PSilQ NPs also undergo cell death through ferroptosis.

Chapter 4 depicts the synthesis, characterization, and therapeutic performance of multifunctional chlorine e6 loaded PSilQ NPs (Ce6-PSilQ NPs). This project also investigates the cell survival impact of autophagy on PDT. Combine therapy nanoparticles that includes an autophagy inhibitor (Dp44mT) were synthesized. Additionally, siRNA-based silencing of autophagy related gene (p62/SQSTM1) in co-ordination with PDT was also tested. The combine therapy with Dp44mT and Ce6-PSilQ NPs demonstrated an additive effect to improve the PDT outcome against cancer cells.

Chapter 5 provides concluding remarks on the use of silica nanoparticles for multi-therapeutic strategies with special emphasis on the projects described in Chapters 2-4; moreover, it the describes future directions for each project.

2. Combination of Nucleic Acid and Mesoporous Silica Nanoparticles: Optimization and Therapeutic Performance *In Vitro*

Citation:

Juneja R, **Vadarevu H**, Halman J, Tarannum M, Rackley L, Dobbs J, Marquez J, Chandler M, Afonin K, Vivero-Escoto JL. Combination of Nucleic Acid and Mesoporous Silica Nanoparticles: Optimization and Therapeutic Performance In Vitro. ACS Appl Mater Interfaces. 2020 Sep 2;12(35):38873-38886. doi: 10.1021/acsami.0c07106. Epub 2020 Aug 18. PMID: 32805923; PMCID: PMC7748385.

2.1. Introduction

RNA interference (RNAi) triggered by exogenous RNA duplexes has gained prominence as a therapeutic specific gene silencing mechanism, and advances have demonstrated its utility in treating complex diseases [8, 168] with already two therapies (Onpattro®[169] and Givlaari™[170]) recently approved by FDA. RNAi presents substantial opportunity as a therapeutic procedure for intractable cancers by providing a massive number of targets that conventional strategies do not render [23]. Although appealing as a therapeutic concept, clinical positioning of RNAi therapies is hindered by inefficient delivery and immunotoxicity related roadblocks. Nucleic acid nanoparticles (NANPs) present an alternative to traditional therapeutic nucleic acids, adding an additional layer of customizability [15]. These complexes are composed entirely of nucleic acids (DNA, RNA, or their analogs), and use rational design and the innate structure of nucleic acids to assume a plethora of complex three-dimensional structures [171, 172]. The limitless possibilities of these unique structures allow for highly tunable properties including size, charge, mass, thermodynamic and chemical stabilities, and multifunctionality of therapeutic nucleic acids [74, 77-79, 81, 84, 173-176] as well as the potential to regulate their immunostimulation [76, 177-185]. In addition to their roles of programmable scaffolds that coordinate therapeutic nucleic acids, NANPs have the inherent ability to be used as logic gates and biosensors, allowing for both therapeutic and diagnostic applications beyond the standards [73, 76,

186-188]. Despite the promising advantages of NANP technology, there are several issues that need to be overcome before their translation from benchtop to clinic such as poor resistance to enzymatic degradation, inability to cross biological membranes, and the potential for deleterious immune responses. Recently, our lab has demonstrated the use of polymeric and magnetic nanoparticles as carriers for NANPs' delivery and compared the stability and efficacy of various NANP/delivery complexes [189, 190]. Both platforms were shown to efficiently protect and deliver NANPs, confirming specific gene-knockdown by the released siRNA in various human cancer cell lines. However, these systems are limited to the delivery of one type of therapeutic agent – NANPs decorated with therapeutic nucleic acids and expanding the delivery platform would make this approach amenable to a broader range of challenges. Therefore, there is the critical need to develop delivery platforms that not only deliver NANPs, but also other therapeutic agents such as conventional small molecule drugs. Mesoporous silica nanoparticles (MSNPs) are an attractive alternative as a delivery vehicle for chemo, photo, and gene therapy. Several advantages have been already demonstrated for the MSNPs platform as delivery system such as biocompatibility, large surface area, and ability of multifunctionalization (e.g., therapeutic, imaging and/or targeting agents) [2, 191-194]. MSNPs are ideal carriers for siRNAs because they are efficiently internalized by mammalian cells, can be modified to protect the siRNA cargo from enzymatic degradation, and can be engineered to escape from endosomes or lysosomes to release their cargo into the cytoplasm [195-197]. Our group has previously developed silica-based nanoconstructs as a strategy for the efficient transport and delivery of siRNA [166, 178, 198]. In this project, the MSNPs shell is composed of polyethylene glycol (PEG)/polyethyleneimine (PEI) to serve as the delivery vector for NANPs. Using similar platform, we have recently shown the efficient transfection of siRNA for silencing of tenascin C in hepatic cells [198]. In addition, we

have tested the platform's potential as a delivery vector for fibrous NANPs carrying siRNA that targets the green-fluorescent protein in human breast cancer cells [178]. Nevertheless, the therapeutic performance and potential simultaneous co-delivery of NANPs with other therapeutics using MSNs has not been demonstrated yet. Herein, we report on the synthesis, characterization, optimization, and application *in vitro* of a nanoplatform that combines two promising nanotechnologies, NANPs and MSNPs (NA-MS-NP). We evaluated the immunologic, safety, and silencing performance of the NA-MS-NP system using different NANPs' shapes, including globular (cubic, cNANPs), planar (ring, rNANPs) and fibrous (fiber, fNANPs). NA-MS-NPs showed minimal immunostimulation with only the system containing globular NANPs activating the interferon (IFN) production and toll-like receptor 7 (TLR7) pathways. NA-MS-NPs carrying non-therapeutic NANPs are safe *in vitro* regardless of their shape, and the platform containing fNANPs generated the highest silencing efficiency. Finally, we evaluated the combination effect of the NA-MS-NP platform loaded with doxorubicin and targeting the anti-apoptotic *BCL2* protein in a triple negative human breast cancer (MDA-MB-231) and human melanoma (A-375) cell lines. A significant co-operative therapeutic effect between doxorubicin and NANPs against *BCL2* was observed for melanoma cells.

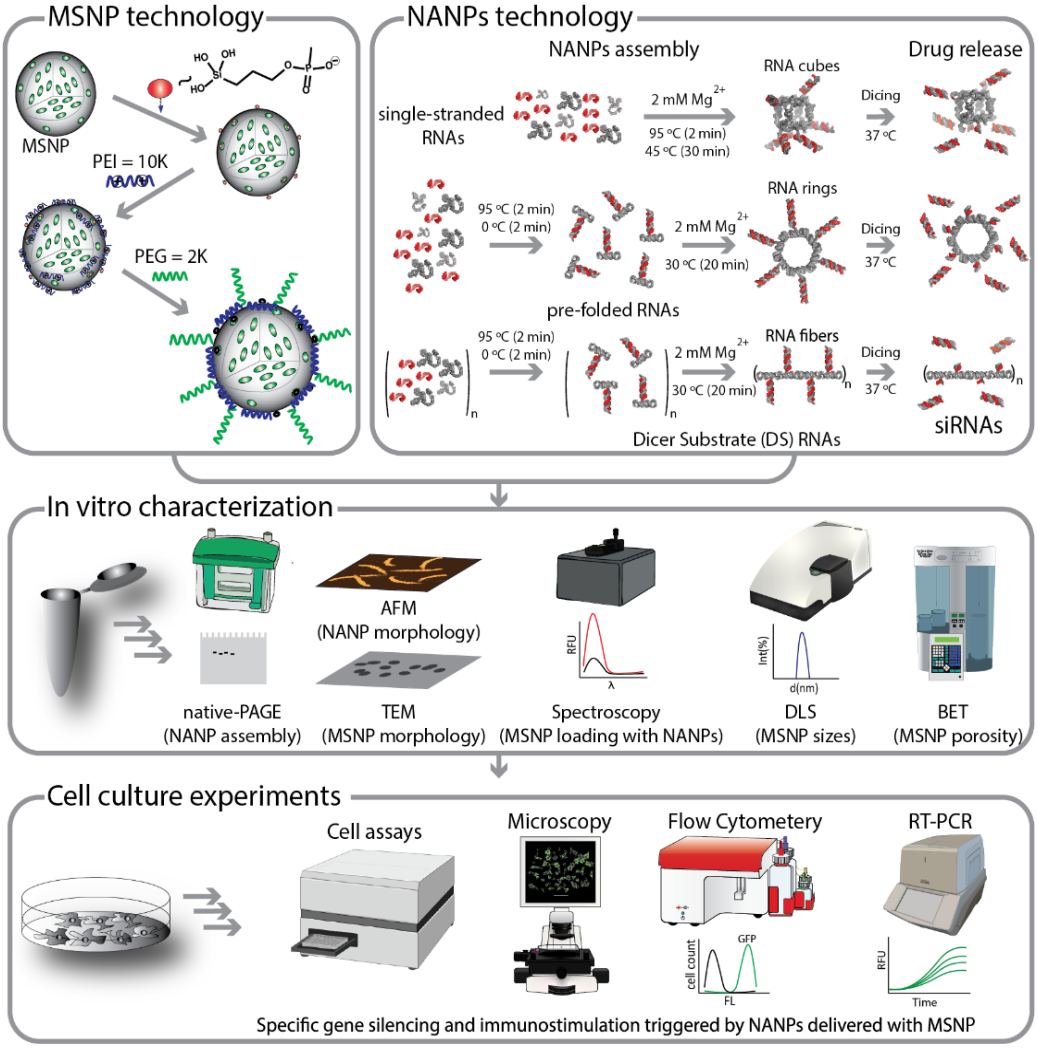

Figure 3 (**A**) Schematic representation for the fabrication of MSNPs and NANPs. The surface of MSNPs were functionalized in a multi-step approach by grafting first with phosphonate groups followed by coating with PEI and PEG polymers. Three different types of NANP materials, globular (cNANPs), planar (rNANPs) and fibrous (fNANPs) were synthesized via one-pot assembly protocols. (**B**) Different characterization techniques were used to confirm the fabrication of MSNPs, NANPs and NA-MS-NPs. (**C**) *In vitro* experiments were carried out to validate cellular uptake, gene silencing, assessment of cell growth and survival upon treatment with synthesized NA-MS-NPs.

2.2. Experimental

2.2.1. Synthesis of NANPs

RNA transcription was achieved by incubating DNA templates (containing T7 promoter regions) at 37 °C with home-made T7 RNA polymerase, 100 mM DTT, and transcription buffer (400 mM HEPES-KOH, 10 mM spermidine, 200 mM DTT, and 120 mM $MgCl_2$) for 4 h. The reaction was stopped with RQ1 DNase (Promega) for 30 minutes at 37 °C, and then purified with denaturing gel electrophoresis (urea PAGE, 8M urea, 8% acrylamide) by extracting gel slices and eluting the samples into 300 mM NaCl, 1x TBE overnight. On the following day, the samples were mixed with 2x volume of 100% ethanol and chilled to -20 °C for a minimum of 3 h. The samples were then spun at 14,000 x g for 30 min and the supernatant was disposed. An additional washing step was performed by adding 90% ethanol, and centrifuging at 14,000 x g, followed by disposing of the supernatant. Finally, the samples were dried using a SpeedVac concentrator, and then re-suspended in double deionized endotoxin free water. The concentrations were measured using a NanoDrop 2000.

The synthesis of all NANPs was completed using a “one-pot” assembly method [74]. Cubes and rings (cNANPs and rNANPs) both consist of six scaffold ssRNAs with 3’-side dicer substrate antisense extensions and six complementary dicer substrate sense strands (appendix). Fibers (fNANPs) consist of two with 3’-side dicer substrate antisense extensions and two complementary dicer substrate sense strands (appendix). For cNANPs, the strands were mixed in equimolar concentration and heated to 95 °C for two minutes, then cooled to 45 °C for another two minutes. Afterwards, 5x assembly buffer (final concentration 89 mM tris-borate, 2 mM $MgCl_2$, 50 mM KCl) was added, and the solution was incubated at 45 °C for an additional 30 min. For rNANPs and fNANPs, the strands were mixed in equimolar concentration and heated to 95 °C for two

minutes, then cooled immediately on ice (~4 °C) for another two minutes. Afterwards, the 5x assembly buffer was added, and the solution was incubated at 30 °C for 30 min. To confirm the assembly of all structures, the NANPs were run in non-denaturing native-PAGE (8%, 37.5:1) followed by ethidium bromide total staining.

2.2.2. Complexation of NA-MS-NPs

To enable NA-MS-NPs complexes formation, 0.1 mg of MSNPs were dispersed in 100 µL of 1x assembly buffer (89 mM tris-borate, 2 mM MgCl2, 50 mM KCl) followed by slow addition of either DNA/RNA duplexes or NANPs (cNANPs, rNANPs, or fNANPs) solution at a concentration of 10 µM. Additional 1x assembly buffer was added to the mixture to make a final volume of 200 µL. The final solution was mixed by pipetting several times followed by incubation for 30 min at room temperature. After that, NA-MS-NPs were separated from the dispersion by centrifugation at 8-10k rpm and re-dispersed in 100 µL of 1x assembly buffer. The optimal N/P mole ratio of 10 was used for all the NANP-MSNP complexes fabricated in this work.

2.2.3. Characterization of NANPs, MSNPs and NA-MS-NPs

Atomic force microscopy (AFM) was used to investigate the morphology of the NANPs. Freshly cleaved mica was modified with 1-(2-aminopropyl) silatrane (APS) according to established protocol.[199, 200] Five microliters of the NANPs (1 µM) was deposited onto the mica surface for two minutes. Unbound RNAs and excess salts were washed twice with 50 µL of deionized water, and the mica surface was dried with argon gas. AFM imaging was done on MultiMode AFM Nanoscope IV system (Bruker Instruments, Santa Barbara, CA) in tapping mode. Images were recorded with a 1.5 Hz scanning rate using a TESPA-300 probe, a resonance frequency of 320 Hz, and a spring constant of 40 N/m. Images were processed using FemtoScan Online (Advanced Technologies Center, Moscow, Russia).

The size and shape of the MSNPs were visualized using TEM (JEM-1230 TEM) operating at an accelerating voltage of 80 kV. The samples for TEM were prepared by dispersing the MSNPs in aqueous solution, and then deposited on a carbon-coated copper grid and air dried for at least 24 h. Particle size distributions were calculated by ImageJ based on a sample of at least 50 particles from different images taken over different quartiles. The size is reported as the average ± SD. The hydrodynamic diameter of the nanoparticles was measured by dynamic light scattering (DLS) using a Malvern Instrument Zetasizer Nano (red laser 633 nm). The equilibration time for each sample was set to 3 min; and three measurements taken on each sample. The DLS measurements were performed on dilute dispersion (0.1 mg/mL) of nanoparticles in 1 mM PBS. ζ-potential was measured in phosphate buffer solution (0.1M) using the same equipment. Thermogravimetric analysis was performed using a Mettler Toledo small furnace Thermo Gravimetric Analyzer. The thermal degradation profiles were obtained for a heating rate of 1°C/min between 25 °C to 800 °C followed by a 60 min hold at 800 °C. To determine the porous surface area and pore size the nitrogen sorption isotherms were determined using Quantachrome Instruments Nova series surface area and pore size analyzer. The Brunauer-Emmett-Teller (BET) and Barrett-Joyner-Halenda (BJH) methods were used to calculate the surface area and average pore diameter of the MSNPs, respectively.

To image the NA-MS-NPs by TEM, a drop of the NA-MS-NP suspension (approx. 5 μL) was deposited on a lacey carbon-coated copper grid. Before the sample was completely dried, a drop of the negative staining agent (Nano-W™) was added, followed by a second drop a minute later. The sample was finally air-dried on the grid. Images were taken with a JEOL JEM 2100 LaB6 TEM. Particle size distributions were calculated measuring n=50 nanoparticles using ImageJ and origin software, from different images taken at different quartiles and various magnifications.

2.2.4. Nuclease degradation protection studies

To evaluate the ability of MSNPs to protect nucleic acids from enzymatic degradation, a dsDNA carrying an Alexa Fluor 488 (Al488) fluorophore (5′ sense) and an Iowa Black Quencher (3′ anti-sense) were conjugated to MSNPs and treated with RQ1 DNase. MSNPs (0.33 mg/mL final) were mixed with the labeled dsDNA (0.8 μM final) in a solution of 30 μL total following the protocol described in section 2.2. To this solution, 3μL of RQ1 DNase was then mixed and the samples were rapidly loaded into CFX96 RT-thermocycler where the temperature was held at 37^{o} C. The relative fluorescence was measured every 30 sec for 30 min using a Bio-Rad CFX96 Real-Time System. As a positive control, DNA duplexes without MSNs in the presence of RQ1 DNase were used.

2.2.5. Competitive assay to study the release of NANPs from NA-MS-NPs

NANPs and MSNPs were complexed at a N/P ratio of 10 for 30 minutes at room temperature following the method described in section 2.2. After their attachment, aqueous heparin sulfate (Sigma) was added to the solution at a nucleic acid:heparin ratio of 1:6 w/w and incubated at 37o C for 30 minutes. The samples were analyzed via a native-PAGE as described above.

2.2.6. Immune response by THP1-Dual™ cells and HEK-Blue™ hTLR 3 or 7 cells

THP1-Dual™ cells (InvivoGen) engineered to express SEAP upon NF-κB stimulation and luciferase upon IRF stimulation were seeded at 40,000 cells per well in a 96 well-plate. The cells were then transfected with NA-MS-NPs for a final concentration of 50 nM NANPs. To measure their relative immunostimulation, 24 h post transfection, 20 μL of cell supernatant was mixed with 180 μL of prepared QUANTI-Blue™ solution (InvivoGen) and incubated for 75 minutes at 37 ^{o}C. The absorbance at 620 nm was then measured using a plate-reader to quantify NF-κB stimulation.

For IRF stimulation, 20 µL of suspension media was mixed with 50 µL of prepared QUANTI-Luc™ solution, and the luminescence was measured immediately using a plate-reader.

HEK-Blue™ hTLR 3, 7, and 9 cells (InvivoGen) were used to assess contribution from specific nucleic acid receptors in detecting NA-MS-NPs. HEK-Blue™ hTLR 3 or 7cells were plated in a 96 well plate at a density of 40,000 cells per well and allowed to adhere overnight. The next day, the cells were treated with various NA-MS-NPs (50 nM NANPs) and incubated for 24 h at 37 ^{o}C and 5% CO_2 atmosphere. Then, 20 µL of cell supernatant was mixed with 180 µL of QUANTI-Blue™ solution and incubated for 75 minutes at 37^{o} C and 5% CO_2 atmosphere. The absorbance at 620 nm was measured to quantify the activation of the respective TLRs. Positive controls such as Poly I:C and R848were used for TLR 3, and 7, respectively.

2.2.7. Cellular uptake of NA-MS-NPs

For this study, fluorescein-labeled MSNs (Fl-MSNPs) and Alexa546 labeled NANPs were used. Flow cytometry was utilized to evaluate the uptake of the Alexa546-labeled NA-Fl-MS-NPs in MDA-MB-231 cells. These cells were cultured in 24-well plate at a density of 2 x 10^4 cells per well in 0.5 mL medium and incubated for 24 h at 37 °C and 5% CO_2 atmosphere. Alexa546-labeled NA-Fl-MS-NPs (0.5 mL) were added to the cultured cells at a concentration of 30 µg/mL, and incubated for 24 h at 37 °C and 5% CO_2 atmosphere. Afterwards, the cells were washed, trypsinized and collected for analysis in the flow cytometer (BD LSR Fortessa™ cell analyzer) using mean FL-1 (Green channel), and FL-2 (Red channel) for fluorescein and Alexa546 fluorescence, respectively. Free Alexa546-labeled NANPs were also evaluated as control samples.

2.2.8. Cellular uptake and intracellular localization of Alexa546-labeled dsDNA complexed with MSNPs

A similar protocol as described in section 2.7 was used to analyze the internalization of Alexa546-labeled dsDNA-Fl-MS-NPs by flow cytometry. To evaluate the temperature-dependent mechanism of uptake associated to Alexa546-labeled dsDNA and Fl-MSNPs in MDA-MB-231 cells. These cells were cultured in 24-well plate at a density of 2 x 10^4 cells per well in 0.5 mL medium and incubated for 24 h at 37 °C and 5% CO_2 atmosphere. Alexa546-labeled dsDNA-Fl-MSNPs (0.5 mL) were added to the cultured cells at a MSNPs concentration of 10, 20 or 30 µg/mL, and incubated for 4 h at 37 °C or 4 °C and 5% CO_2 atmosphere. Afterwards, the cells were washed, trypsinized and collected for analysis in the flow cytometer (BD LSR Fortessa™ cell analyzer) using mean FL-1 (Green channel), and FL-2 (Red channel) for fluorescein and Alexa546 fluorescence, respectively. Free and Alexa546-labeled dsDNA loaded to commercial Lipofectamine 2000 (L2K) were used as controls.

For confocal laser scanning microscopy, MDA-MB-231 cells were seeded on a coverslip placed in 6-well plates at a density of 5 × 10^4 cells per well in 2 mL of DMEM and incubated at 37 °C in 5% CO_2 atmosphere for 24 h. After removing the culture medium, the cells were incubated with Alexa546-labeled dsDNA-Fl-MSNPs at MSNPs concentration of 10 µg/mL in 2 mL of complete media for 24 h. Then, cells were washed three times with cold phosphate buffer solution. The cell nuclei were stained with DAPI and incubated for 15 min at 37 °C. All microscopy images were acquired using an Olympus Fluoview FV 1000 confocal laser scanning microscope.

To determine intracellular localization, MDA-MB-231 cells were seeded on a coverslip placed in 6-well plates at a density of 5 x 10^6 cells per well in 2 mL of DMEM and incubated at 37 °C in 5% CO_2 atmosphere for 24 h. IR700-labeled dsDNA-Fl-MSNPs (2 mL) were added at a

concentration of 10 µg/mL and incubated for another 6 h at 37 ºC and 5% CO_2 atmosphere. Cells were washed twice with PBS and were further incubated with either CellLight® Early Endosomes-RFP or CellLight® Late Endosomes-RFP (Molecular Probes, Invitrogen, USA) for the labeling of early or late endosomes, respectively. First, the appropriate volume of the CellLight® reagent was calculated for the number of cells using the following formula according to the manufacturer manual (https://www.thermofisher.com/order/catalog/product/C10589#/C10589):

$$\text{Volume of CellLight® reagent (mL)} = \frac{(\text{number of cells x desired PPC})}{(1\text{x}10^8 \text{CellLight® particles/mL})}$$

Where the number of cells is the estimated total number of cells at the time of labeling, PPC is the number of particle per cell, which is 30 for this experiment, and $1\text{x}10^8$ is the number of particles per mL of the reagent. Using the previous formula, it was determined that 90 µL of either CellLight® Early Endosomes-RFP or CellLight® Late Endosomes-RFP reagent was then added to the cells in complete cell media (2 mL) and swirled gently. The cells were further incubated for 16 h at 37 ºC and 5% CO_2 atmosphere. Then, the microscopy images were acquired using Olympus Fluoview FV 100 confocal laser scanning microscope.

2.2.9. Specific gene silencing

MDA-MB-231/GFP cells expressing green fluorescent protein (GFP) (Biolabs, Inc.) for both flow cytometry and microscopy experiments were treated with NA-MS-NPs, where all NANPs were functionalized with Dicer substrate (DS) RNAs against GFP. For analysis with flow cytometry, MDA-MB-231/GFP cells were grown in 12-well plates at a concentration of 2×10^4 cells per well for 24 h at 37 °C in 5% CO_2 atmosphere. The cells were transfected with NA-MS-NPs with a NANPs concentration of 50 nM (ratio N/P=10) and incubated for 72 h at 37 °C (5% CO_2). DS RNAs targeting GFP loaded to MSNPs (dsRNA-MS-NPs) were used as control. After the

incubation time, the cells were washed with phosphate buffer solution twice to remove particles which are not taken up. Cell dissociation buffer (100 µL) (Gibco) was added to detach the cells from the culture plate. The cell suspension from each well was collected in separate tubes and gently shaken before analysis. The level of GFP expression was determined by flow cytometry (BD Bioscience) with at least 15,000 events collected and analyzed using the Cell quest software. The data is reported in terms of percentage of GFP silencing.

For microscopy analysis, MDA-MB-231/GFP cells were seeded in a 24-well plate at a density of 1 x 10^4 cells per well in 0.5 mL complete medium and incubated for 24 h at 37 °C and 5% CO_2. The cells were then exposed to NA-MS-NPs at a NANPs concentration of 50 nM (ratio N/P=10) and incubated for 72 h at 37 °C in 5% CO_2 atmosphere. DS RNAs targeting GFP loaded to MSNPs (dsRNA-MS-NPs) were used as control. The cells were washed twice with phosphate buffer solution and incubated for an additional 24 h in fresh medium. Finally, the plates were imaged to assess the GFP expression using the EVOS® FL Imaging System (inverted four-color imaging system).

2.2.10. Cytotoxicity of NA-MS-NPs

Non-functional NANPs were assembled to evaluate the cytotoxicity of NA-MS-NPs in the absence of therapeutic DS RNA. MDA-MB-231 cells were seeded at a density of 5 x 10^3 cells per well in a 96 well plate and incubated for 24 h at 37 ^oC and 5% CO_2 atmosphere. Cells were then treated with DS RNAs, and DS RNA functionalized fNA-, rNA-, cNA-MS-NPs or DOX-MSNPs at concentrations of 10, 20, 30 or 50 µg/mL and incubated for 48 h at 37 ^oC and 5% CO_2 atmosphere. Then, the cell media was removed, the treated cells were washed twice with PBS, and 100 µL of fresh complete media was added to the wells. Cells were incubated for another 24 h at 37 ^oC and 5% CO_2 atmosphere. Later, all cells were washed with PBS and replenished with 100 µL of fresh

media and 20 µL of MTS solution. Following 2.5 h of incubation at 37 ºC and 5% CO_2, the cytotoxicity was assessed by measuring the relative absorbance of the treatment groups with respect to non-exposed cells at 490 nm using a micro-plate reader. Cytotoxicity analysis for A-375 cells was carried out using a similar protocol. For A-375 cells, an initial seeding density of 2 x 10^3 cells per well and complete DMEM cell culture media was used.

2.2.11. Evaluation of combined therapy

To evaluate gene silencing efficiency in combination with chemotherapy, DOX-MSNPs were loaded with either just DS RNAs designed to target *BCL2* protein, or DS RNA functionalized fNANPs. A-375 cells were seeded at a density of 2 x 10^3 cells per well into 96 well plates and incubated for 24 h at 37 ºC and 5% CO_2 atmosphere. dsDNA or non-functional fNANPs both loaded to DOX-MSNPs were employed as control materials. A-375 cells were transfected with MSNP at a concentration of 10, 20, 30 or 50 µg/mL. After incubation for 48 h at 37 ºC and 5% CO_2, the cell media was removed, the treated cells were washed twice with PBS, and 100 µL of fresh complete media was added to the wells. After 24 h of incubation at 37 ºC and 5% CO_2 atmosphere, all wells were washed with PBS and replenished with 100 µL of fresh media and 20 µL of MTS solution. Following 2.5 h of incubation at 37 ºC and 5% CO_2, the cytotoxicity was assessed by measuring the relative absorbance of the treatment groups with respect to non-exposed cells at 490 nm using a micro-plate reader. Combination therapy was also carried out for MDA-MB-231 cells using the same protocol, but with an initial seeding density of 5 x 10^3 cells per well and RPMI cell culture media.

2.2.12. Statistical analysis

All the data in the manuscript is reported as mean ± SD unless mentioned otherwise. For the nanoparticle size analysis using TEM, 160 nanoparticles were analyzed using Image J. The

hydrodynamic size, ζ-potential, and Kaiser's test were performed in triplicates or more. The amount of DOX loaded was analyzed in triplicates using different batches of nanoparticles. Immune response experiments were carried out in triplicate, and statistical analysis was performed using a One-way ANOVA, followed a Tukey's multiple comparison test. Cellular uptake using flow cytometry was evaluated with a minimum of 5000 gated cells and quantified in triplicates. The statistical analysis was performed with One-way ANOVA using Tukey's multiple comparison test. For the cell viability studies, the GraphPad prism was used to calculate the EC_{50} values (n=3). Statistical analysis was done by One-way ANOVA using Tukey's multiple comparison test. All the statistical analysis was performed using GraphPad Prism (v8.2.0) with a *p*-value < 0.05 was considered to be statistically significant.

2.3. Results and discussion

2.3.1. Synthesis and Characterization of MSNPs

Our group and others have demonstrated the tremendous potential of MSNPs for delivering a wide variety of therapeutic and imaging agents [198, 201-203]. The versatility of this delivery platform relies on MSNPs' high surface area, tunable surface chemistry, biocompatibility and well-defined pore structure. To promote the delivery of nucleic acid-based materials, we have previously reported on a multistep synthetic approach, modifying the surface of MSNPs with polyethyleneimine (PEI) and polyethylene glycol (PEG) polymers (Error! Reference source not f ound.).[178, 198] Herein, we used this platform for delivery of NANPs. The physicochemical properties of the MSNPs were fully characterized and are shown in the supporting information (Figure 10and Table 1). As expected, the as-made MSNPs are spherical in shape with a diameter of 41 ± 3 nm (n = 50) according to TEM, a hydrodynamic diameter of 73 ± 1 nm (n=5) and a highly negative surface charge of -50 ± 4 mV (n=5). The MSNPs presented a high surface area of 638 m^2/g and pore diameter of 2.2 nm as determined using the nitrogen sorption isotherms. After

functionalization with PEI and PEG polymers, a dramatic shift in the ζ-potential value from negative (-50 ± 4 mV) to positive (+14 ± 1 mV) values was observed. In addition, a slight increase in the hydrodynamic diameter to 118 ± 10 nm (n=5) was also determined. Both thermogravimetric analysis and Kaiser's test confirmed the presence of the polymers with a weight loss of 20.3 ± 1.5 and 28.1 ± 0.9 % wt, and the presence of primary amine groups with amounts of 1861 ± 545 and 1207 ± 327 nmol/mg, after modification with PEI and PEG, respectively (Table S1).

To prepare the DOX-loaded PEG-PEI-MSNPs, DOX molecules were loaded into non-functionalized MSNPs under acidic conditions, which enhance the electrostatic interaction between non-functionalized MSNPs and DOX molecules. Non-functionalized MSNPs' surface is negatively while DOX is positive charged due to the primary amine group in its structure [204]. This approach resulted in a high DOX loading amount of 16.7±1.6 % wt (n=3) for the final DOX-loaded PEG-PEI-MSNPs, which is similar to what has been previously reported for MSNP materials [205]. Unless stated otherwise, PEG-PEI-MSNPs and DOX-loaded PEG-PEI-MSNPs are referred as MSNPs and DOX-MSNPs in the rest of the manuscript for simplicity.

2.3.2. Optimization of nucleic acids binding to MSNPs, pH-dependent release and enzymatic stability

All initial optimization experiments in solution were performed using Alexa 488-labeled DNAs rather than NANPs. The binding between nucleic acid material and MSNPs relies on the electrostatically interaction between the negatively charged phosphate groups (P) of nucleic acids and positive amine groups (N) on the MSNPs [178, 206]. First, we determined the optimal N/P ratio for our system by gel electrophoresis varying the N/P ratio from 1 to 40 (Error! Reference s ource not found.). Fluorescently labeled with Alexa488 dye DNA duplexes (DNA-Alexa488) that are not complexed with MSNPs migrated freely through the gels, while the mobility of the

duplexes electrostatically complexed with MSNPs was limited. We found out that for N/P ratios larger than 10, there is a complete binding between the DNA-Alexa488 and MSNPs as indicated by the lack of the free DNA-Alexa488 band. This result was further corroborated by the lack fluorescence signal in the supernatant after centrifugation of the DNA-Alexa488-MSNP material (Error! Reference source not found.). Previous reports have shown that N:P ratios > 8 for this M SNP platform provide optimal electrostatic interactions [206]. Therefore, we chose to use N/P ratio of 10 for this work since it shows strong binding and maximum loading of nucleic acids.

We also investigated the MSNPs ability to protect nucleic acids from enzymatic degradation using a fluorescently quenched duplexes assembled form DNA strands tagged with an Alexa 488 fluorophore at the 5'-side and complementary strands with Iowa black quencher on the 3'-side. These DNA duplexes are treated with RQ1 DNase. If there is not enzymatic protection, the degradation of the duplexes and further spatial separation of fluorophore and quencher would lead to activation of the fluorescence signal. However, in the absence of degradation, the close proximity of the Iowa Black completely would quench the fluorescence of Alexa 488 [189]. The DNA duplexes were complexed with MSNPs and treated with RQ1 DNase (Error! Reference s ource not found.). MSNPs successfully protected DNA duplexes from DNase degradation, as evidenced by the minimal increase in fluorescence. Control experiment with only DNA duplexes treated with DNase showed a dramatic increase in fluorescence signal.

Our data demonstrated that MSNPs can efficiently complex with and protect nucleic acids from nuclease degradations. Nevertheless, it is also important to show that the nucleic material is released once it reached the desired site inside the cells. We hypothesized that the release of nucleic acids from MSNPs can be triggered by lowered pH such as the one found in endosomes or lysosomes. To test this hypothesis, we evaluate the release of DNA-Alexa488 loaded to MSNPs

in buffer solutions at pH 5.2, and 7.4. There is a remarkable release of about 60% of DNA-Alexa488 compare with the sample at pH 7.4 (Figure 11. pH-dependent release of DNA-Alexa488 from MSNPs. The release of DNA-Alexa488 was measured in solution by using a fluorescence spectrometer at two different pHs; pH = 7.4 (circles) and pH = 5.2 (squares).. This pH-responsive release can be explained by the disruption of the interaction of the phosphonate groups in the backbone of the RNA or DNA and the amine groups in the PEI polymer in the presence of protons at acidic pH [64].

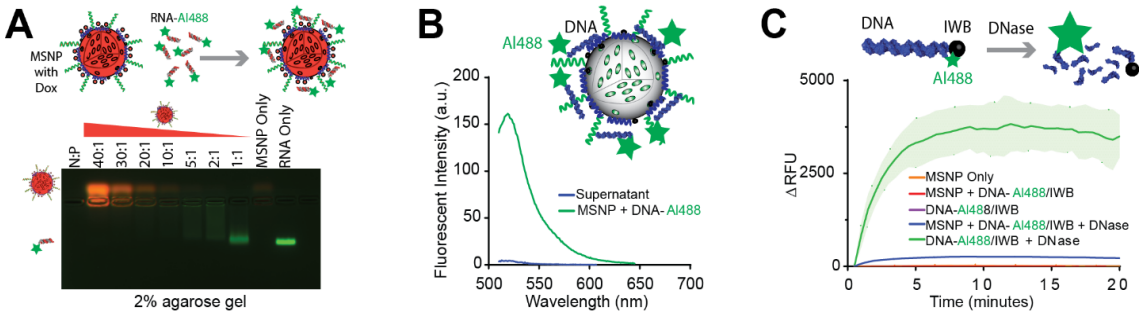

Figure 4 **A**) Gel electrophoresis shows the binding effect of DNA-Alexa 488 to MSNP at various N:P ratios. The presence of the green band indicates the decrease in electrostatic complexation of DNA-Alexa488 to the MSNPs at lower N/P ratios. (**B**) The strong binding at N/P = 10 was corroborated by analyzing the DNA duplexes remaining in the supernatant solution after the binding with MSNs. (**C**) The treatment of DNA duplexes with quenching pair Alexa488 and Iowa Black with and without MSNP conjugation confirms the protection from nuclease activity.

2.3.3. Formation of NA-MS-NPs and NANPs' integrity studies upon their release from NA-MS-NPs.

Three representative NANPs (globular cNANPs, planar rNANPs, and fibrous fNANPs) were all synthesized via one-pot assembly under the same buffer conditions. cNANPs are formed via intermolecular Watson-Crick base pairing [176], while rNANP and fNANP designs both are assembled via initial intramolecular formation of Watson-Crick base pairings that facilitates magnesium-dependent intermolecular kissing loop interactions (Error! Reference source not f

ound.) [84]. Each structure has the capacity to carry several DS RNAs against a specific target gene such as GFP or *BCL2*. The assembly of the different NANPs are achieved by mixing equimolar amounts of the constituent strands and undergoing a process of heating and cooling, outlined in detail in the methods section. To assess the formation of the NANPs, AFM and gel electrophoresis were carried out, demonstrating their morphologies and monodispersity. AFM micrographs clearly showed the formation of each anticipated NANP, while the single band observed in native-PAGE demonstrated their monodisperse assemblies.

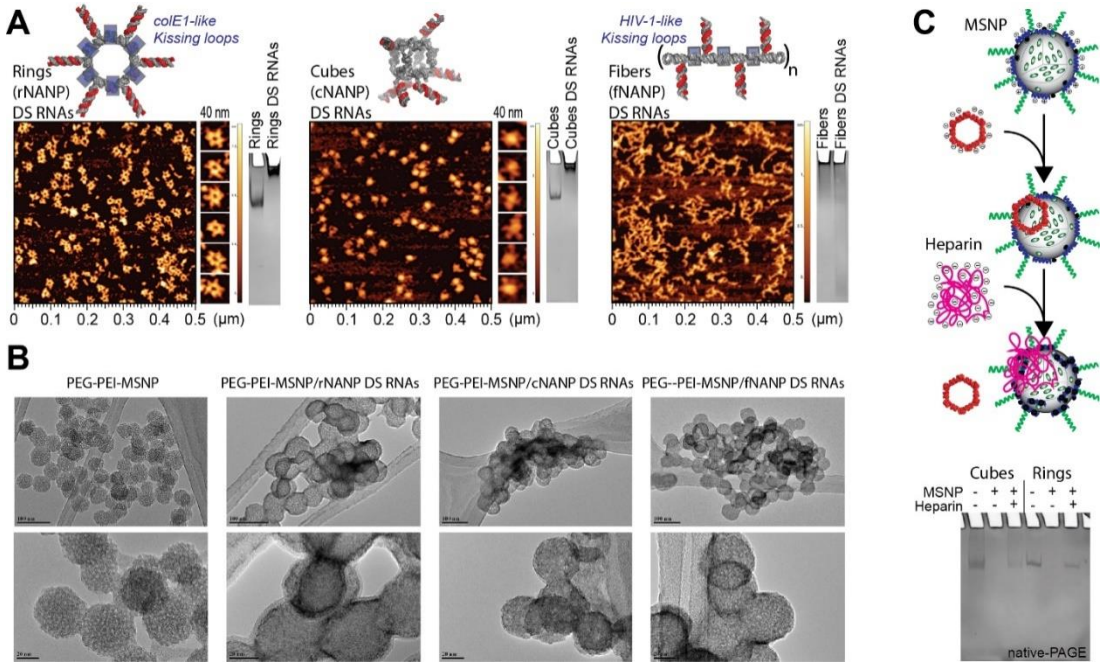

Figure 5 Physical characterization of both NANPs and MSNPs. (**A**) Atomic force microscopy images and electro mobility shift assays of GFP functionalized NANPs demonstrates uniformity and morphology. (**B**) Transmission electron microscopy images demonstrate size, shape and distribution of NA-MS-NPs. (**C**) Complexation and release of NANPs from MSNP demonstrate by competitive binding with heparin. NANPs are released and stay intact post complexation with MSNPs.

The formation of the NA-MS-NPs relies on the electrostatic interaction between the negative charge associated to the phosphate backbone of NANPs and the positive charged of MSNPs. Based on our optimization experiments described above, we maintained the same N/P ratio of 10 for the assembly of NA-MS-NPs. TEM was used to visualize the NA-MS-NPs after staining the material with a solution of organo-tungstate. Tungstate based compounds are commonly used for negative stain EM which is accessible and convenient approach. The negative staining works by heavy metal compounds embedded in a thin layer of biological macromolecule likes proteins or nucleic acids highlighting their morphology [207, 208]. The TEM images for the NA-MS-NPs depicted a denser surface from the negative staining as an indication of the presence of NANs on the surface of the MSNs (Error! Reference source not found.). However, we were not able to distinguish the d ifferent morphology or shapes of the NANs which can be attributed the drawbacks of negative stain EM. Though negative stain EM is easy, the drying process involved can cause collapse or denaturing of the biological or macromolecules.

To determine the ability of MSNPs to deliver intact NANPs, a heparin competition assay was carried out in order to disrupt the electrostatic interactions between NANPs and MSNPs [189]. The highly negative charge of heparin outcompetes the NANPs binding with MSNPs, resulting in the release of the NANPs. Gel electrophoresis was used to evaluate the release of the NANPs (Error! Reference source not found.). The native-PAGE image clearly shows that the bands, c orresponding to either cNANPs or rNANPs after their release from MSNPs in the presence heparin, travel similar distance as the original NANs. This is a clear demonstration that MSNPs can effectively carry and release NANPs without affecting their morphology. Due to the size of fNANPs and their inability to enter the gel, they were not evaluated using this technique.

2.3.4. Immunostimulation by NA-MS-NPs *in vitro*

Recently we discovered that when NANPs are used with the delivery agent, the dimensionality, size, and composition of NANPs dictate their immunostimulatory properties [76, 177, 178, 181, 182, 189]. Therefore, we characterized the immunostimulatory effects of NA-MS-NPs. We used human monocytic cells, THP1-Dual (InvivoGen), engineered to express secreted alkaline phosphatase (SEAP) and luciferase in response to NF-kB and IRF stimulation, respectively. We also utilized HEK-Blue hTLR cells to address the contribution from specific receptors. These model systems present a simple and straightforward way to measure immune signaling from nucleic acids. Poly I:C and R848, known inducers of immune response, were used as positive control in these studies. We observed differential immune stimulation for MSNPs carrying different NANPs containing DS RNA against GFP. Specifically, MSNPs modified with cNANPs elicited the greatest response in THP1-Dual cells in the IRF pathway, exhibiting the highest production of interferons, consistently with previous results (Error! Reference source not found.) ADDIN EN.CITE [181, 189]. Both TLR3 and 7 are responsible for RNA detection in endosomal compartments, with TLR3 recognizing dsRNA and TLR7 ssRNA detection [209]. Our data show that all the NA-MS-NPs generated a response in HEK-Blue hTLR3 cells; however, MSNPs by themselves also initiated an immune response, which was not predicted with this cell line (Error! Reference source not found.). Upon contacting the manufacturer, it was determined that the HEK-Blue hTLR3 cells express (lower) endogenous TLR5, which can be activated by PEI [210, 211]. Furthermore, the NF-kB stimulation in the THP1-Dual cells may be also attributed to the presence of PEI on the nanoparticles (Error! Reference source not found.). Moreover, cNA-MS-NPs were able to activate TLR7, while the other NA-MS-NPs were not (Error! Reference source not found.). Additionally, these cNA-MS-NPs were demonstrated to provoke an interferon response (Error! Reference source not found.). This particular performance of cNANPs has already been observed

for polymeric delivery agents [212]. These results demonstrate that not only the immune response of NANPs is important to be determined, but also the one associated to the carrier can have a major impact in the overall immune response of the nanocomplex. Interestingly, this concept also adds an additional layer of customizability for the therapeutic activity of NA-MS-NPs. Wherein the NANPs can be used as both a traditional therapeutic (RNAi, aptamer, anti-sense, etc.) and as an adjuvant, MSNPs can also be customized to produce its own additive immune response.

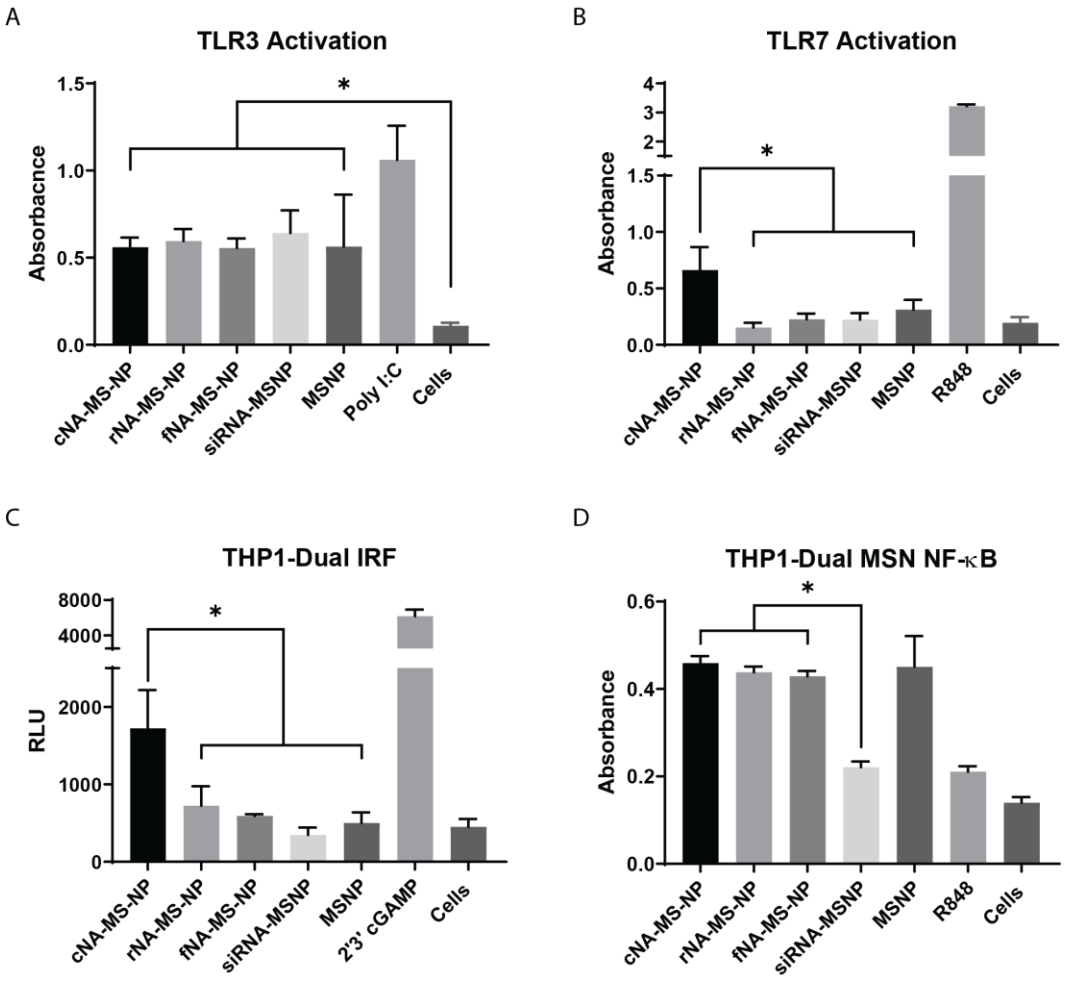

Figure 6 Immunostimulatory properties of MSNs carrying GFP functionalized NANs treated in (**A)** HEK-Blue hTLR3, (**B)** HEK-Blue hTLR 7, (**C**) HEK-Blue hTLR 9, and (**D)** THP1-Dual cells demonstrate the cellular pathways which are activated by different NANPs. Statistics: One-way ANOVA using Tukey's multiple comparison test was performed between different groups determine the statistical difference. * $p \leq 0.05$.

2.3.5. Cellular uptake and co-localization studies for dsDNA loaded MSNPs

Our group and others have already demonstrated the ability of MSNPs to deliver nucleic acid materials [178, 195, 198]. Nevertheless, in this work for the first time, we are showing the delivery of NANPs with different shapes using MSNPs. To carry out these experiments NANPs and MSNPs were labeled with Alexa546 and fluorescein, respectively. Flow cytometry was used to determine the efficiency of internalization of the Alexa546 labeled-NA-Fl-MS-NPs in MDA-MB-231 cancer cells. The flow cytometry data show comparable internalization of all NA-Fl-MS-NPs regardless of the NANPs' morphology (Error! Reference source not found.). These results show t hat MSNPs can efficiently deliver NANPs regardless of the shape. Previous reports have shown that in the case of polymeric nanoparticles the shape is an important factor for their internalization [213]. However, it appears that this is not the case for the NA-MS-NPs, most likely due to the strong electrostatic interaction between both nanoparticles. Control experiments of NANPs in the absence of delivery vector show no internalization of nanoparticles (Figure 12).

We performed a deeper investigation on the cellular uptake and co-localization of MSNPs in MDA-MB-231 cells. For cost efficiency, these experiments were carried out using Alexa 546-labeled dsDNA rather than NANPs. Similar to the results found for NA-MS-NPs, the flow cytometry data showed that both the Alexa546-labeled dsDNA and Fl-MSNPs are efficiently internalized by MDA-MB-231 cells (Error! Reference source not found.). Control experiments w ith Alexa546-labeled dsDNA in the absence of Fl-MSNPs showed no internalization of DNA (Figure 12). These data were further confirmed by confocal microscopy. Confocal images show the presence of Fl-MSNPs (green) and Alexa546-labeled dsDNA (red) inside the cells. It is clear after merging the green and red channels with the DIC that most of the Alexa546-labeled dsDNA loaded Fl-MSNs (yellow) has been internalized by the cells (Error! Reference source not found.). T

his is convincing evidence that the MSNPs successfully carried the dsDNA across the cell membrane. In addition, we detected spots in the micrographs where the green and red fluorescence do not completely overlap, which can be indicative that dsDNA has been released from the MSNs (Error! Reference source not found.). As described above, we hypothesize that the main m echanism to account for the release of dsDNA is the displacement of dsDNA driven by acidic pH in organelles associated to the endolysosomal pathway.[63]

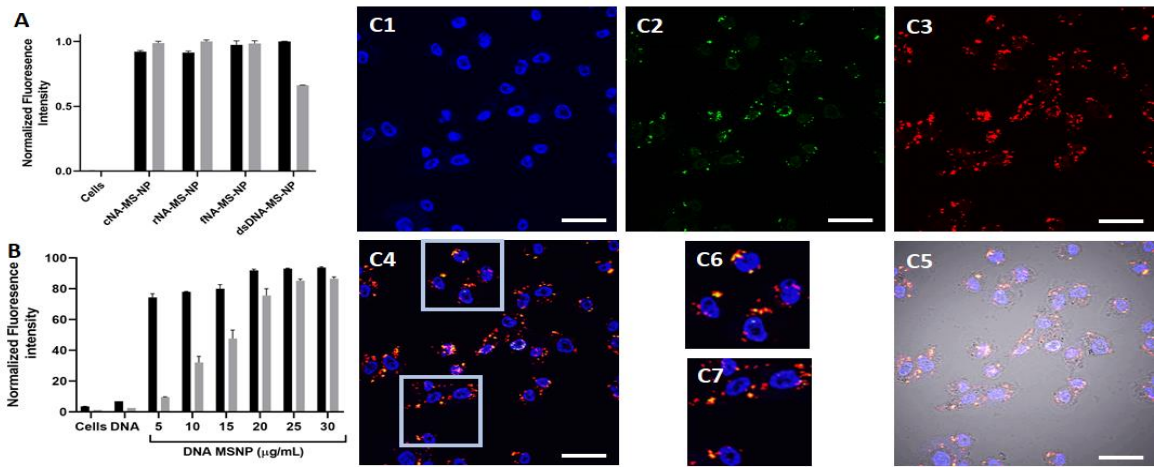

Figure 7 MDA-MB-231 cells uptake of Alexa546-labeled NANPs or dsDNA loaded to MSNPs. (**A)** Mean fluorescence intensity associated to NANPs (gray) and MSNPs (black) obtained from flow cytometry experiments. (**B)** Mean fluorescence intensity associated to dsDNA (gray) and MSNPs (black) at different concentration of the nanoparticle complex obtained from flow cytometry experiments. (**C**) Confocal micrographs of MDA-MB-231 cells inoculated with Alexa546-labeled dsDNA loaded MSNPs (10 µg/mL). The cell nuclei are observed in the blue channel after staining with Hoechst 33342 (**C1**). The fluorescence in the FITC (green) channel (**C2**) indicates the localization of MSNPs. The fluorescence in the TRITC (red) channel shows the presence of Alexa546-labeled dsDNA (**C4**). The merged micrographs (**C4** - **C5**) show the colocalization and localization of Alexa546-labeled dsDNA loaded MSNs inside MDA-MD-231 cells. The insets in (**C6** - **C7**) clearly demonstrates the release of Alexa546-labeled dsDNA from MSNPs. Scale bar = 40 µm.

MSNPs have already been shown to be internalized through endocytic mechanisms and to be trafficked by the endolysosomal pathway [214]. A temperature-dependent experiment was carried out to evaluate whether the internalization of Alexa546-labeled dsDNA loaded Fl-MSNPs follow an energy-dependent or passive mechanism. Supporting Figure 13 shows that the internalization of Alexa546-labeled dsDNA loaded Fl-MSNPs is reduced under low temperature (4 °C) when compared to physiological temperature (37 °C), thus confirming that these complexes are indeed uptaken by the cells through endocytic pathways [215].

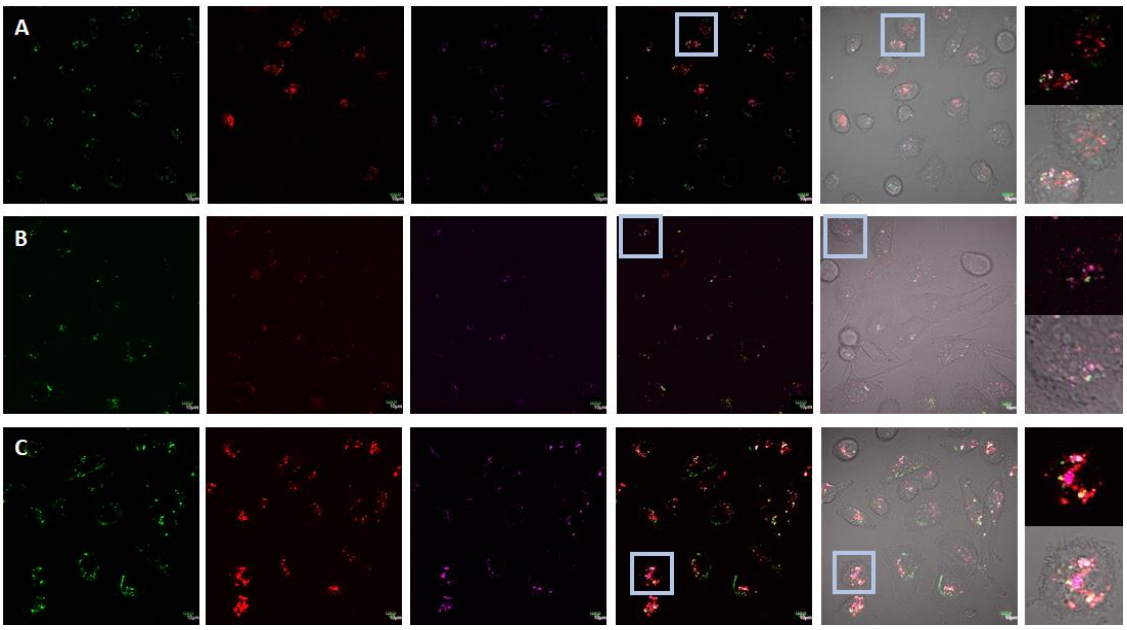

Figure 8 Confocal micrographs of MDA-MB-231 cells inoculated with NIR700-labeled dsDNA loaded MSNPs (10 µg/mL). The fluorescence in the FITC (green) channel indicates the localization of MSNPs. The fluorescence in the TRITC (red) channel shows the labeling of organelles; CellLight® Early Endosomes-RFP (**A**), CellLight® Late Endosomes-RFP (**B**) or Lysotracker (**C**). The presence of Alexa546-labeled dsDNA is indicated in purple. The merged micrographs show the co-localization and localization of IR700-labeled dsDNA loaded MSNPs inside MDA-MD-231 cells. The insets clearly demonstrate the escape from endosomes/lysosomes and the release of IR700-labeled dsDNA from MSNPs. Scale bar = 10 µm.

To determine the colocalization of dsDNA duplexes loaded to MSNPs inside the cells; early-, late-endosomes or lysosomes were stained using CellLight® Early Endosomes-RFP, CellLight® Late Endosomes-RFP or Lysotracker, respectively. For this experiment, to avoid any overlap with the organelle markers, DNA duplexes were labeled with IR700 fluorophore (IR700-labeled dsDNA). Confocal micrographs showed that Fl-MSNPs are co-localized with early-, late-endosomes or lysosomes (Error! Reference source not found.). However, a major localization is o bserved with lysosomes (Error! Reference source not found.). In several instances, nanoparticles were not co-localized with any of the organelles as an indication of endolysosomal escape, most likely due to the so-called "proton sponge effect" associated to PEI polymers [63]. Moreover, similar to what was shown above, the release of IR700-labeled DNA duplexes is also corroborated in these experiments. Overall, these results corroborate that the nanoconstructs are efficiently endocytosed by the MDA-MB-231 cells, transport through the endolysosomal pathway, escape from endosomes/lysosomes most likely due the "proton sponge effect" and deliver DNA duplexes in the cytoplasm.

2.3.6. Specific gene silencing

We have previously demonstrated that NANPs functionalized with DS RNA against GFP silence its expression when transfected into GFP expressing human cell lines using magnetic nanoparticles or polymeric micelles [189, 190]. In this work, we assessed the NA-MS-NPs silencing efficacy using MDA-MB-231 cell line modified to overexpress GFP. NANPs were functionalized with RNA duplexes against GFP. In these experiments, NA-MS-NPs depicted silencing-dependent efficacy based on the shape of NANPs (Figure 9). The fNANPs and DS RNAs showed the higher knock-down efficiency against GFP with 54% and 68% silencing, respectively when compared to other NA-MS-NPs (One-way ANOVA, $p < 0.05$). In the case of cNANPs and rNANPs, a silencing

efficiency of 40% and 33% was determined, respectively. Previous report using polymeric micelles or magnetic nanoparticles as vectors did not show differences in GFP silencing efficiency depending on NANPs' dimensionality [189, 190]. Considering that based on our results all NA-MS-NPs internalize the cells with a similar efficiency and all NANPs carry equal number of DS RNAs; the different in silencing found in this study is most likely due to differences in electrostatic binding between NANPs and MSNPs, which can influence the intracellular release of NANPs. We hypothesize that cNANPs and rNANPs are likely to have stronger bindings to MSNPs than fNANPs or DS RNAs. A stronger electrostatic binding will result in fewer released NANPs, which will impact their processing by Dicer and final knock-down of the target protein.

Fluorescence microscopy was further used to confirm the results obtained by flow cytometry. Our negative control experiment depicted a higher population of MDAMB-231/GFP cells expressing green fluorescent protein, which is silenced after transfection with NA-MS-NPs (Figure 9). The fluorescence micrographs clearly showed a significant reduction in the expression of GFP after transfecting MDA-MB-231/GFP cells with NA-MS-NPs. Based on our experimental results, fNANPs are the most efficient for gene silencing with reduced immunostimulatory effect.

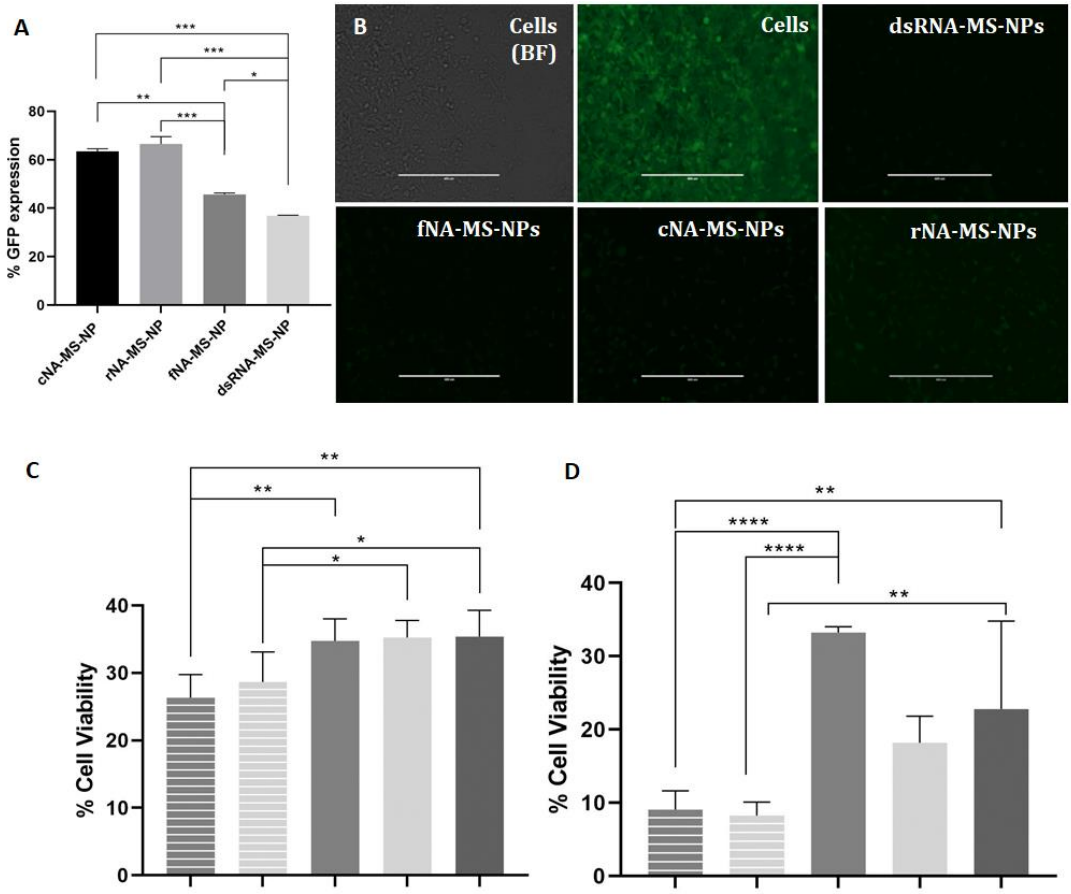

Figure 9. (**A**) Percent GFP expression post treatment with DS RNA using MSNPs obtained using flow cytometry. (**B**) Fluorescence microscopy imaging for GFP gene silencing in MDA-MB-231 cells/GFP. Controls cells bright field and no treated. Cells treated with anti-GFP NA-MS-NPs. Scale bar = 400 µm. Cytotoxicity results of anti-*BCL2*-fNA-DOX-MS-NPs (gray/stripes), anti-*BCL2*-RNA-DOX-MS-NPs (light gray/stripes), non-functionalized fNA-DOX-MS-NPs (gray), non-therapeutic dsDNA-DOX-MS-NPs (light gray), and DOX-MS-NPs (dark gray) at a concentration of 10 µg/mL for A-375 cells (**C**) and 50 µg/mL for MD-MB-231 cells (**D**). Statistics: One-way ANOVA was performed between different groups determine the statistical difference. ****$p \leq 0.0001$, ***$p \leq 0.001$, ** $p \leq 0.01$, and * $p \leq 0.05$.

2.3.7. Combination therapy using fNA-MS-NPs

Despite all the advantages of using NANPs for RNAi therapy, only few reports of co-delivery of NANP/chemotherapeutic drugs have been published [75, 216, 217]. Among different nanocarriers, MSNPs have shown remarkable features for the efficient co-delivery of siRNA/chemotherapeutic drugs. This platform has been successfully administered as effective gene delivery vector in different cancer models [154, 218]. As a proof of principle to demonstrate the therapeutic ability of the NA-MS-NPs for combined therapy, silencing of anti-apoptotic gene *BCL2* in combination with doxorubicin (DOX) were used. *BCL2* is an attractive oncogene target because it activates the cellular antiapoptotic defense, which is one of the main mechanisms of cancer resistance [219]. Inhibition of *BCL2* enhances the sensitivity of cancer cells to standard therapies [220], hence the importance of this gene as a potential therapeutic target in various human cancers. DOX, which is part of the family of anthracyclines drugs, mainly acts as DNA intercalator that triggers apoptosis. Therefore, by combining NANPs that target the synthesis of *BCL2* protein with DOX, we anticipate having a major impact on cell survival [221-223].

To evaluate the combination therapy of DOX and RNAi inducers targeting *BCL2* using the NA-MS-NPs, MDA-MB-231 and A375 cell lines were used. MDA-MB-231 is a triple negative breast cancer cell line and A375 is a skin cancer cell line that overexpresses *BCL2* [224, 225]. First, to rule out the possibility of any cytotoxicity associated to non-functionalized NANPs loaded to MSNPs, the viability of these cells in the presence of the nanoconstructs was tested using the MTS assay. The results showed a slight cytotoxicity due to carrier at the tested concentrations, but no differences in growth inhibition for the non-functional NA-MS-NPs as an indication that the NANPs do not play a role on the cytotoxic of both cell lines (Figure 14). In addition, we also evaluated any possible synergy between the non-functionalized NANPs with DOX-MSNPs. The

cell viability results showed that the growth inhibition is only associated to therapeutic effect of DOX but does not dependent on the NANPs (Figure 15).

Our viability results demonstrated that there is no cytotoxic effect associated to the dimensionality of NANPs. Therefore, the fNANs, that have reduced immunostimulation effect and higher gene silencing as compared with other NANPs, were selected for the combined therapy. To test the combination therapy of *BCL2* silencing and DOX in A375 and MDA-MB-231 cell lines, fNANPs containing DS RNAs against *BCL2* were engineered and complexed to DOX-MSNPs. As control experiments for this study, anti *BCL2* DS RNAs, non-therapeutic DNA duplexes, and non-functionalized fNANPs complexed with DOX-MSNPs were used. The viability results in both cell lines depict a concentration-dependent cytotoxic effect associated to the nanoparticles. It is observed that DOX is the main factor on the therapeutic outcome against both cell lines (Figure 16). Previous reports using the same combination have shown the similar trend [161, 223]. Nevertheless, in a closer look at specific concentrations we found additive effects induced by anti-*BCL2*-fNA-DOX-MS-NPs for both cell lines. In the case of A-375 cells at the concentration of 10 µg/mL, there is an evident co-operative effect between DOX and anti-*BCL2*-fNANPs as shown in Figure 9. The cytotoxic effect of the anti-*BCL2*-fNA-DOX-MS-NP platform was higher than DOX-MSNs, non-therapeutic DS DNA with DOX-MSNPs or non-functionalized fNA-DOX-MS-NPs. In a similar way, MDA-MB-231 cells at a concentration of 50 µg/mL, it was observed a better cytotoxic effect for anti-*BCL2*-fNA-DOX-MS-NPs as compared to DOX-MSNPs, non-therapeutic dsDNA-DOX-MSNPs or non-functionalized fNA-DOX-MS-NPs (Figure 9). For both cell lines, the DS RNA targeting *BCL2* loaded to DOX-MSNPs showed similar cytotoxicity than anti-*BCL2*-fNA-DOX-MS-NPs. Our results demonstrated that the shape, either globular, planar or fibrous, of NANPs does not have an impact on the cytotoxicity of neither bare nor DOX-loaded

MSNPs. Nevertheless, when DS RNA or anti-*BCL2*-fNANPs are loaded to DOX-MSNPs, a clear additive effect with the chemotherapeutic drug is observed at specific concentrations.

2.4. Conclusion

We have evaluated and optimized the use of MSNPs as efficient carrier for the delivery of NANPs. We demonstrate that the silencing efficacy and immunostimulatory activity is significantly impacted by the shape of NANPs. fNANPs have reduced immunostimulation effect and the higher gene silencing efficacy as compared with planar or globular NANPs. Nevertheless, the cytotoxicity of the NA-MS-NPs is not affected by the morphology NANPs. fNANPs were used as a prove of principle to evaluate the combination of siRNA targeting *BCL2* and the chemotherapeutic drug, doxorubicin. An additive effect was determined for both A375 and MDA-MB-231 cell lines. The present results suggest that this novel platform provides great potential for combinatorial therapy of cancer.

2.5. Appendix - Combination of Nucleic Acid and Mesoporous Silica Nanoparticles

Extended Materials and Methods

Tetraethylorthosilicate (TEOS, 98%), cetyltrimethylammonium bromide (CTAB), 3-aminopropyl triethoxysilane (APTES), 3-(trihydroxysilyl)propyl methylphosphonate monosodium salt solution 50 wt % in H_2O (THPMP), trimethylamine, ninhydrin, fluorescein isothiocyanate (FITC), heparin sulfate and rhodamine B isothiocyanate (TRITC) were purchased from Sigma-Aldrich (St Louis, MO, USA). Polyethylene imine (PEI, branched; MW 10kDa) was purchased from Alfa Aesar (Haverhill, MA, USA). Methoxy-Polyethylene-glycol succinimidyl carboxymethyl ester (mPEG-SCM, 2kDa) was obtained from Creative PEGworks. Doxorubicin was obtained from LC Laboratories. All DNA (Alexa 488/546/IR700) and short RNA oligos were

purchased through Integrated DNA Technologies (IDTDNA.com) and longer RNAs entering the composition of NANPs were synthesized via *in vitro* run-off T7 transcription as described later. Assembly buffer (89 mM Tris-borate, 2 mM $MgCl_2$, 50 mM KCl) was used to aid in the folding of all NANPs.

Synthesis of MSNPs

Synthesis of negatively charged MSNPs

The non-functionalized MSNPs were synthesized according to our previously published sol-gel procedure.[178, 198] Briefly, 0.78 g of CTAB was dissolved in a solution of 21.6 mL water, and 3.32 mL ethanol. To this, 0.1 mL diethylamine (0.4 mM) was added and, the solution was heated to 60 °C. TEOS (2.19 mL) was added dropwise into the aqueous solution of CTAB, and the reaction was allowed to run for 18 h at 60 °C to obtain as-made MSNPs. Later, the surface of MSNPs was modified by grafting 3-(trihydroxysilyl)propyl methylphosphonate monosodium salt (THPMP) to impart negative surface charge on the material. For phosphonate modification, THPMP (150 µL diluted in 0.5 mL water) was added dropwise to the as-synthesized MSNPs and stirred for 6-8 h at 60 °C. The surfactant CTAB, was then removed from the pores using an acidic solution of methanol (37% w/v), which was heated to 60 °C with stirring for 10 h. This process was repeated a second time to make sure that all the surfactant was removed.

Synthesis of fluorescein labeled MSNPs

To incorporate fluorescein molecules in the MSNPs, fluorescein-modified silane was first synthesized and added to the negatively charged MSNP dispersion in ethanol as described below. To synthesize fluorescein-modified silane, 7.3 µL of APTES was mixed with 3.3 mg of fluorescein

isothiocyanate (FITC) in 0.6 mL of dry DMF and stirred for 2 h under at room temperature and nitrogen atmosphere. The fluorescein-modified silane was then mixed with a dispersion of MSNPs (150 mg) in 20 mL of ethanol at 60^{o}C and stirred overnight for 15 h. The fluorescein labeled MSNPs (Fl-MSNPs) were then centrifuged and washed with methanol at least three times.

Synthesis of doxorubicin (DOX)-loaded MSNPs (DOX-MSNPs)

To synthesize DOX-MSNPs, 20 mg of MSNPs were suspended in 1.0 mL of water with a pH of 4.5 adjusted using 0.02 M HCl solution. To this suspension, 1.0 mL of 5 mg/mL doxorubicin hydrochloride (DOX-HCl) aqueous solution was added and stirred at room temperature for 48 h. The DOX loaded MSNPs were collected by centrifugation at 13,000 rpm for 15 min and washed three times with water to remove any unencapsulated DOX. The synthesized DOX-MSNPs were resuspended in ethanol for storage. To measure the DOX loading capacity of nanoparticles; the supernatants from the loading and washing steps were collected. The pH of these solutions was adjusted to pH 4.5 using 0.02 M HCl and analyzed at 490 nm using a Varian Cary 50 Bio UV-Visible spectrophotometer. The amount of DOX loaded was then calculated using a calibration curve obtained upon the same experimental conditions.

Synthesis of PEG-PEI-modified MSNPs

To carry out the surface modification of the nanoparticles, MSNPs or DOX-MSNPs were coated with PEI polymer (MW=10 KDa) to switch the surface charge from negative to positive values. To perform PEI coating, 10 mg of negatively charged MSNPs were dispersed in an ethanolic solution (5 mL) containing 5 mg of PEI. After stirring for 2 h at room temperature, PEI-coated particles were washed with ethanol. Finally, the surface of PEI-MSNPs was further functionalized with mPEG-SCM (MW=2K) through a conjugation reaction. To carry out the PEGylation, 10 mg of PEI-MSNPs were dispersed in 5 mL of dried acetonitrile. To this dispersion, a solution of

mPEG-SCM (3 mg/mL) in 1 mL of dried acetonitrile was added. After stirring for 24 h, the final PEG-PEI-MSNPs were washed with ethanol, and stored in the same solvent. Unless stated otherwise, PEG-PEI-MSNPs and DOX-loaded PEG-PEI-MSNPs are referred as MSNPs and DOX-MSNPs in the rest of the manuscript for simplicity.

Quantification of Chemically available primary amines using the Kaiser's test:

The Kaiser's test was used to quantify primary amines on the surface of PEG- and PEI-MSNPs [226]. Sodium acetate buffer (2 M, 100 mL) was prepared by dissolving 14.11 g sodium acetate in 86 mL distilled water followed by addition of 14 mL glacial acetic acid (2 M). The pH of the resulting solution was adjusted to 5.4 using HCl. The ninhydrin solution was prepared by dissolving 0.5 g ninhydrin in 10 mL of ethanol. To carry out the Kaiser's assay; 100 μL of the prepared sodium acetate buffer (pH 5.4) and 70 μL ninhydrin solution were mixed together in a glass vial. Then 10-20 μL of the NP sample was added. The tubes were heated up to 70 °C in an oil bath for 10-15 min. After cooling, 3 mL of ethanol-water mixture in a ratio of 3:2 (vol/vol) was added to each tube. Finally, the absorbance of each solution was measured at 570 nm by a UV-Vis spectrophotometer. The result for each batch is calculated based on the average of four measurements. The final data is presented as the average ± SD for three batches.

Cell culture:

MDA-MB-231, a human invasive TNBC cell line; and A-375, a human melanoma cell lines were purchased from American Type Culture Collection (ATCC). MDA-MB-231 cells were cultured in RPMI 1640 medium (supplemented with 10% FBS, 1% pen-step) at 37 °C with 5% CO_2 atmosphere. A-375 cells were cultured in DMEM (supplemented with 10% FBS, 1% pen-step) at 37 °C with 5% CO_2 atmosphere. The culture media was changed every other day. All cell cultures

were maintained in 25 cm^2 or 75 cm^2 cell culture flasks and the cells were passaged at 70-80% confluency every 2-4 days. The cell survival was tested by the CellTiter 96® AQueous Assay (MTS assay). The absorbance was measured at a wavelength of 490 nm in a plate reader Multiskan FC.

Sequences used in this project:

DNA Cube

5’ GGCAACTTTGATCCCTCGGTTTAGCGCCGGCCTTTTCTCCCACACTTTCACG

5’ GGGAAATTTCGTGGTAGGTTTTGTTGCCCGTGTTTCTACGATTACTTTGGTC

5’ GGACATTTTCGAGACAGCATTTTTTCCCGACCTTTGCGGATTGTATTTTAGG

5’ GGCGCTTTTGACCTTCTGCTTTATGTCCCCTATTTCTTAATGACTTTTGGCC

5’ GGGAGATTTAGTCATTAAGTTTTACAATCCGCTTTGTAATCGTAGTTTGTGT

5’ GGGATCTTTACCTACCACGTTTTGCTGTCTCGTTTGCAGAAGGTCTTTCCGA

RNA Ring

5’ GGGAACCGUCCACUGGUUCCCGCUACGAGAGCCUGCCUCGUAGC

5’ GGGAACCGCAGGCUGGUUCCCGCUACGAGAGAACGCCUCGUAGC

5’ GGGAACCGCGUUCUGGUUCCCGCUACGAGACGUCUCCUCGUAGC

5’ GGGAACCGAGACGUGGUUCCCGCUACGAGUCGUGGUCUCGUAGC

5’ GGGAACCACCACGAGGUUCCCGCUACGAGAACCAUCCUCGUAGC

5’ GGGAACCGAUGGUUGGUUCCCGCUACGAGAGUGGACCUCGUAGC

RNA Fiber

5’ GGGAAUCCAAGGAGGCAGGAUUCCCGUCACAGAAGGAGGCACUGUGAC

5’ GGGAACGUAAGCCUCCAACGUUCCCGGAUGCUAAGCCUCCAAGCAUCC

GFP Cube

5’GGCAACUUUGAUCCCUCGGUUUAGCGCCGGCCUUUUCUCCCACACUUUCACGUU

CGGUGGUGCAGAUGAACUUCAGGGUCA

5’GGGAAAUUUCGUGGUAGGUUUUGUUGCCCGUGUUUCUACGAUUACUUUGGUCU

UCGGUGGUGCAGAUGAACUUCAGGGUCA

5’GGACAUUUUCGAGACAGCAUUUUUUCCCGACCUUUGCGGAUUGUAUUUUAGGU

UCGGUGGUGCAGAUGAACUUCAGGGUCA

5’GGCGCUUUUGACCUUCUGCUUUAUGUCCCCUAUUUCUUAAUGACUUUUGGCCU

UCGGUGGUGCAGAUGAACUUCAGGGUCA

5’GGGAGAUUUAGUCAUUAAGUUUUACAAUCCGCUUUGUAAUCGUAGUUUGUGUU

UCGGUGGUGCAGAUGAACUUCAGGGUCA

5’GGGAUCUUUACCUACCACGUUUUGCUGUCUCGUUUGCAGAAGGUCUUUCCGAU

UCGGUGGUGCAGAUGAACUUCAGGGUCA

GFP Ring

5’GGGAACCGUCCACUGGUUCCCGCUACGAGAGCCUGCCUCGUAGCUUCGGUGGUG

CAGAUGAACUUCAGGGUCA

5’GGGAACCGCAGGCUGGUUCCCGCUACGAGAGAACGCCUCGUAGCUUCGGUGGU

GCAGAUGAACUUCAGGGUCA

5’GGGAACCGCGUUCUGGUUCCCGCUACGAGACGUCUCCUCGUAGCUUCGGUGGUG

CAGAUGAACUUCAGGGUCA

5’GGGAACCGAGACGUGGUUCCCGCUACGAGUCGUGGUCUCGUAGCUUCGGUGGU

GCAGAUGAACUUCAGGGUCA

5’GGGAACCACCACGAGGUUCCCGCUACGAGAACCAUCCUCGUAGCUUCGGUGGUG

CAGAUGAACUUCAGGGUCA

5’GGGAACCGAUGGUUGGUUCCCGCUACGAGAGUGGACCUCGUAGCUUCGGUGGU

GCAGAUGAACUUCAGGGUCA

GFP Fiber

5’GGGAAUCCAAGGAGGCAGGAUUCCCGUCACAGAAGGAGGCACUGUGACUUUGG

UGGUGCAGAUGAACUUCAGGGUCA

5’GGGAACGUAAGCCUCCAACGUUCCCGGAUGCUAAGCCUCCAAGCAUCCUUUGGU

GGUGCAGAUGAACUUCAGGGUCA

GFP Sense

5’ pCAUUAACGAGCUGCUUAAUGACGA

“p” denotes phosphate on the 5’

GFP Sense with Alexa 488

5’ pCAUUAACGAGCUGCUUAAUGACGA-Alexa488

GFP Anti-Sense

5’ CGGUGGUGCAGAUGAACUUCAGGGUCA

Supporting Figures

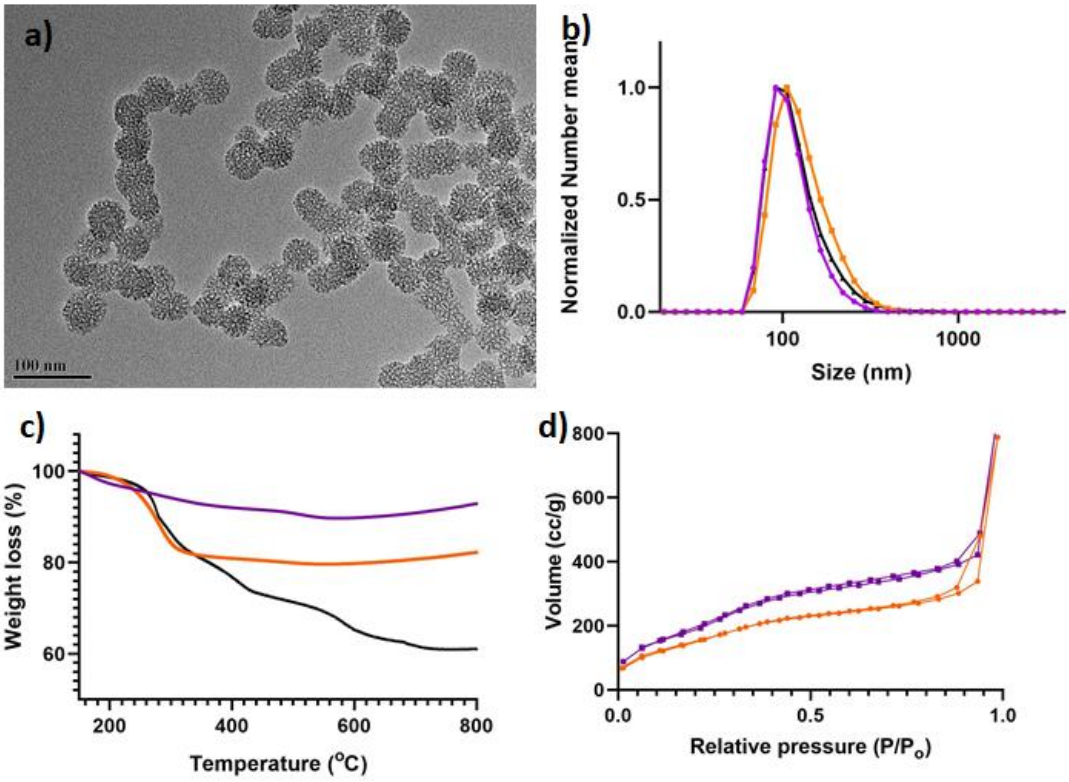

Figure 10. (a) TEM image of as-made MSNPs (diameter = 41 ± 3 nm; n = 50). (b) DLS plots and (c) TGA graphs for as-made MSNPs (purple), PEI-MSNPs (orange), and PEG-PEI-MSNPs (black (d) N_2 isotherms for as made MSNPs (purple) and PEI-MSNPs (orange).

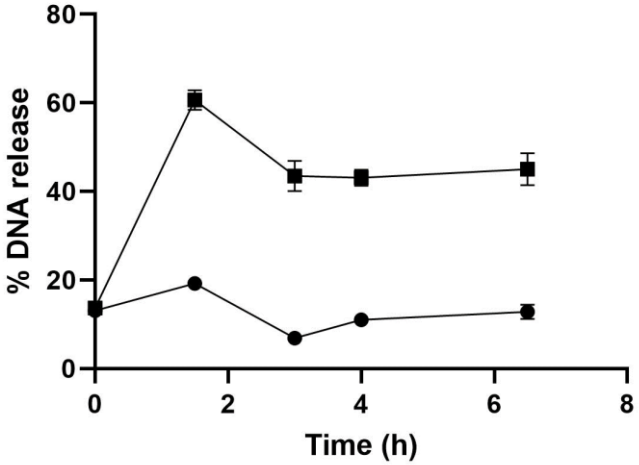

Figure 11. pH-dependent release of DNA-Alexa488 from MSNPs. The release of DNA-Alexa488 was measured in solution by using a fluorescence spectrometer at two different pHs; pH = 7.4 (circles) and pH = 5.2 (squares).

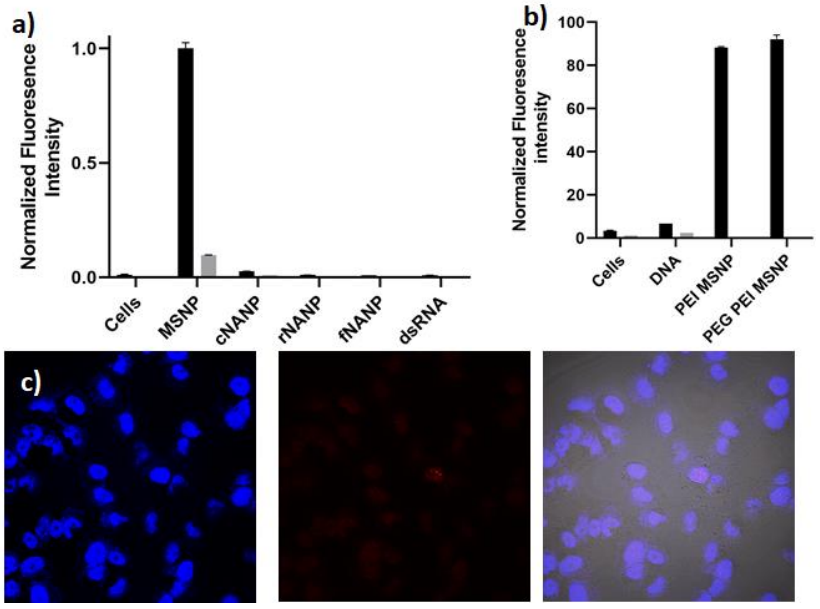

Figure 12. (a) Normalized fluorescence intensity associated to NANPs (gray) and MSNPs (black) obtained from flow cytometry experiments. (b) Normalized fluorescence intensity associated to dsDNA-Alexa546 (gray) and MSNPs (black) obtained from flow cytometry experiments. (c)

Confocal micrographs of MDA-MB-231 cells inoculated with Alexa546-labeled dsDNA. The cell nuclei are observed in the blue channel after staining with Hoechst 33342. The fluorescence in the TRITC (red) channel shows the presence of Alexa546-labeled dsDNA. The merged micrographs show no internalization of Alexa546-labeled dsDNA inside MDA-MD-231 cells.

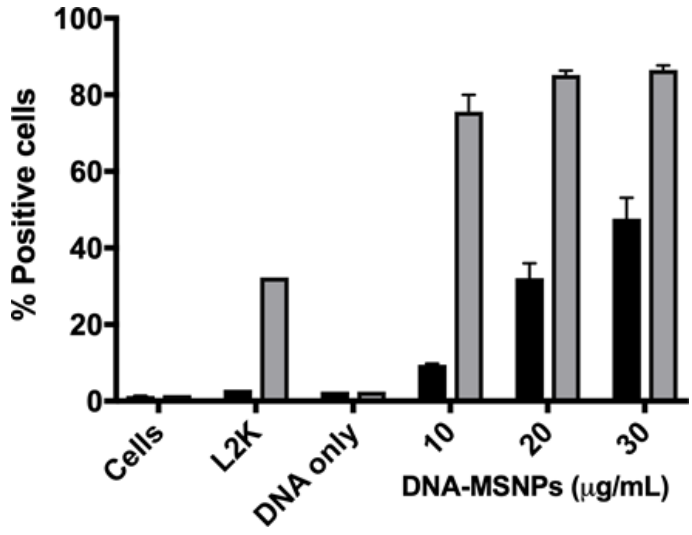

Figure 13. Temperature-dependent internalization of internalization of Alexa546-labeled dsDNA loaded Fl-MSNPs at 4 °C (black) and 37 °C (gray).

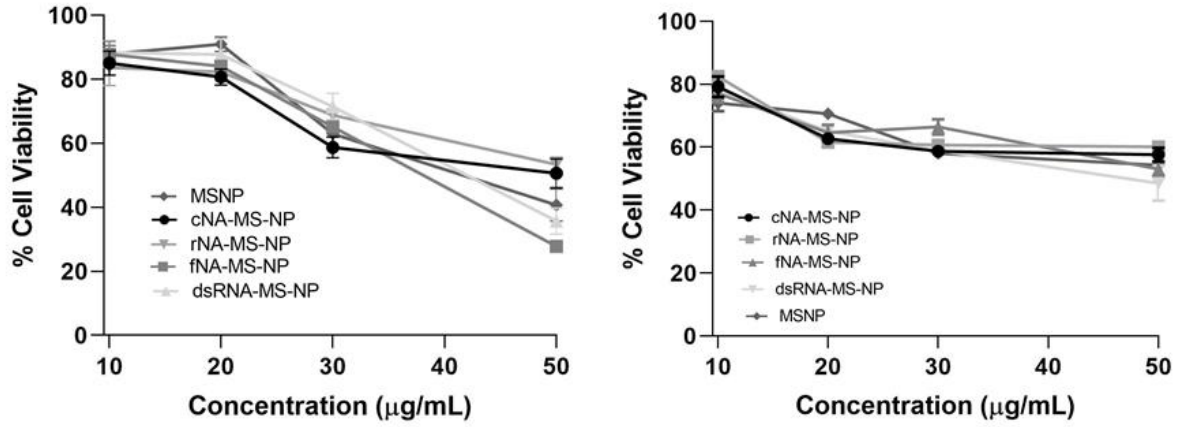

Figure 14. Cytotoxicity results of NA-MS-NPs, dsRNA-MS-NPs and MSNPs for A-375 (left) and MDA-MB-231 (right) cells.

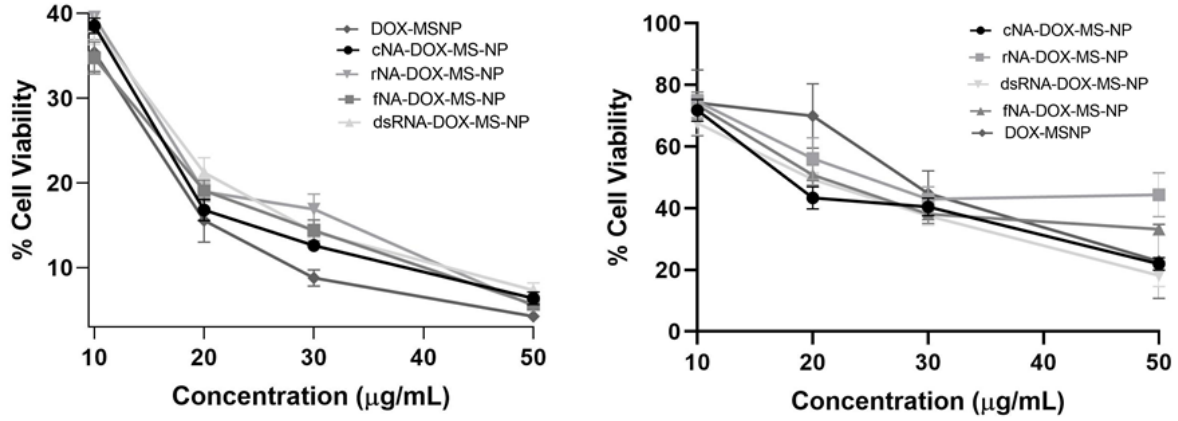

Figure 15. Cytotoxicity results of non-functionalized NA-DOX-MS-NPs, dsRNA-DOX-MS-NPs and DOX-MSNPs for A-375 (left) and MDA-MB-231 (right) cells.

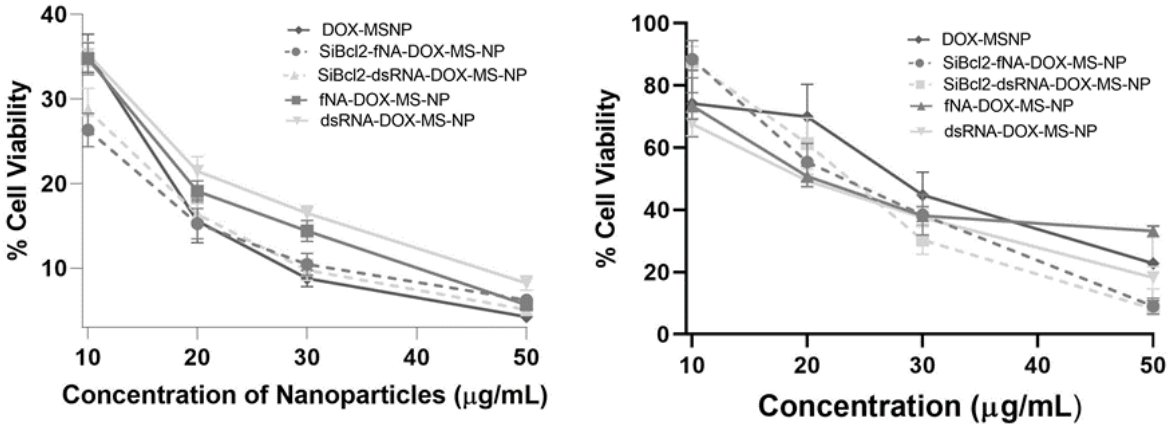

Figure 16. Cytotoxicity results of *BCL2*-functionalized fNA-DOX-MS-NPs, *BCL2*-RNA-DOX-MS-NPs, control NPs and DOX-MSNPs for A-375 (left) and MDA-MB-231 (right) cells.

Supporting Tables

Table 1. Structural properties of the MSNP materials.

Material	DLS Size (d, nm) (n=5) (PDI)	ζ- potential (mV) (n=5)	Weight loss (%wt)	Kaiser's test (nmol amines/mg)
As-made MSNPs	73 ± 1 (0.14 ± 0.01)	-50 ± 4	8.0 ± 0.8	NA
PEI-MSNPs	96 ± 1 (0.11 ± 0.02)	+19 ± 2	20.3 ± 1.5	1861 ± 545
PEG-PEI-MSNPs (MSNPs)	118 ± 10 (0.25 ± 0.02)	+14 ± 1	28.1 ± 0.9	1207 ± 327

	Surface area (m^2/g)	Pore Volume (cm^3/g)	Pore Diameter (nm)
As-made MSNPs	637.9	2.3	2.2

3. Light-Activated Protoporphyrin IX-Based Polysilsesquioxane Nanoparticles Induce Ferroptosis in Melanoma Cells

Citation:
Vadarevu H, Juneja R, Lyles Z, Vivero-Escoto JL. Light-Activated Protoporphyrin IX-Based Polysilsesquioxane Nanoparticles Induce Ferroptosis in Melanoma Cells. Nanomaterials (Basel). 2021 Sep 7;11(9):2324. doi: 10.3390/nano11092324. PMID: 34578640; PMCID: PMC8470003.

3.1. Introduction

Photodynamic therapy (PDT) is a minimally invasive treatment for cancer and other diseases. PDT uses non-toxic photosensitizers (PSs) that, upon activation with light of a specific wavelength in the presence of cellular oxygen, trigger a photochemical process leading to the generation of reactive oxygen species (ROS) [227]. The efficiency of ROS production in PDT is governed by effective activation of the PS internalized by cells of interest. The ROS generated in PDT can consume intracellular antioxidant substances like glutathione (GSH). Most PSs form unstable aggregates in aqueous media due to hydrophobicity and often require the use of organic solvents to aid their solubility. The application of PSs for PDT is heavily dependent on aqueous stability, and the past decade has seen many efforts directed towards developing stable formulations of such molecules in water [90]. The use of nanoparticles (NPs) for physical or chemical encapsulation of hydrophobic PSs has been widely explored as an alternative approach to overcome these issues. Nanoplatforms, such as liposomes, polymeric systems, inorganic materials, and silica-based nanoparticles, have demonstrated their effectiveness as PS carriers [228, 229]. Our group pioneered the use of polysilsesquioxane (PSilQ) materials as an efficient platform for the delivery of protoporphyrin (PpIX) for in-vitro and in-vivo treatment of cancer. We demonstrated the advantage of using a redox-responsive PpIX-PSilQ platform to enhance the PDT effect in vitro [230-232]. This approach was used to develop a degradable PpIX-PSilQ platform for the effective PDT treatment of triple negative breast cancer (TNBC) in vivo [233]. Furthermore, we assessed the multi-modal capability of PpIX-PSilQ NPs by combining PDT, chemotherapy, and gene

silencing in the same platform for the treatment of TNBC [166]. Herein, we report the study of the cell death mechanisms associated with PpIX-PSilQ nanoparticles.

Apoptosis and necrosis are well characterized cell death mechanisms related to PDT [85]. Autophagy is a commonly reported cellular program in response to PDT that affords both cell survival and cell death depending on the cell type and degree of oxidative damage [234, 235]. A newly discovered cell death mechanism is ferroptosis, which has shown to enhance the treatment efficacy of traditional chemo- and radiotherapy. Recently, ferroptosis has also been studied as an alternative mechanism of PDT to kill cancer cells [98]. We previously showed that apoptosis is the main mechanism linked to the phototoxicity of PpIX-PSilQ nanoparticles [233]; however, there is no study reporting the impact of ferroptosis in the PDT effect of this platform. Ferroptosis is an iron-dependent cell death that is caused by extreme peroxidation of cellular phospholipids and is a commonly reported response to tumor radiation therapy [236, 237]. Excess hydroxyl radicals resulting from iron-catalyzed Fenton reactions can potentially initiate oxidative degradation of lipids in cell membranes by free-radical chain mechanism and subsequently cause cell death [237]. A recent study showed that GSH depletion associated to PDT could directly increase the accumulation of lipid peroxidation and enhance the ferroptosis effect [238, 239]. Herein, we study the cell death mechanisms associated with PpIX-PSilQ nanoparticles, with special emphasis on ferroptosis (Figure 17).

We synthesized PpIX-PSilQ nanoparticles for the purpose of this work. The physicochemical properties of this platform are similar to our previously reported systems [166, 233]; however, this platform does not have stimuli-responsive features. Phototoxicity, generation of ROS, and cellular internalization were also confirmed using a malignant melanoma cell line, A375. Cell death mechanisms were investigated using different assays, including Annexin V apoptosis, glutathione

peroxidase activity, and lipid peroxide probe C-11 BODIPY. The results show that PpIX-PSilQ nanoparticles in the presence of light produce cell death in A375 cells, which is correlated to apoptosis and ferroptosis. The role of ferroptosis in phototoxicity of the PpIX-PSilQ system was further confirmed using a ferroptosis inhibitor. These results demonstrated that ferroptosis is an important cell death mechanism associated to the PDT performance of PpIX-PSilQ nanoparticles.

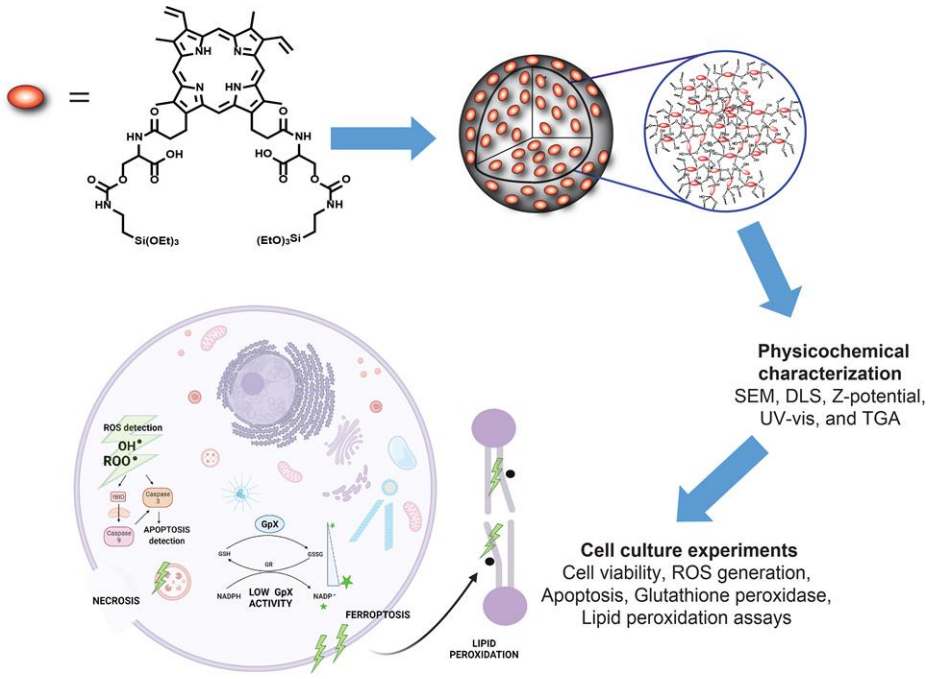

Figure 17. PpIX-PSilQ NPs are fabricated using the PpIX silane derivative (4) as a building block through microemulsion method. The physicochemical properties of the nanoparticles, such as SEM, DLS, ζ-potential, UV−vis, and TGA, are evaluated. The in-vitro performances, including the phototherapy, ROS generation, and internalization of PpIX-PSilQ NPs, are determined using A375 cells. The cell death mechanisms associated with the phototherapeutic outcome of PpIX-PSilQ NPs, like apoptosis, necrosis, and ferroptosis, against A375 cells are studied.

3.2.Experimental

3.2.1. Cell Culture

A375 cells were purchased from American Type Culture Collection (ATCC® CRL-1619™, Manassas, Virginia, USA). The cells were cultured in DMEM with 10% FBS, 1% penicillin/streptomycin, 1% GlutaMAX, and 1% NEAAs at 37 °C with 5% CO_2 atmosphere.

3.2.2. Stock Solutions for In-Vitro Experiments

For the treatment of cells with PpIX, 5 mM primary stock solution was freshly prepared in complete DMEM with 1% *v*/*v* of DMSO. A primary stock of Hoechst 33342 at a concentration of 4 mM was prepared in deionized water containing 1% *v*/*v* DMSO and stored at −20 °C, which was diluted to 20 µM in complete DMEM for staining cells. Then, 10 mM DCFH-DA primary stock was prepared in DMSO and was diluted to 10 µM in complete DMEM before addition to cells. Then, 20 mM stock solution of Ferrostatin-1 was prepared in DMSO and was diluted to 2 µM in complete DMEM for cell treatment. A primary stock of PpIX-PSilQ NPs in a concentration equivalent to 200 µM of PpIX was prepared in complete DMEM by ultrasonication for 5 min and diluted for cell treatment.

3.2.3. Synthesis of PpIX-PSilQ Nanoparticles

The direct microemulsion method was used to synthesize the PpIX-PSilQ NPs *[166]*. The following procedure was used: 0.22 g of AOT (0.495 mmol) was added to 10 mL of nanopure water under gentle stirring for 30 min at room temperature. Then, 0.4 mL of n-butanol was added. Once the solution became clear, 0.1 mL of cyclohexane (oil phase) was added. The final mixture was stirred for 15 min to give a single-phase transparent solution. To this mixture, a solution of

PpIX silane precursor (4, see Scheme S1) (1.6 mg) in 0.1 mL of 1:2 dimethyl sulfoxide (DMSO)/dimethyl formamide (DMF) mixture (*v*/*v*) was added dropwise under continuous stirring at room temperature. To enhance the solubility and condensation process of compound 4, 0.1 mL of aqueous ammonia (28%) followed by 0.2 mL of an aqueous solution of NaOH (2 M) was added to the solution. The reaction mixture was stirred for 48 h at room temperature. The nanoparticles were obtained by disrupting the microemulsion with an excess of acetone, which afforded the precipitation of the PpIX-PSilQ NPs. The final nanoparticles were collected by centrifugation (13,000 rpm for 10 min), followed by sequential washing steps with acetone, ethanol, and DMF to remove any unreacted reagents. The washed PpIX-PSilQ NPs were stored in ethanol at 4 °C.

3.2.4. Determination of Intracellular Reactive Oxygen Species (ROS)

A375 cells were seeded in six-well plates at a density of 5×10^4 cells/well in 2 mL of complete DMEM and incubated at 37 °C in 5% CO_2 atmosphere. After 24 h, PpIX-PSilQ nanoparticles (50 or 100 µM equivalent amount of PpIX) or free PpIX (10 or 50 µM) were added to the wells in fresh media. Followed by 48 h of incubation, the media was removed, and cells were washed with Dulbecco phosphate buffer solution (DPBS). Cell permeable ROS probe (DCFH-DA, 10 µM) was added to the cells in serum free media, and cells were incubated for 30 min at 37 °C and 5% CO_2. After removing the media, the cells were washed with DPBS and irradiated (630 nm, 24.5 mW/cm^2) for 20 min. Subsequently, cells were harvested using trypsin and analyzed for green fluorescence associated with the oxidation product, 2',7'-dichlorofluorescein (DCF), using a BD LSRFortessa flow cytometer. Untreated cells were also incubated with the ROS probe; the data were utilized as the negative control.

3.2.5. Evaluation of Intracellular ROS Using Confocal Microscopy

A375 cells were seeded in a six-well plate containing glass coverslips at a density of 5×10^4 cells/well in 2 mL of complete DMEM and incubated at 37 °C in 5% CO_2 atmosphere for 24 h. After media removal, 50 µg/mL of PpIX-PSilQ NPs (equivalent to 25 µM PpIX) were added to the wells in fresh media and incubated for 48 h. Cells were washed once with DPBS, followed by the addition of 10 µM of ROS probe DCFDA in serum free media, and incubated for 30 min. Next, cells were washed once with DPBS and irradiated (630 nm, 24.5 mW/cm^2) for 20 min. Coverslips were then mounted on to glass slides using adhesive spacers after adding 30 µL of DPBS to the slide. Images were acquired using Olympus FluoView 1000 confocal fluorescence microscope. A375 cells inoculated with PpIX-PSilQ nanoparticles (not irradiated), and untreated cells in the presence of the ROS probe were imaged as controls.

3.2.6. Cellular Uptake of PpIX-PSilQ Nanoparticles

To evaluate the cellular uptake of PpIX-PSilQ NPs in A375 cells, the cells were seeded in 24-well plates at a density of 2×10^4 cells/well in 500 µL of complete DMEM and incubated for 24 h at 37 °C in 5% CO_2 atmosphere. PpIX-PSilQ NPs or PpIX was added to the wells in fresh media at concentrations corresponding to 25 or 50 µM of PpIX. After 24 h of incubation, media was removed, cells were washed twice with DPBS, and cells were harvested with trypsin. Collected cells were resuspended in 200 µL of DPBS and analyzed for red channel fluorescence using a BD LSR Fortessa flow cytometer. Untreated cells were employed as negative controls.

To further evaluate the cellular uptake of PpIX-PSilQ NPs in A375 cells using CLSM, the cells were seeded in a six-well plate with glass slides at a density of 5×10^4 cells/well in complete DMEM. After 24 h of incubation at 37 °C in 5% CO_2 atmosphere, the media was removed, and 50 µg/mL of PpIX-PSilQ NPs were added to the wells in fresh media. The cells were incubated for

another 24 h, the cell media was removed, and cells were washed twice with DPBS. Cells were stained with 20 µM of Hoescht 33342 nuclear staining solution and incubated for 20 min at 37 °C. After removal of the dye-containing media, coverslips were washed with DPBS and then mounted on to glass slides using adhesive spacers. Images were acquired using Olympus FluoView 1000 confocal fluorescence microscope at 40 × magnification.

3.2.7. In Vitro Evaluation of PDT Triggered Apoptosis

A375 cells were seeded in six-well plates at a density of 5 x 10^4 cells/well in complete DMEM. Followed by 24 h of incubation at 37 °C in 5% CO_2 atmosphere, PpIX-PSilQ NPs (equivalent concentrations of PpIX of 50 or 100 µM) or PpIX (10 or 50 µM) were added to the wells in fresh media. After 48 h of incubation, cell media was removed, and the cells were washed once with DPBS prior to irradiation with red light (630 nm, 24.5 mW/cm^2) for 20 min. Fresh media was replenished, and cells were incubated for additional 24 h at 37 °C in 5% CO_2 atmosphere. Treated cells were harvested with trypsin and tested using Annexin V staining (FITC Annexin V Apoptosis Detection Kit, BD Pharmingen™, San Jose, California, USA) as per manufacturer's protocol to determine apoptotic cell population. Annexin V antibody was added to the cells dispersed in 0.1 X binding buffer, followed by incubation for 20 min at room temperature. Cells were pelletized by centrifugation (2500 rpm, 5 min), and unbound Annexin V was removed. After excess antibody removal, 0.1 X binding buffer was used to wash cells once and for redispersion. Cells were co-stained with a vital dye (SYTOX™ Blue dead cell stain, Invitrogen™, (Waltham, Massachusetts, USA)) and classified into live, FITC+/dead, and FITC+/live populations using a BD LSR Fortessa flow cytometer. Untreated cells and non-irradiated samples were employed as negative controls.

3.2.8. Inhibition of Ferroptosis

The phototoxicity of PpIX-PSilQ NPs was evaluated in the presence of a ferroptosis inhibitor (Ferrostatin-1) using MTS assay. A375 cells were seeded in 96-well plates at a density of 2×10^3 cells/well in 100 µL of complete DMEM and incubated at 37 °C in 5% CO_2 atmosphere for 24 h. After cell media removal, PpIX (10–200 µM) or PpIX-PSilQ NPs (equivalent concentrations of PpIX of 10–250 µM) were added in fresh media to the cells. Followed by 48 h of incubation, cells were washed once with 100 µL of DPBS and irradiated with red light (630 nm, 24.5 mW/cm2) for 20 min. Treated cells were replenished with 100 µL of fresh media containing 2 µM Fer-1 (0.01% *v*/*v* DMSO) and incubated for additional 24 h at 37 °C in 5% CO_2 atmosphere. Control dark experiments were conducted in parallel with PpIX-PSilQ NPs or PpIX at the same concentrations but were maintained in the dark for the entire duration of the experiment. To determine the phototoxicity of the PDT treatment, the cells were washed once with DPBS, and 100 µL media was added along with 20 µL of CellTiter 96 solution to each well. The cells were incubated for 2 h at 37 °C in 5% CO_2 atmosphere. Cell viability (%) was analyzed and calculated as described above. The IC_{50} values are determined using GraphPad Prism (v8.3.0 for Windows, La Jolla, CA, USA), fitting the viability data to a nonlinear regression.

3.2.9. Evaluation of NADPH/NADP+ Kinetics

A375 cells were seeded at a density of 5×10^4 cells/well in complete DMEM in six-well plates. After 24 h of incubation at 37 °C in 5% CO_2 atmosphere, PpIX-PSilQ NPs, or PpIX (10, 30, or 50 µM of PpIX) were added to the cells in fresh media. Followed by 48 h of incubation, cell media was removed, and cells were washed once with DPBS and irradiated with red light (630 nm, 24.5 mW/cm^2) for 20 min. Fresh media was replenished, and cells were incubated for additional 2 h. Then, cells were washed once with DPBS and harvested. Collected cells were centrifuged for 5

min at 4 °C at 13,000× *g*. Supernatants were collected by transferring to new tubes. Non-irradiated samples and untreated cells were employed as controls. Samples were prepared as per assay protocol (Glutathione Peroxidase Activity Assay Kit, Fluorometric, Abcam ab21992) in a 96-well solid black plate in triplicate per sample. Fluorescence intensity (Ex/Em = 420/480) was monitored using a TECAN SPARK® multimode microplate reader in kinetic mode for 60 min. Reaction rates were determined using GraphPad Prism (v8.3.0 for Windows, La Jolla, CA, USA), fitting the kinetic data to a non-linear curve (second order polynomial).

3.2.10. Measurement of Intracellular Lipid Peroxides

A375 cells were seeded in six-well plates at a density of 5×10^4 cells/well in 2 mL of complete DMEM and incubated at 37 °C in 5% CO_2 atmosphere. After 24 h, PpIX-PSilQ NPs or PpIX (50 µM of PpIX) were added to the cells in fresh media. Followed by 48 h of incubation, cell media was removed, and cells were washed once with DPBS. Cell-permeable lipid peroxide probe C-11 BODIPY (10 µM) was added to the cells in serum free media, and cells were incubated for 30 min at 37 °C and 5% CO_2. After removing the media, the cells were washed once with DPBS and irradiated (630 nm, 24.5 mW/cm^2) for 20 min. Cells were incubated for 6 h post irradiation and harvested using trypsin. The fluorescence was analyzed using a BD LSRFortessa flow cytometer. A shift from ~590 nm to ~510 nm was expected from the oxidation of the polyunsaturated butadienyl portion of the dye. Control experiments of cells untreated, PpIX-PSilQ NPs, and PpIX in the absence of light were also carried out.

The extent of lipid peroxidation was further confirmed using confocal microscopy. A375 cells were seeded in six-well plates at a density of 5×10^4 cells/well in complete DMEM at 37 °C in 5% CO_2 atmosphere. After 24 h of incubation, cell media was removed, and 50 µg/mL of PpIX-

PSilQ NPs were added to the wells in fresh media. Cell were incubated for additional 24 h, cell media was removed, and cells were washed twice with DPBS. Cell-permeable lipid peroxide probe C-11 BODIPY (10 µM) was added to the cells in serum free media and incubated for 30 min at 37 °C and 5% CO_2. After removal of the cell media, the cells were washed once with DPBS and irradiated (630 nm, 24.5 mW/cm^2) for 20 min. Then, 6 h after irradiation, coverslips were washed with DPBS and then mounted on to glass slides using adhesive spacers. Untreated cells were used as the baseline, while cells treated with PpIX-PSilQ NPs and PpIX in the absence of light were imaged as control experiments. Images were acquired using Olympus FluoView 1000 confocal fluorescence microscope at 40 × magnification

3.2.11. Statistics

All experimental results in this study are reported as mean ± standard deviation (SD) unless mentioned otherwise. The hydrodynamic size and ζ-potential were carried out in triplicate. The amount of PpIX loaded to the PSilQ nanoparticles was analyzed in triplicate using different batches. Cellular uptake, Annexin V apoptosis/necrosis, ROS detection by DCFH-DA, and C-11 BODIPY oxidation using flow cytometry were measured with a minimum of 10,000 gated cells and quantified in triplicates. The statistical analysis for all experiments was performed with two-way ANOVA using Tukey's multiple comparison test. All the statistical analysis was performed using GraphPad prism (v8.2.0) with a p-value <0.05 considered to be statistically significant. For the cell viability studies, GraphPad Prism was used to calculate the IC_{50} values (n = 6).

3.3. Results and discussion

3.3.1. Synthesis and Characterization of PpIX-PSilQ NPs

The synthesis of the PpIX silane precursor was carried out through a multi-step reaction pathway already reported by our group with slight modifications (Scheme S1) *[166, 233]*. Compounds 2–4 were characterized using spectroscopic techniques as depicted in the Supporting Information.

The structural properties of the PpIX-PSilQ nanoparticles were characterized using DLS, ζ-potential, and SEM. The hydrodynamic diameter of nanoparticles was determined as 262.6 ± 20.0 nm in PBS (*Figure 18*). The ζ-potential measurements show a negative surface charge (−35.5 ± 4.0 mV) on the surface of PpIX-PSilQ NPs (Table S1). SEM images of PpIX-PSilQ NPs depict the nanoparticles as spherical in morphology with a size of 41.7 ± 4.9 nm (n = 10) (*Figure 18* and Figure 24). The loading capacity of PpIX in the nanoparticles was characterized using TGA, and the amount of PpIX was determined as 24.0 ± 2.0% wt (*Figure 18* and Table 2), which was confirmed by UV-vis spectroscopy, 20.2 ± 3.6% wt (Figure 25). The UV-vis absorption spectrum corroborates the presence of PpIX in PpIX-PSilQ NPs (*Figure 18*). The characteristic S-band for porphyrins was clearly observed at 404 nm. The colloidal and chemical stability of the nanoparticles was characterized using DLS and UV-vis spectroscopy, respectively. DLS data show that the hydrodynamic diameter and polydispersity index (PdI) of the PpIX-PSilQ NPs in complete cell media were fairly stable during 24 h (Figure 24). The leak of PpIX molecules from PpIX-PSilQ NPs was studied in the presence and absence of a reducing agent (dithiothreitol = DTT) for 192 h. Minimal leakage (<10%) was determined during that time (Figure 24).

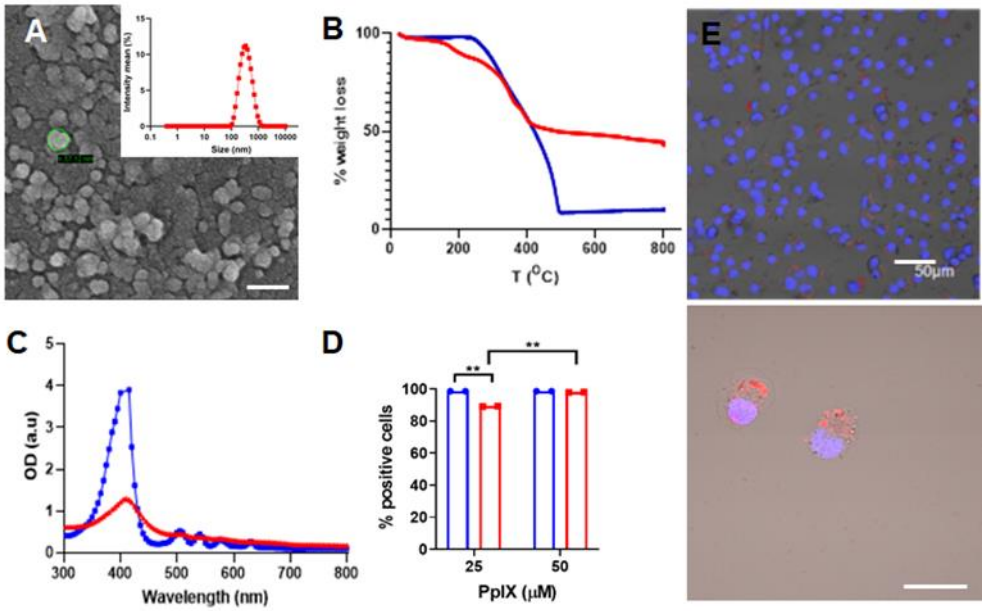

Figure 18. Characterization of PpIX-PSilQ NPs. (A) DLS and SEM image of PpIX-PSilQ NPs. Scale bar = 100 nm. (B) TGA plot for PpIX (blue) and PpIX-PSilQ NPs (red). (C) UV-vis spectrum of PpIX (blue) and PpIX-PSilQ NPs (red). (D) Flow cytometry data of PpIX-PSilQ nanoparticles (red) and free PpIX (blue) at different concentrations (25 and 50 µM PpIX) in A375 cells after 24 h of incubation. Statistics: two-way ANOVA using Tukey's multiple comparison test; ** $p \leq 0.01$. (E) Confocal microscopy images of A375 cells after 24 h incubation with PpIX-PSilQ NPs (25 µM PpIX). Image(s) show merged fluorescent channels of Hoechst-33342 nuclear stain dye (blue), PpIX fluorescence (red), and brightfield. Scale bars = 50 µm and 20 µm.

3.3.2. In Vitro PDT Performance of PpIX-PSilQ NPs

The cellular internalization of PpIX-PSilQ nanoparticles was evaluated by flow cytometry and confocal microscopy using A375 cells. Flow cytometry data (*Figure 18*) for PpIX-PSilQ NPs at two different concentrations of PpIX, 25 and 50 µM, showed 89.2 ± 0.1% and 98.5 ± 0.2% of positive cells, respectively. In the case of free PpIX, flow cytometry results showed over 99.0% of positive cells at the tested doses of 25 µM and 50 µM. Confocal micrographs obtained for PpIX-PSilQ nanoparticles at 25 µM confirmed the presence of red fluorescence spots inside A375 cells (*Figure 18*).

The phototoxicity of PpIX-PSilQ NPs was evaluated in A375 cells in the presence of red light (630 nm; 30 J/cm^2) for 20 min using the MTS assay. PpIX-PSilQ NPs showed dose-dependent phototoxicity, as seen in Figure 26. The calculated IC_{50} value for nanoparticles was 81.2 µM. The cytotoxicity in the absence of light (dark cytotoxicity) of the nanoparticles was also tested. As seen in Figure 26, PpIX-PSilQ NPs showed no cytotoxicity even at equivalent concentrations of PpIX as high as 250 µM. The phototoxicity of PpIX also depicted a dose-dependent response similar to PpIX-PSilQ NPs. The calculated IC_{50} for PpIX in the presence of red light was 9.4 µM. Dark cytotoxicity evaluation of free PpIX showed a 20–25% decline in cell viability in the concentration range of 100–250 µM.

The production of some of ROS, including hydrogen peroxide, hydroxyl, and peroxyl radicals associated with PDT, were measured in vitro using a fluorescent ROS probe, DCFH-DA *[240, 241]*. Upon diffusion into cells, DCFH-DA is deacetylated by cellular esterases to a non-fluorescent compound, which is later oxidized by ROS into fluorescent 2′,7′- dichlorofluorescein (DCF). A375 cells were treated with PpIX-PSilQ nanoparticles at 50 and 100 µM equivalent of PpIX. Quantification by flow cytometry shows 9.0 ± 2.9% and 18.9 ± 3.3% of DCF positive cells post irradiation for those concentrations, respectively (*Figure 19*). In the case of PpIX, 3.2 ± 0.9% and 45.9 ± 6.6% of DCF positive cells were measured post irradiation for 10 and 50 µM, respectively (*Figure 19*). For both PpIX-PSilQ NPs and PpIX, negligible production of ROS was detected in the absence of light irradiation. Confocal microscopy was used to visually confirm the

generation of ROS. As seen in the confocal micrographs (Figure 27), both PpIX-PSilQ nanoparticles and PpIX produce ROS inside the cells upon irradiation.

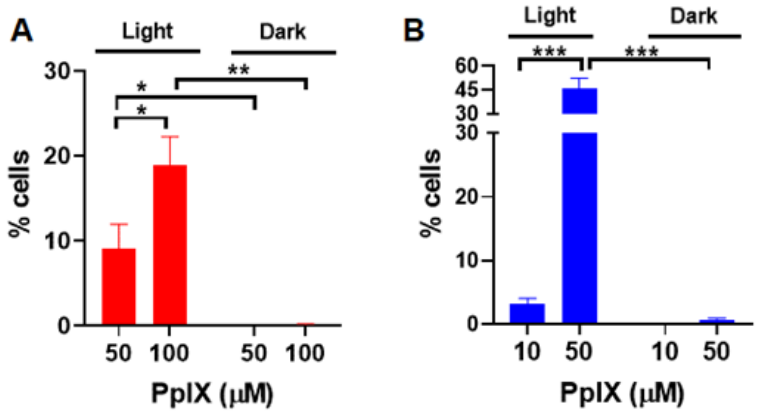

Figure 19. Reactive oxygen species generated by PpIX-PSilQ NPs. Quantification of ROS positive cells by flow cytometry of (A) PpIX-PSilQ nanoparticles (50 and 100 μM equivalent of PpIX) and (B) PpIX (10 and 50 μM) in the presence or absence of light. Data are represented as mean ± SD. Statistics: two-way ANOVA using Tukey's multiple comparison test: *** $p \leq 0.001$, ** $p \leq 0.01$, * $p \leq 0.05$, and ns: $p > 0.05$.

3.3.3. Apoptosis and Necrosis induced by PpIX-PSilQ Nanoparticles

The generation of apoptosis and/or necrosis promoted by PDT using PpIX-PSilQ NPs was analyzed using flow cytometry in the presence of the SYTOX Blue dead-cell nuclear stain assay and Annexin V Apoptosis Detection Kit. SYTOX Blue dye penetrates compromised plasma membrane, staining nucleic acids inside the cells. The Annexin V assay contains a FITC-labeled antibody that binds to phosphatidylserine residues expressed on the plasma membrane of apoptotic cells. Two different concentrations of nanoparticles were evaluated in this experiment: 50 and 100 μM, based on the amount of PpIX. These concentrations were selected with the purpose of the photoactivity associated to the nanoparticles, which triggers a measurable response for the cell death mechanisms. Cells treated with nanoparticles in the presence of light showed 5.8 ± 1.7% and 24.2 ± 1.7% of Annexin-V-positive cells for 50 and 100 μM, respectively (Figure 20). Dark controls for nanoparticles were used as negative controls, showing only 0.7 ± 0.6% and 4.7 ± 1.2%

of Annexin-V-positive cells for the same concentrations (Figure 28). A similar analysis was performed for PpIX at concentrations of 10 and 50 μM. As depicted in Figure 28, cells treated with 50 μM of PpIX after light irradiation exhibited 62.3 ± 17.6% of Annexin-V-positive cells. PpIX at 10 μM did not show a significant production of apoptotic cells. Dark controls for PpIX show 3.7 ± 1.2% of Annexin-V-positive cells for 50 μM (Figure 28). Cells treated with nanoparticles showed 2.6 ± 0.0% and 7.4 ± 1.8% necrotic cells for treatment concentrations 50 and 100 μM in the presence of light (Figure 20). Nanoparticle treatment led to less than 0.1% necrotic cell death for 50 and 100 μM in the absence of light (Figure 28). Necrosis was observed in 3.5 ± 2.3% and 4.9 ± 0.4% of the analyzed population of cells treated with 10 and 50 μM of free PpIX (Figure 20) in the presence of light. In the case of dark controls, free PpIX treatment caused necrosis in 3.1 ± 1.0% and 3.9 ± 0.2% of cells treated with 10 and 50 μM, respectively (Figure 28).

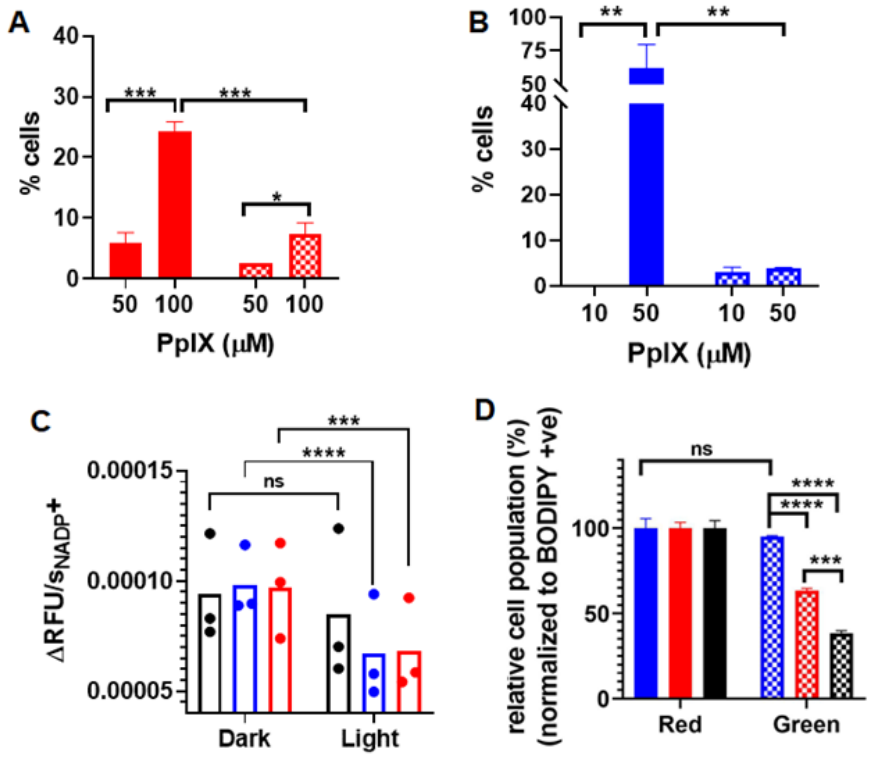

Figure 20. (**A**) Apoptotic (red solid bars) and necrotic (red checkered bars) cells after PDT treatment with PpIX-PSilQ NPs (50 and 100 μM equivalent of PpIX). (**B**) Apoptotic (blue solid bars) and necrotic (blue checkered bars) cells after PDT treatment with PpIX (10 and 50 μM). (**C**) Reaction rate values of $NADP^+$ generation for control (black), PpIX-PSilQ NPs (50 μM PpIX eq.) (red), and PpIX (50 μM) (blue). (**D**) Quantification of lipid peroxidation using confocal microscopy in A375 cells treated with control (black), PpIX-PSilQ NPs (50 μM PpIX eq.) (red), and PpIX (50 μM) (blue) in the red (solid bars) and green (dashed bars) channels. Data are represented as mean ± SD. Statistics: two-way ANOVA using Tukey's multiple comparison test: **** $p \leq 0.0001$, *** $p \leq 0.001$, ** $p \leq 0.01$, * $p \leq 0.05$, and ns: $p > 0.05$.

3.3.4. Inactivation of Glutathione Peroxidase Triggered by PpIX-PSilQ Nanoparticles

We assessed the effect of PpIX-PSilQ nanoparticles using A375 cells on the activity of the enzyme family glutathione peroxidase (GpX) indirectly through the NADPH oxidation reaction. The assay involves the oxidation of external glutathione (GSH) to glutathione disulfide (GSSG) catalyzed by

GpX in collected cell lysates. The GSSG generated in the previous step is reduced to GSH by externally supplied glutathione reductase (GR) and nicotinamide adenine dinucleotide phosphate (NADPH), affording $NADP^+$ as by-product (Figure 29). The kinetics of formation of $NADP^+$, monitored by the fluorescence of a $NADP^+$-specific probe, is an indirect approach to measure the catalytic activity of GpX *[242]*. The kinetic profiles of $NADP^+$ for cells incubated with PpIX-PSilQ nanoparticles or PpIX in the presence of light showed a clear reduction in the formation of $NADP^+$ compared with control groups (Figure 29). To confirm these results, the rates of formation of $NADP^+$ were calculated (Figure 20). The reaction rate values of cells treated with PpIX-PSilQ nanoparticles or PpIX indicate a significant decline in the generation of $NADP^+$, which is as an indirect consequence in the reduction of the GpX activity.

3.3.5. Lipid ROS Generation Detected by a Lipid Peroxidation Sensor

The beginning of lipid peroxidation in cells is routinely characterized by measuring the oxidation of a lipophilic fluorescent probe, BODIPY™ 581/591 C11. The probe monitors the formation of oxygen-centered lipid radicals in phospholipid membranes of cells by eliciting an oxidation-induced shift in fluorescence emission peak from 590 nm (red) to 510 nm (green) *[243]*. We determined the impact on lipid peroxidation after treatment of A375 cells with PpIX-PSilQ nanoparticles by flow cytometry and confocal microscopy. The flow cytometry data in Figure 20 shows 24.9 ± 1.5% and 56.8 ± 1.2% increase in positive cells for PpIX-PSilQ nanoparticles and PpIX after irradiation as compared with control (two-way ANOVA, $p \leq 0.001$). Control experiments with PpIX-PSilQ nanoparticles and PpIX in the absence of light showed less than 1% of positive cells (Figure 30). The lipid peroxidation in A375 cells associated with the PpIX-PSilQ nanoparticles after PDT treatment was further corroborated by confocal microscopy. Figure 21 shows the confocal micrographs associated with the BODIPY C11 dye (red channel), the oxidized

version of the dye (green channel), and merged versions together with the brightfield. The red channel shows the presence of the BODIPY C11 dye in the membranes (Figure 21). In the case of the samples that were irradiated, an enhancement in green fluorescence is observed for both PpIX-PSilQ NPs and PpIX (Figure 21) as compared with control experiments in the absence of light (Figure 31). Merged images (Figure 21) confirmed the overlap of the BODIPY C11 dye and its oxidized version after light irradiation.

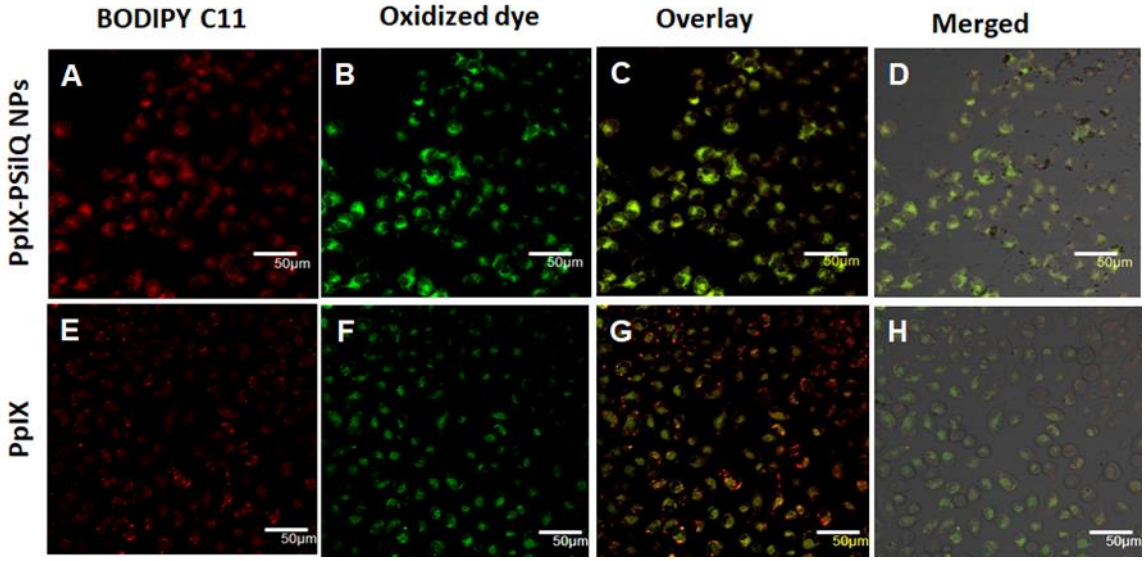

Figure 21. Lipid peroxidation detected by BODIPY™ 581/591 C-11 sensor. Confocal micrographs of A375 cells inoculated with (**A**–**D**) PpIX-PSilQ nanoparticles or (**E**–**H**) PpIX after light irradiation. The red channel depicts the presence of BODIPY 581/591 C-11 (**A**,**E**). The green channel shows the fluorescence corresponding to the oxidized version of BODIPY 581/591 C-11 (**B**,**F**). Merged image of the red and green channels (**C**,**G**) with the brightfield image (**D**,**H**). Scale bar = 50 µm.

3.3.6. Inhibition of Ferroptosis Using Ferrostatin-1

To determine the impact of ferroptosis on the PDT treatment of A375 cells using PpIX-PSilQ nanoparticles, we evaluated the phototoxicity of the nanoparticles in the presence of a lipophilic antioxidant (Ferrostatin-1) (*Figure 22*). Ferrostatin-1 decreased the phototoxic effect of PpIX-PSilQ NPs on A375 cells by 36% as indicated by increase in the IC_{50} to 110.9 µM from 81.2 µM

in the presence and absence of Ferrostatin-1, respectively. In the case of PpIX, the influence of Ferrostatin-1 shows an important reduction of 63% on the PDT effect against A375 cells with IC_{50} values of 15.4 µM and 9.4 µM in the presence and absence of Ferrostatin-1, respectively. Control experiments in the absence of light showed no cytotoxic effect associated with the presence of Ferrostatin-1 (*Figure 32*).

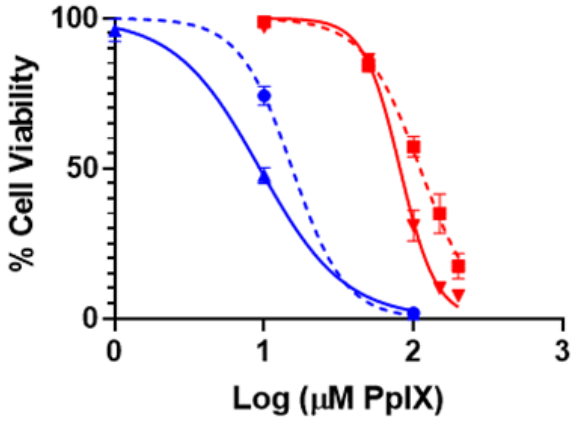

Figure 22. Phototoxicity of PpIX-PSilQ nanoparticles. PpIX-PSilQ nanoparticles (red) and PpIX (blue) treated A375 cells in the absence (solid) or presence (dashed) of Ferrostatin-1 (2 µM). Irradiation with red light (630 nm; 24.5 mW cm−2) for 20 min (n = 6).

3.3.7. Discussion

Photodynamic therapy triggers different type of cell death mechanisms, with the most common being apoptosis, necrosis, and autophagy. Apoptosis is an endogenous mechanism involved with complicated apoptosis signaling cascade and can be compromised by augmented antiapoptotic signaling or loss of proapoptotic mechanisms [244]. Therefore, drug-resistance is induced in many chemotherapy-based cancer treatments. Ferroptosis, as an alternative approach of inducing cell death by lipid peroxidation, has attracted much attention to overcome some of the challenges associated to drug-resistant cancers [245]. Recently, ferroptosis has also been associated with PDT [98]. Our group has focused on the development of PSilQ nanoparticles as a photosensitizer-

delivery platform for PDT [166, 230-233, 246]. We have already demonstrated that PSilQ nanoparticles carrying PpIX as a photosensitizer induce phototoxicity through apoptotic and necrotic cell death mechanisms [233]. However, the possibility of these nanoparticles also triggering ferroptosis has not been investigated. In this study, we synthesized PpIX-PSilQ nanoparticles without stimuli-responsive features to warrant permanent encapsulation of PpIX molecules in the nanoparticle. Based on an already established synthetic protocol in our group, we synthesized and characterized a PpIX silane derivative that is used for the fabrication of the PpIX-PSilQ nanoparticles in this work [166, 232]. A three-component microemulsion method was used for the fabrication of the PpIX-PSilQ nanoparticles. The nanomaterial is spherical with a diameter of 41.7 ± 4.9 nm, a hydrodynamic diameter of 262.6 ± 20.0 nm, and ζ-potential of -35.5 ± 4.0 mV. The hydrodynamic diameter of the material is constant over a period of 24 h, and minimal degradation was observed during 192 h as an indication of its colloidal and chemical stability. As reported previously, PSilQ nanomaterials are distinguished for reaching a high loading capacity of the therapeutic agent [166, 247-249]; in this case, the loading of PpIX to PSilQ nanoparticles was determined to be 24.0 ± 4.0%wt.

We evaluated the in-vitro properties of the PpIX-PSilQ nanoparticles in a human melanoma cell line, A375 cells. Several studies have showed promising results supporting the efficacy of PDT to treat melanoma either as primary or adjuvant therapy at different stages of the disease [25, 250]. Flow cytometry and confocal microscopy showed that A375 cells were able to internalize the nanoparticles in high amounts despite the negative charge on their surface. We previously reported that the cell internalization of PSilQ nanoparticles is usually carried out through an endocytosis pathway [166, 233].

The PDT performance in A375 showed the typical dose response associated to the PpIX-PSilQ nanoparticles. In comparison with the parent porphyrin PpIX, the phototoxicity of the nanoparticles is reduced about nine times, IC_{50} for PpIX = 9.4 µM vs PpIX-PSilQ NPs = 81.2 µM. This difference can be explained by the self-quenching effect produced through encapsulating of photosensitizers in the nanoparticles, which directly impacts the generation of $^1O_2$ [230, 231]. Nevertheless, our group showed that by rendering stimuli-responsive degradability to the nanoparticles, the PDT capability can be restored, making this a promising approach to avoid unwanted side effects due to phototoxicity of photosensitizers in healthy tissue [166, 233].

Cell death related to PDT is triggered by the production of reactive oxygen species inside the cells. First, we measured the generation of ROS by PpIX-PSilQ nanoparticles in vitro using DCFH-DA as ROS probe with flow cytometry. The quantification of positive cells associated with ROS demonstrated that nanoparticles in the presence of light generated ROS in a concentration-dependent manner. A similar trend was shown for PpIX (*Figure 19*). Confocal microscopy was used to further demonstrate the ability of PpIX-PSilQ nanoparticles for ROS production. DCFH-DA is a ROS probe specific for detecting hydrogen peroxide, hydroxyl, and peroxyl radicals in vitro [240, 241]. The confocal micrographs corroborate the formation of ROS by PpIX-PSilQ NPs after activation with light.

Apoptosis is the most common cell death mechanism associated with PDT. The impact of light-activated photosensitizers on mitochondria is reported as a major factor controlling the induction of apoptosis. The caspase-dependent apoptotic cascade involving mitochondrial membrane depolarization and subsequent loss of cytochrome *c* (*cyt c*) has been well characterized with respect to PDT [251]. In cancer cells with abnormally high levels of *Bcl-2*, photodamage by cross-linking or cleavage may limit the effectiveness of this important anti-apoptotic control. In many cases,

Bcl2 has been reported as an important molecular target of PDT that promotes apoptosis in treated cells [252, 253]. We previously reported enhancement in apoptosis resulting from silencing of *Bcl-2* gene in A375 cells [254]. In our previous work, we demonstrated that PpIX-based PSilQ nanoparticles use apoptosis as one of the main cell death mechanisms to eliminate triple-negative breast cancer cells [233]. Herein, we used the Annexin V apoptosis assay to confirm that apoptosis also plays an important role in the PDT of A375 cells using PpIX-PSilQ nanoparticles or the parent porphyrin PpIX (Figure 20). We also observed that a higher proportion of necrotic cells were obtained for the PpIX-PSilQ nanoparticles. Nanoparticles, which are usually endocytosed and trafficked through the endolysosomal pathway, are highly localized in lysosomes [255]. It has been shown that the excess of ROS generated by PSs inside the lysosomal compartment prompt lysosomal membrane permeabilization (LMP) [256]. Excessive LMP often causes necrotic cell death by extreme cytosolic acidification [257]. Control experiments in the dark show a minimal number of apoptotic or necrotic cells associated with nanoparticles.

Ferroptosis is described as a regulated cell death mechanism driven by lipid peroxidation and the suppression of the GpX enzymatic activity, often observed as a consequence of excess intracellular ROS produced by Fenton reactions mediated by iron [98, 236, 237]. In this project, PDT affords lipid peroxidation by two different mechanisms: the direct reaction of $^1O_2$ or the reaction of hydroxyl radicals with lipid membrane [238]. Both alternatives afford the accumulation of lipid hydroperoxides [258, 259]. In addition, PDT can induce direct photo-oxidative inactivation of GpX enzymes by $^1O_2$ and GSH depletion, which results in increased intracellular peroxides that are responsible for cellular damage through ferroptosis [242]. Therefore, PDT can trigger ferroptosis by increasing the amount of lipid peroxides and inactivating GpX enzymes. We investigated the effect of PpIX-PSilQ nanoparticles in both the formation of lipid peroxides and

inactivation of GpX enzymes. The kinetic profile for the generation of $NADP^+$, which is an indirect approach to measure the activity of GpX enzymes, clearly demonstrated a reduction in the production of $NADP^+$ when A375 cells were treated with PpIX-PSilQ nanoparticles in the presence of light irradiation. A significant reduction of the reaction rate values for the generation of $NADP^+$ confirms the impact of PpIX-PSilQ nanoparticles on the activity of GpX enzymes (Figure 20). Similar performance was observed for PpIX molecules. The photo-oxidative mechanism for the inactivation of GpX enzymes by photosensitizers through type II reaction was reported using rose Bengal [260]. An irreversible oxidation of selenocysteine centers in GpX to dehydroalanine (DHA), and consequent loss of GpX activity due to $^1O_2$ was detected in the lysates of J774A.1 cells photo-treated with this photosensitizer. Overproduction of $^1O_2$ diminishes the activity of GpX enzymes most likely by modification of selenocysteine residues [261].

We also studied the formation of lipid peroxides using a lipid peroxidation sensor through flow cytometry and confocal microscopy. Similar to PpIX molecules, PpIX-PSilQ nanoparticles after light irradiation enhanced the generation of lipid peroxides compared with only light treatment (two-way ANOVA, $p \leq 0.001$) (Figure 20). Overall, our results show that by encapsulating PpIX molecules in the PSilQ platform, comparable trends were observed with PpIX on the inactivation of GpX enzymes and production of lipid peroxides as a clear indication that PpIX-PSilQ nanoparticles lead to ferroptosis as one of the mechanisms of cell death.

To further confirm that the ferroptosis mechanism is involved in the PDT performance of PpIX-PSilQ nanoparticles, we tested the phototoxicity of the material in the presence of ferrostatin-1, a selective and potent inhibitor of ferroptosis (*Figure 22*). This molecule is a radical-trapping antioxidant agent that traps peroxyl radicals in membrane lipids, which are the primary species to trigger ferroptosis [262]. The phototoxicity data showed that the presence of ferrostatin-1 reduced

the PDT effect of PpIX-PSilQ nanoparticles and PpIX molecules by 36% and 63%, respectively. Our results described above show that the PDT effect of PpIX-PSilQ NPs reduced GpX activity, contributing to the failure of peroxyl radical-scavenging capacity and increasing the lipid peroxidation levels of treated cells. However, the addition of the phospholipid radical-trapping agent ferrostatin-1 reduced the phototoxicity exerted by PpIX-PSilQ NPs. This significant impact of ferrostatin-1 in the PDT performance of both PpIX-PSilQ nanoparticles and PpIX gives a clear indication that ferroptosis is an important cell death mechanism in their PDT performance [98]. Overall, these results are convincing arguments to support the hypothesis that ferroptosis is one of the main cell death mechanisms triggered by PSilQ nanoparticle-mediated photodynamic therapy.

3.4. Conclusion

We designed and fabricated PpIX-PSilQ nanoparticles with minimal leaking of the photosensitizer to study the cell death pathways associated with their PDT effect in A375 cells. PpIX-PSilQ nanoparticles followed similar cell death pathways as the parent PpIX photosensitizer. Apoptosis is an important pathway for PpIX and PpIX-PSilQ nanoparticles as well. PpIX-PSilQ nanoparticles showed higher necrotic cells than PpIX, most likely related to lysosomal membrane permeabilization, which is directly associated with the intracellular trafficking of the nanoparticles. We demonstrated, by analyzing the level of lipid peroxides and inactivation of GpX enzymes, that PpIX-PSilQ nanoparticles also follow ferroptosis as an important pathway to kill A375 cancer cells. This study provides a deeper understanding of the cell death pathways that account for the PDT effect of photosensitizer loaded PSilQ nanoparticles. We envision that this investigation provides relevant results to develop promising light-activated nanoparticles that depend on ferroptosis for the treatment of apoptosis-resistant cancer cells.

3.5. Appendix- Light-Activated Protoporphyrin IX-Based Polysilsesquioxane Nanoparticles Induce Ferroptosis in Melanoma Cells

Materials

Protoporphyrin IX (PpIX), dioctyl sodium sulfosuccinate (Aerosol OT or AOT), 2',7'-dichlorodihydrofluorescein diacetate (DCFH-DA), BODIPY^{TM} 581/591 C-11 (Lipid peroxidation sensor) and SYTOX^{TM} Blue dead cell stain and Glutamax were obtained from Thermo Fischer Scientific (Waltham, Massachusetts, USA). 1- ethyl-3-(3-dimethylaminopropyl) carbodiimide (EDC) was purchased from Oakwood Chemical (Columbia, South Carolina, USA). N-butanol, dithiothreitol (DTT), serine, 3-(Triethoxysilyl)propyl isocyanate (TESPIC), Ferrostatin-1, sterile-filtered DMSO and the rest of the chemicals used in this work were obtained from Sigma-Aldrich (St. Louis, Missouri, USA). Chemicals and solvents were used without any further purification unless specified otherwise. Roswell Park Memorial Institute (RPMI 1640), Dulbecco Modified Eagle Medium (DMEM), penicillin-streptomycin (pen-strep), phosphate buffer saline (PBS, 1X), and trypsin were purchased from Corning (Corning, New York, USA). CellTiter 96® AQueous Assay was obtained from Promega (Madison, WI, USA). Non-essential amino acids (NEAA) was purchased from Quality biologicals (Gaithersburg, Maryland, USA). Fetal bovine serum (FBS) was purchased from Atlanta Biologicals (Atlanta, Georgia, USA). Hoechst 33342 dye was purchased from Life Technologies (Waltham, Massachusetts, USA). BD Pharmingen™ Annexin V-FITC apoptosis detection kit was purchased from BD Biosciences (San Jose, California, USA). Glutathione peroxidase activity assay kit (Fluorometric) was purchased from Abcam (Waltham, Massachusetts, USA).

Methods

A Raith 150 Field Emission Scanning Electron Microscope (SEM) (Raith America Inc., New York, NY, USA) was utilized to measure the particle size and shape of the materials.

Nanoparticle samples were suspended in methanol in preparation for the SEM. Dynamic light scattering (DLS) and ζ-potential measurements were carried out using a Malvern Instrument Zetasizer Nano (red laser 633 nm) (Malvern Instrument Ltd., Malvern, UK). The amount of PpIX loaded into the PSilQ NPs was quantified by thermogravimetric analysis (Mettler-Toledo AG Analytical, Schwersenbach, Switzerland). The thermal degradation profiles were obtained for a heating rate of 1 °C/min between 25 and 800 °C followed by a 60 min hold at 800 °C. Biotable power source with RGB LED array (MM Optics, University of São Paulo, Brazil) emitting at 630 nm (24.5 mW/cm²) was used for all *in vitro* PDT experiments. A microplate reader (TECAN Spark) was used for fluorescence intensity measurement in kinetic mode for $NADP^+$ (San Jose, California, USA). A Multiskan FC plate reader by Fisher Scientific plate reader was used for the cell viability analysis (Waltham, Massachusetts, USA). A BD LSRFortessa™ cell analyzer was used for the fluorescence-activated cell sorting (FACS) experiments (Indianapolis, Indiana, USA). An Olympus Fluoview FV 1000 confocal laser scanning microscope (CLSM) was used for the confocal experiments (Center Valley, Pennsylvania, USA).

Synthesis of PpIX silane derivative (4)

The synthesis of the PpIX silane derivative used as monomer for the fabrication of PpIX-PSilQ nanoparticles was performed in a three-step reaction pathway (Scheme S1). First, the synthesis of protoporphyrin IX succinimide ester (PpIX-SE) (**2**) was carried out by placing 0.889 mmol (500 mg) of protoporphyrin IX (PpIX) (**1**) in a round bottom flask containing 20 mL of dimethyl sulfoxide (DMSO) and 70 mL of dichloromethane (DCM). To this solution, 2.226 mmol (272 mg) of 4-dimethyl amino pyridine was added along with a solution of 5.320 mmol (1.02 g) of 1-ethyl-3-(3-dimethylaminopropyl) carbodiimide (EDC) hydrochloride in 20 mL of DMSO. The

flask was then placed in an ice bath and stirred for 10 min. To this mixture, 5.326 mmol (613 mg) of N-hydroxysuccinimide (NHS) was added to the flask and was kept in an ice bath for 3 h. A diluted ethanolic solution in water (100 mL, EtOH:H_2O/75:25% vol./vol.) was added to the flask to afford precipitation of the product. PpIX-SE (**2**) was then collected through gravity filtration and washed with ethanol before being dried in a lyophilizer. Yield: 506 mg (76 %wt.); ^{1}H NMR (DMSO-d_6, ppm): δ 2.71 (m, 8H), 3.15 (t, 4H, J = 7.3 Hz), 3.55 (s, 3H), 3.56 (s, 3H), 3.61 (s, 3H), 3.63 (s, 3H), 4.28 (t, 4H, J = 7.3 Hz), 6.17 (d, 2H, J = 11.7 Hz), 6.38 (d, 2H, J = 17.9 Hz), 8.36 dd, 1H, J = 17.2 Hz, 11.7 Hz), 8.44 (dd, 1H, J = 17.2 Hz, 11.7 Hz), 10.05 (s, 1H), 10.09 (s, 1H), 10.10 (s, 1H), 10.12 (s, 1H). FT-IR (cm^{-1}): 3503 (N-H), 2915 (C-H), 1808 (C=O), 1778 (C=O), 1732 (C=O), 1627 (CN); MALDI-MS (m/z): Calculated: $[M]a^+$ = 756.30; Observed: $[M]^+$ = 756.31. UV-Vis (DMF, nm): 404 (S-band); 623, 576, 542, 506 (Q-bands). Molar extinction coefficient (λ = 404 nm; DMF; mol L^{-1} cm^{-1}): 195,800. As the second step, PpIX-serine (**3**) was afforded by dissolving 0.46 mmol (350 mg) of PpIX-SE (2) in 25 mL of DMSO. To this mixture, an aqueous solution of serine (1.5 mmol, 150 mg in 3.0 mL of water) was added by the addition of diisopropylethylamine (DIPEA) (2.0 mmol, 350 μL). The final solution was heated and stirred at 120 °C for 72 h. A diluted acidic ethanolic-based solution (250 mL of H_2O:Ethanol; 20:80 %vol./vol.; 200 μL of concentrated HCl) was added to the flask to precipitate out the product. The precipitate is collected by gravity filtration and washed with water before being dried in a lyophilizer. Yield: 506 mg (49 %wt.); ^{1}H NMR (DMSO-d_6, ppm): 3.06 (t, 4H, J = 7.7 Hz), 3.54 (s, 3H), 3.56 (s, 3H), 3.62 (s, 3H), 3.64 (s, 3H), 3.92 (d, 4H, J = 5.1 Hz), 4.34 (t, 4H, J = 7.7 Hz), 4.66 (t, 2H, J = 5.1 Hz), 6.14 (d, 2H, J = 11.1 Hz), 6.33 (d, 2H, J = 17.4 Hz), 8.39 (dd, 1H, J = 17.4 Hz, 11.1 Hz), 8.47 (dd, 1H, J = 17.4 Hz, 11.1 Hz), 10.04 (s, 1H), 10.12 (s, 1H), 10.18 (s, 1H), 10.21 (s, 1H). IR (cm^{-1}): 3306 (N-H), 2920 (C-H), 1710 (C=O),

1640 (C-N). UV-Vis (DMF, nm): 408 (S-band); 628, 575, 540, 506 (Q-bands). Molar extinction coefficient (λ = 408 nm; DMF; mol L^{-1} cm^{-1}): 75,800. To produce the PpIX silane precursor (**4**), PpIX-serine (**3**) (0.13 mmol, 100 mg) was placed into a round bottom flask under N_2 atmosphere followed by the addition of dry DMF (10 mL). To this solution, triethylamine (0.57 mmol, 161.8 μL) was slowly added until compound (**3**) was fully dissolved. Later, the whole solution was placed in an ice bath followed by the addition of triethoxysilyl propyl isocyanate (TESPIC) (0.27 mmol, 134.7 μL). The final solution was left for 3 h in the ice bath, let warmed up to room temperature and stirred for an additional 15 h. To obtain the final product, 80 mL of acidic aqueous solution (200 μL of conc. HCl) was added to precipitate out compound **4** and collected it by gravity filtration. The PpIX silane derivative is dried in a lyophilizer. ^{1}H NMR (DMSO-d_6, ppm): 0.24 (t, 4H, J = 8.1 Hz), 0.90 (t, 18H, J = 6.9 Hz), 1.25 (q, 4H, J = 8.1 Hz), 3.00 (t, 4H, J = 7.7 Hz), 3.06 (t, 4H, J = 8.1 Hz), 3.43 (q, 12H, J = 6.9 Hz), 3.56 (s, 3H), 3.58 (s, 3H), 3.67 (s, 3H), 3.70 (s, 3H), 3.92 (d, 4H, J = 5.1 Hz), 4.34 (t, 4H, J = 7.7 Hz), 4.66 (t, 2H, J = 5.1 Hz), 6.12 (d, 2H, J = 11.3 Hz), 6.31 (d, 2H, J = 17.9 Hz), 8.36 (dd, 1H, J = 17.9 Hz, 11.3 Hz), 8.44 (dd, 1H, J = 17.9 Hz, 11.3 Hz), 10.04 (s, 1H), 10.12 (s, 1H), 10.18 (s, 2H). IR (cm^{-1}): 3302 (N-H), 2923 (C-H), 1709 (C=O), 1648 (C-N), 1066-1102 (Si-O; Si-C). UV-Vis (DMF, nm): 410 (S-band); 629, 576, 541, 507 (Q-bands). Molar extinction coefficient (λ = 410 nm; DMF; mol L^{-1} cm^{-1}): 55,400.

Quantification of the amount of PpIX loaded to PpIX-PSilQ nanoparticles using UV-vis spectroscopy

UV-Visible spectroscopy was used to confirm the amount of PpIX loaded to the PpIX-PSilQ NPs. Spectral absorbance of PpIX-PSilQ NPs dispersed in 3 mL of DMSO was measured at λ_{max} = 401 nm using Varian Cary Bio50 UV-Vis absorption spectrophotometer. The obtained

absorbance value was fitted using PpIX calibration curve in the same solvent (Figure 25). The loading percentage was calculated using the fitting equation, the volume of DMSO and the original mass of nanoparticles in the sample.

Leakage of PpIX from PpIX-PSilQ NPs

PpIX-PSilQ NPs was dispersed in DMF at a concentration of 2 mg/mL to determine the amount of PpIX leaked. The dispersion was stirred at 37 °C in the presence or absence of 10 mM DTT. The release of PpIX from the nanoparticles was measured by recording the absorbance of supernatants collected at 408 nm. The supernatant was returned to the original vial, and the nanoparticles were re-dispersed after each measurement. The measurements were taken at staggered intervals of time for a period of 8 days. The absorbance values were used to calculate the amount of PpIX leaked from the PpIX-PSilQ nanoparticles using a calibration curve of PpIX in DMF.

***In Vitro* Phototoxicity of PpIX-PSilQ nanoparticles**

The viability of A375 cells after PDT treatment with PpIX-PSilQ NPs or PpIX was analyzed by the MTS assay. The cells were seeded in 96 well plates at a density of 2,000 cells/well in 100 µL of complete DMEM and incubated at 37 °C in 5% CO_2 atmosphere for 24 h. After media removal, PpIX (0.1-100 µM) or PpIX-PSilQ NPs (at equivalent PpIX concentrations of 10-200 µM) were added to the cells in fresh media. After 48 h of incubation, cells were washed once with DPBS and irradiated with red light (630 nm, 24.5 mW/cm^2) for 20 min. Treated cells were replenished with 100 µL of fresh media and incubated for additional 24 h. Control dark experiments were conducted in parallel with PpIX-PSilQ NPs or PpIX at the same concentrations but were maintained in the dark for the entire duration of the experiment. To determine the phototoxicity of the PDT treatment, the cells were washed once with DPBS and

100 µL media was added along with 20 µL of CellTiter 96 solution to each well. The cells were incubated for 2 h at 37 °C in 5% CO_2 atmosphere. Cell viability (%) was calculated by analyzing absorbance values recorded at 490 nm using a microplate reader. Cell viability (%) was calculated as follows: viability = $(A_{sample} - A_{blank})/(A_{control} - A_{blank}) \times 100\%$, where A_{sample} , $A_{control}$ and A_{blank} denote absorbance values of the sample, control, and blank wells. The IC_{50} values are determined using GraphPad Prism (v8.3.0 for Windows, La Jolla, CA, USA), fitting the normalized viability data to a nonlinear regression.

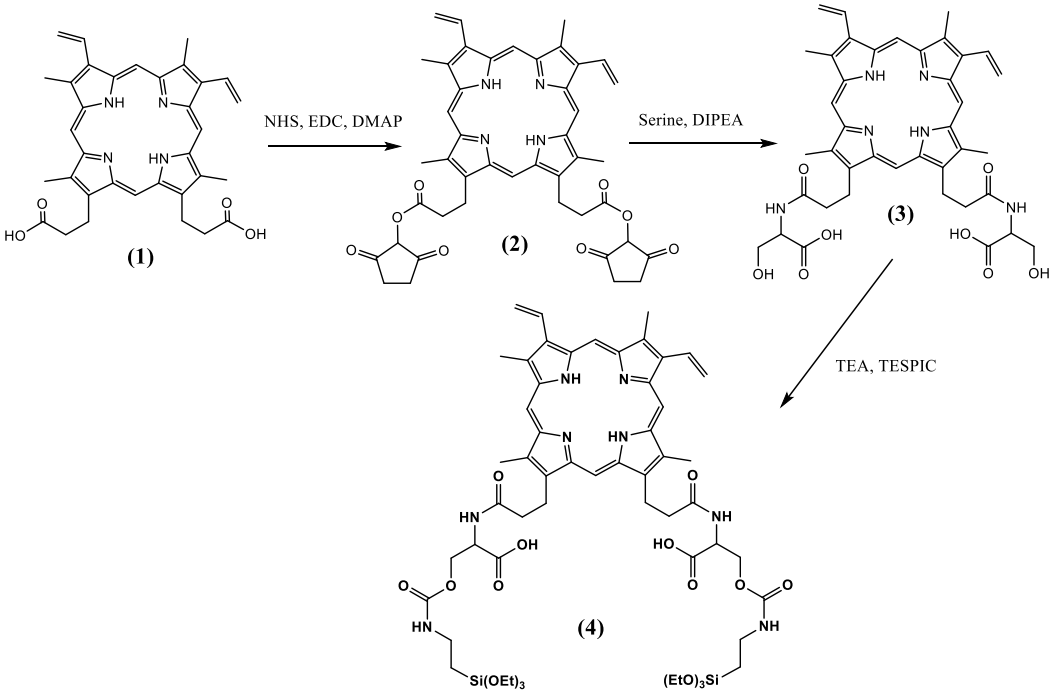

Figure 23. The carboxylic acid groups were activated through an EDC/NHS coupling reaction to afford compound **2**. Following activation, molecule **3** was synthesized by adding serine as a trifunctional linker. Finally, the isocyanate silane precursor reacted with the alcohol group through a nucleophilic acyl reaction to produce the PpIX silane monomer **4** used for the fabrication of PpIX-PSilQ NPs.

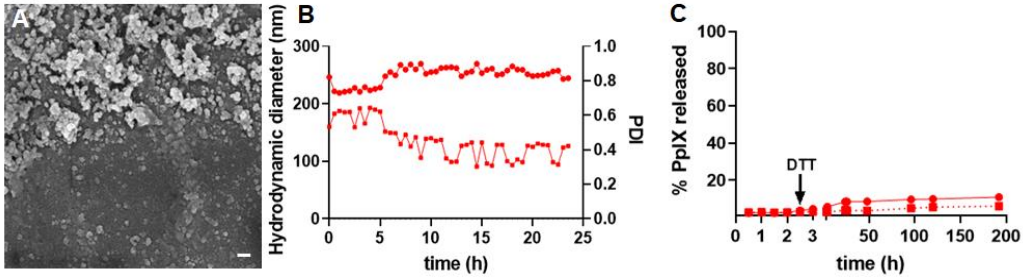

Figure 24. (**A**) SEM image of PpIX-PSilQ NPs. Scale bar= 200 nm. (**B**) Colloidal stability of the PpIX-PSilQ NPs in complete cell culture media supplemented with serum for 24 h monitored using DLS, hydrodynamic sizes are represented by (circles) and PdI represented as (squares). (**C**) Leakage of PpIX in the presence (circles) and absence (squares) of reducing agent (DTT).

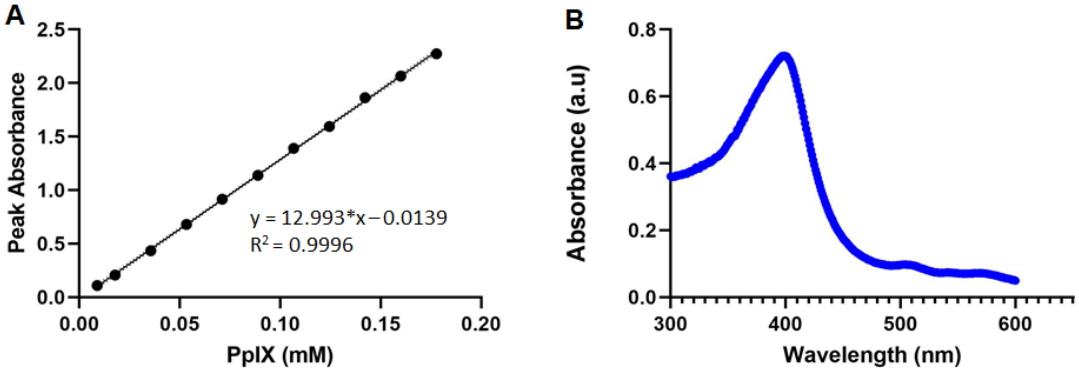

Figure 25. (**A**) Calibration curve of PpIX in DMSO (λ_{max} = 401 nm). (**B**) UV-vis spectrum of PpIX-PSilQ nanoparticles in DMSO.

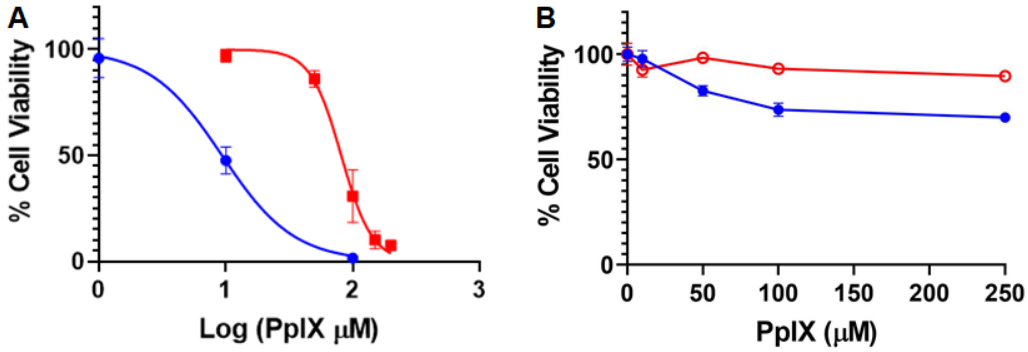

Figure 26. (A) Phototoxicity and (**B**) cytotoxicity of PpIX-PSilQ nanoparticles (red) and PpIX (blue) in A375 cells. Irradiation with red light (630 nm; 24.5 mW cm^{-2}) for 20 min (n = 6).

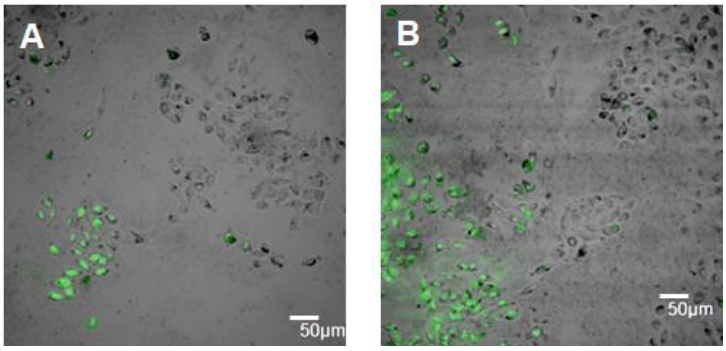

Figure 27. Intracellular ROS production in A375 cells using confocal microscopy for **(A)** PpIX-PSilQ nanoparticles (25 µM equivalent of PpIX) and **(B)** PpIX (25 µM). Images are an overlap of the green channel (DCF fluorescence) and brightfield. Scale bar = 50 µm.

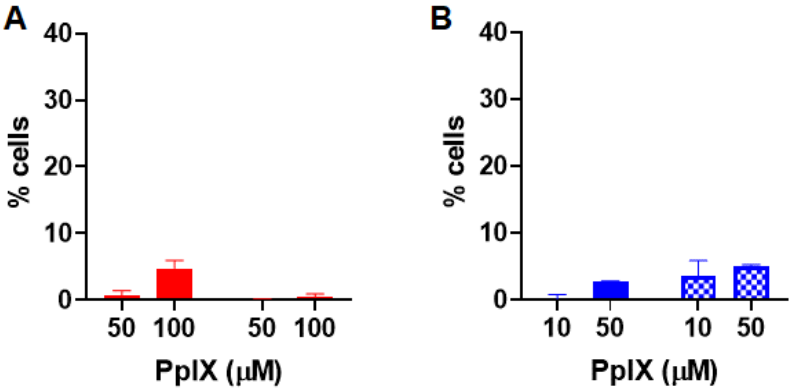

Figure 28. (**A**) Apoptotic (red solid bars) and necrotic (red checkered bars) cells treated with PpIX-PSilQ NPs (50 and 100 µM equivalent of PpIX) in the absence of light. (**B**) Apoptotic (blue solid bars) and necrotic (blue checkered bars) cells treated with PpIX (10 and 50 µM) in the absence of light. Data are represented as mean ± SD.

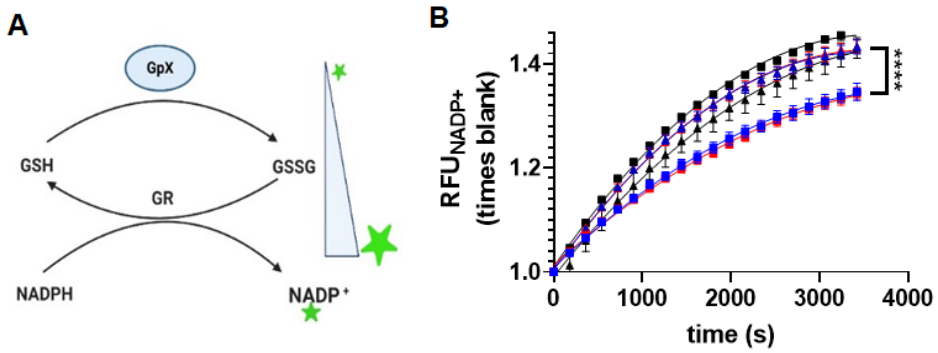

Figure 29. Inactivation of glutathione peroxidase and lipid peroxidation by PpIX-PSilQ nanoparticles. (**A**) Schematic depiction of the working principle of the GpX activity assay. The generation of $NADP^+$ is used to indirectly determine the catalytic activity of GpX. (**B**) Kinetic profiles of $NADP^+$ production for irradiated samples: control (black squares), PpIX-PSilQ NPs (50 µM PpIX eq.) (red squares), PpIX (50 µM) (blue squares); and non-irradiated samples: control (black triangles), PpIX-PSilQ NPs (50 µM PpIX eq.) (red triangles), and PpIX (50 µM) (blue triangles). Data are represented as mean ± SD. Statistics: Two-way ANOVA using Tukey's multiple comparison test: ****$p \leq 0.0001$, ***$p \leq 0.001$, **$p \leq 0.01$, *$p \leq 0.05$, and ns: $p > 0.05$.

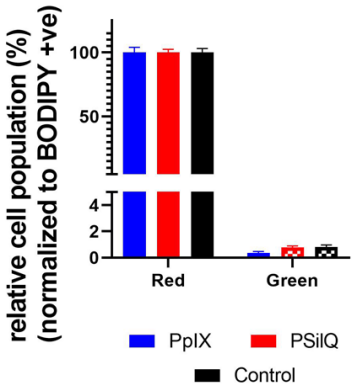

Figure 30. Quantification of lipid peroxidation using confocal microscopy in A375 cells treated with control (black), PpIX-PSilQ NPs (50 µM PpIX eq.) (red), and PpIX (50 µM) (blue) in the red (solid bars) and green (dashed bars) channels. Data are represented as mean ± SD.

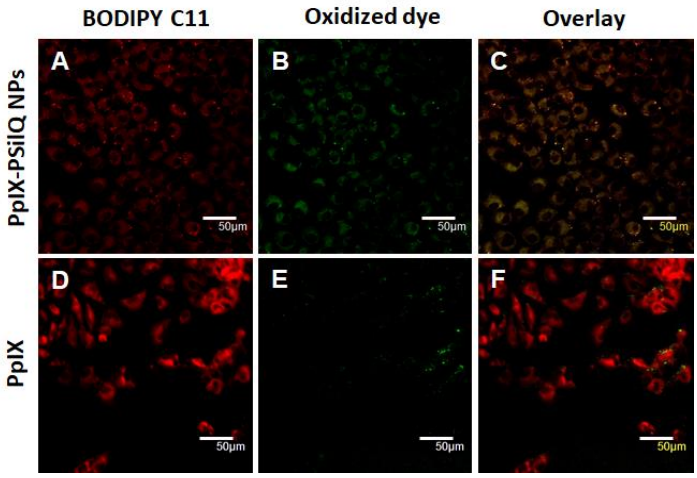

Figure 31. Lipid peroxidation detected by BODIPY™ 581/591 C-11 sensor. Confocal micrographs of A375 cells inoculated with (**A-C**) PpIX-PSilQ nanoparticles or (**D-F**) PpIX in the absence of light. The red channel depicts the presence of BODIPY 581/591 C-11 (**A**/**D**), the green channel shows the fluorescence corresponding to the oxidized version of BODIPY 581/591 C-11 (**B**/**E**), merged image of the red and green channels (**C**/**F**).

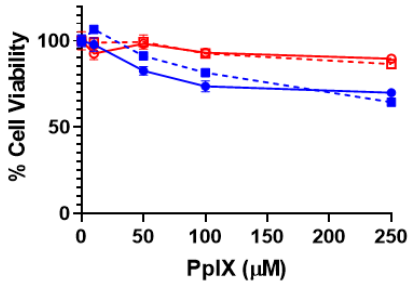

Figure 32. Cytotoxicity of PpIX-PSilQ nanoparticles (red) and PpIX (blue) in A375 cells in the absence (solid) or presence (dashed) of Ferrostatin-1 (2 µM) (n = 6).

Table 2. Hydrodynamic diameter and PdI by DLS, ζ-potential and TGA data.

DLS		
	Size/nm (PDI)	ζ-potential (mV)
PpIX-PSilQ NPs	262.6 ± 20.0 (0.40)	-35.5 ± 4.0

Material	Aromatics (%)
PpIX	62.5
PpIX Ligand 4	63.0
PpIX-PSilQ NPs	24.0 ± 2.0

4. Autophagy regulation using Multimodal Chlorin e6-loaded Polysilsesquioxane Nanoparticles to Improve Photodynamic Therapy

Citation:
Hemapriyadarshini Vadarevu, Adeola Sorinolu, Mariya Munir, Juan L. Vivero- Escoto; Autophagy regulation using Multimodal Chlorin e6-loaded Polysilsesquioxane Nanoparticles to Improve Photodynamic Therapy, Nanomedicine: Nanotechnology, Biology, and Medicine, (In preparation)

4.1. Introduction

Photodynamic therapy (PDT) is a minimally invasive localized treatment modality that has emerged as an alternative or supplementary approach to chemotherapy and surgery [86]. PDT has been clinically available and approved to treat cancers such as head and neck cancer, non-small cell lung cancer, prostate cancer, and colon cancer [229]. PDT involves three major components, namely photosensitizer (PS), light, and oxygen. During PDT, photoactivated PSs transfer energy to surrounding molecular oxygen in the cells and generate highly reactive singlet oxygen (type II) or transfer electrons to generate short-lived PS radical species (type I) that subsequently produce range of highly reactive oxygen species (ROS), such as superoxide anions, and hydroxyl radicals [95]. An overload of ROS causes significant toxicity by oxidative stress, which eventually leads to cell death [85]. Apoptosis has been reported as the primary regulated cell death mechanism in PDT [263].Furthermore, an iron-dependent cell death mechanism called ferroptosis, which is characterized by extreme cellular lipid peroxidation can also be triggered by PDT [98].

In recent years, autophagy has been studied as another cellular mechanism that impact the PDT outcome. Autophagy is a stress response program that is a consequence of PDT independent of cell death signaling [264]. Autophagy is a process of degrading and renewing cytoplasmic components, which is upregulated under cellular stress conditions such as protein aggregate accumulation, infection, and oxidative stress [265]. Mechanisms of resistance for PDT include increased expression of antioxidant genes and other protective programs like autophagy [266].

Autophagy is discussed both as a cytoprotective response and in some cases a feature of cell death following PDT, which depends on sub-cellular localization of the PS, type of ROS and target cell characteristics [264]. The process of autophagy involves the clustering of ubiquitin positive proteins into larger structures that become enclosed with autophagosomes and subsequently degraded within lysosomes after fusion [267]. Autophagy relies on the formation of double-membraned vesicles known as autophagosomes, leading to the degradation of their cargo, such as damaged proteins or organelles promoted by autophagy-related (Atg) proteins [268]. Autophagy is activated in response to external stimuli such as hypoxia, starvation and therapy in cancer cells and therefore often considered as an adaptive and pro-survival mechanism [269]. By this means, accumulation of misfolded proteins is avoided leading to prolonged survival after PDT [113, 270]. Therefore, PDT efficacy can be improved by combination approaches involving modalities that target the resistant pathways [271].

A wide variety of nanocarriers have been employed to enhance the PDT effect by increasing the stability and targeting ability of PSs [272]. In addition, nanoparticle-based formulations that combine PSs with other therapeutic agents have been recently reported. Polysilsesquioxane (PSilQ) NPs are a class of hybrid silica nanoparticles formed by crosslinking condensation of functionalized trialkoxysilanes, affording high loading capacity of the functional moiety and thus providing an interesting platform for therapeutic loading and delivery [273, 274]. PSilQ NPs have been utilized to improve the PDT effect against different types of cancers. The use of this platform for PDT treatment of cancer has been demonstrated in vitro and in vivo [233, 275]. Herein, we hypothesize that PSilQ NPs can be designed to carry both a PS agent and an autophagy inhibitor to efficiently reduce the resistant pathways related to this cellular mechanism to finally improve the PDT effect. To inhibit autophagy two strategies were pursued in this work; first, we used the

pharmacological late stage autophagy inhibitor and metal chelating agent di-2-pyridylketone 4,4-dimethyl-3-thiosemicarbazone (Dp44mT)[276]; and as second option, we utilize siRNA that suppresses the synthesis of p62/SQSTM1 autophagosome cargo protein, which plays an important role in the early stages of autophagy as it links the ubiquitin positive cargo material to the Atg8 family proteins in the nascent phagophore membrane[277].

In this work, we synthesized and characterized PSilQ NPs containing Chlorin e6 (Ce6), which is a second-generation PS agent widely used for the PDT of cancer (Ce6-PSilQ NPs). In addition, we fabricated and characterized Ce6-PSilQ NPs to address both autophagy inhibitory approaches, one loaded with Dp44mT inhibitor (Dp44mT -Ce6-PSilQ) and another one carrying siRNA that targets p62/SQSTM1 (sip62-Ce6-PSilQ NPs). The phototherapeutic performance of these materials was evaluated in vitro using HT29 colon cancer cells. PDT is widely explored for the treatment of colon cancer. Our results show that autophagy is an outcome of PDT induced oxidative stress prominently for nanoparticle formulations of PSs localized in lysosomes. Dp44mT-Ce6-PSilQ NPs prematurely terminated autophagy by blocking the fusion of autophagosomes with lysosomes with the consequent accumulation of autophagosomes that resulted in an enhancement of apoptosis. In the case of the inhibition of p62/SQSTM1 protein, the combination sip62-Ce6-PSilQ NPs did not yield the same result in enhancing PDT. The results suggest that inhibition of autophagy flux but not inhibition of proteins involved in autophagosomal sequestration boosts apoptosis after PDT by Ce6-PSilQ NPs.

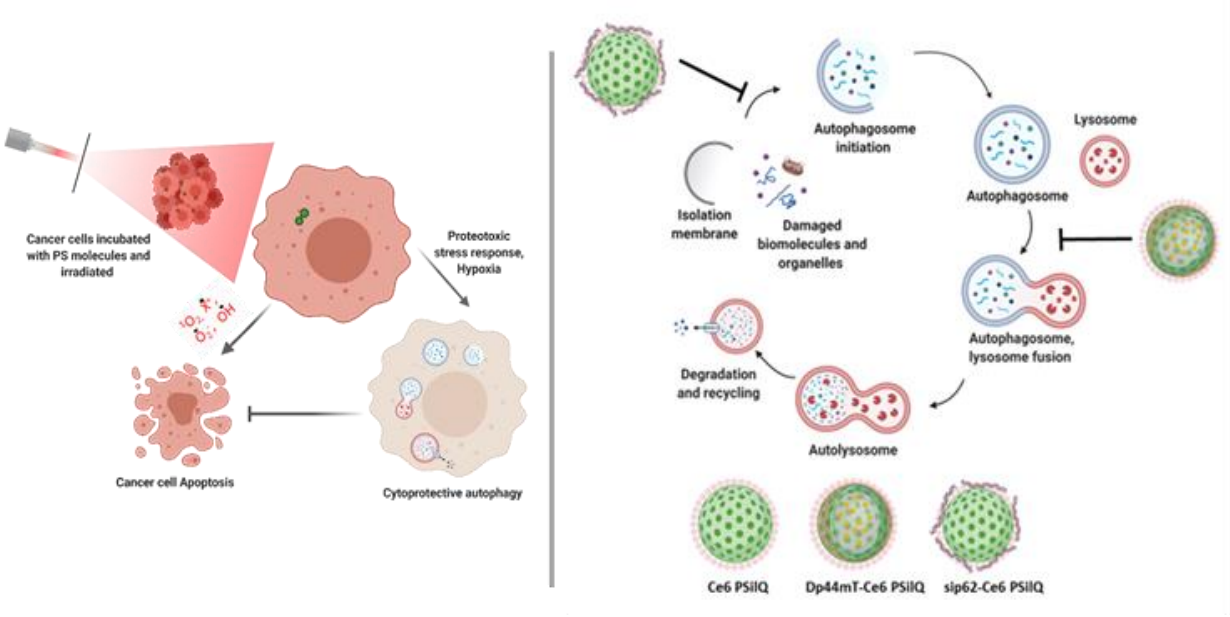

Figure 33. a. Schematic representation of the cytoprotective effect of autophagy in photodynamic therapy b. Cellular process of autophagy and proposed interference mechanisms using PSilQ nanoparticles- sip62-Ce6 PSilQ nanoparticles target early autophagosomal formation and sequestration stage or Dp44mT-Ce6 PSilQ nanoparticles target late stage autophagosome -lysosome fusion stage.

4.2. Experimental

4.2.1. Materials

hlorin e6 (Ce6), Triton X-100 (TX-100), 2',7'-dichlorodihydrofluorescein diacetate (DCFDA), Premo™ Tandem Autophagy sensor RFP-GFP-LC3 kit, Lysotracker™ Green DND-26 and SYTOX™ Blue dead cell stain were obtained from Thermo Fischer Scientific. 1- ethyl-3-(3-dimethylaminopropyl) carbodiimide (EDC) was purchased from Oakwood Chemical. Di-2-pyridylketone 4,4-dimethyl-3-thiosemicarbazone (Dp44mT), 1-hexanol and the rest of the chemicals used in this work were obtained from Sigma-Aldrich and used without any further purification unless specified otherwise. A homemade LED device emitting at 630 nm (24.5

mW/cm²) was used for our in vitro experiments (Laboratory of Technological Support, São Carlos Institute of Physics, Brazil). Roswell Park Memorial Institute (RPMI 1640), Dulbecco Modified Eagle Medium (DMEM), penicillin-streptomycin (pen-strep), phosphate buffer saline (PBS, 1X), and trypsin were purchased from Corning. CellTiter 96® Aqueous Assay was obtained from Promega (Madison, WI, USA). Glutamax was purchased from Gibco and non-essential amino acids (NEAA) was purchased from Quality biologicals. Fetal bovine serum (FBS) was purchased from Atlanta Biologicals. Hoechst 33342 dye was purchased from Life Technologies. Sterile-filtered DMSO was used for all cell experiments and purchased from Sigma. BD Pharmingen™ Annexin V-FITC Apoptosis Detection Kit was purchased from BD Biosciences. SQSTM1/p62 siRNA (h), Control siRNA-A, Control siRNA (FITC Conjugate)-A and siRNA dilution buffer were purchased from Santa Cruz Biotechnology. PureLink RNA Mini Kit and DNAse I (RNAase Free) were purchased from ThermoFisher Scientific. iScript™ cDNA Synthesis kit, PrimePCR™ SYBR Green Assay: SQSTM1 (h) and PrimePCR™ SYBR Green Assay: GADPH (h) and iTaq™ Universal SYBR Green mix were purchased from Bio-Rad Laboratories USA.

4.2.2. Synthesis of Ce6-PSilQ NPs

To fabricate Ce6-PSilQ NPs, first the Ce6 silane ligand was prepared following this protocol; 5.9 µmol (3.5 mg) of Ce6 was added into 1.4 mL of dichloromethane (DCM). To this solution, 35.3 µmol (6.8 mg) of 1-ethyl-3-(3-dimethylaminopropyl) carbodiimide (EDC) hydrochloride solution dissolved in 0.4 mL DMSO was added. The flask was then placed in an ice bath and stirred for 10 min. To this mixture, 35.3 µmol (4.1 mg) of N-hydroxysuccinimide (NHS) dissolved in 0.7 mL DMSO was added to the flask and was kept at room temperature for 3 h. A diluted ethanolic solution in water (3 mL, EtOH:H_2O/75:25% vol./vol.) was added to the flask to afford precipitation of the product (Ce6-SE). The silane derivative Ce6-TES was prepared by adding 45 µL of APTES (215 µmol) and 7 µL of TEA (73 µmol) to 12 mg (16.2 µmol) of Ce6-SE dissolved in 2 mL of

aqueous phase (DMSO:H_2O/80:20% v/v). The final solution was stirred for 1 h. This mixture was used as-prepared for the fabrication of the nanoparticles.

The synthesis of Ce6-PSilQ NPs was carried out through a reverse microemulsion method. Organic phase of the reverse microemulsion system was prepared by mixing Triton X-100 (1.8 g, 1.7 mL), 1-hexanol (1.6 mL) and cyclohexane (7.5 mL). The "*in situ*" prepared Ce6-TES reaction mixture was directly added to the organic phase under vigorous stirring (350 rpm) and room temperature. After the addition of the precursors, 100 µL of NH_4OH (25% w/w) was diluted to 10 % v/v in water and was added to the microemulsion system. The mixture was dialyzed against ethanol to destabilize the microemulsion and the formed nanoparticles were separated from the solution by centrifugation. The nanoparticles were washed twice with ethanol to remove unreacted reagents and the final product was stored in the same solvent.

4.2.3. Synthesis of Dp44mT-Ce6-PSilQ NPs

Organic phase of the reverse microemulsion system was prepared by mixing Triton X-100 (1.8 g, 1.7 mL), 1-hexanol (1.6 mL) and cyclohexane (7.5 mL). The as-prepared Ce6-TES solution and Dp44mT (0.8 mg, 2.7 µmol) dissolved in 0.2 mL of aqueous phase (DMSO:H_2O/80:20% v/v) were added to the organic phase under vigorous stirring (350 rpm) and room temperature. After the addition of the precursors, 100 µL of NH_4OH (25% w/w) was diluted to 10 % v/v in water and was added to the microemulsion system. The mixture was dialyzed against ethanol to destabilize the microemulsion and the as-made nanoparticles were separated from the solution by centrifugation. The nanoparticles were washed twice with ethanol to remove unreacted reagents and the final product was stored in the same solvent.

4.2.4. Synthesis of siRNA-Ce6-PSilQ NPs

siRNA duplexes (Santa Cruz Bio, CA) were dissolved in nuclease free cell culture grade water at a concentration of 10 µM and stored at -20 ^oC. The concentrated 10 µM stock of siRNA was further

diluted to 800 nM in siRNA dilution buffer (Santa Cruz Bio, CA). A 100 µL suspension of Ce6-PSilQ NPs (200 µM Ce6) was prepared in serum and antibiotic free DMEM. To this Ce6-PSilQ NP stock solution, 100 µL of 800 nM siRNA stock was dispensed and mixed well by pipetting. The final solution was incubated at room temperature for 30 min and spun down at 13,000 rpm for 15 min after incubation. The supernatant with any non-bonded siRNA was discarded. The nanoparticles were washed once with 200 µL of 50:50 v/v mixture of serum and antibiotic free DMEM and siRNA dilution buffer and subsequently centrifuged at 13,000 rpm for 15 min. The resulting siRNA-Ce6-PSilQ NPs were resuspended in 200 µL of serum and anti-biotic free DMEM.

4.2.5. Characterization of Ce6-PSilQ NPs

4.2.5.1. Hydrodynamic diameter and ζ-potential

To determine the hydrodynamic size and ζ-potential of Ce6-PSilQ NPs, the nanoparticles were dispersed under ultrasonication for 10 min in complete DMEM at a concentration of 0.1 mg/mL. The resultant dispersion was incubated at room temperature for 30 min before analysis using a Malvern Zetasizer nano. Measurements were conducted at 20 ^{o}C with a 2 min equilibration step between each subsequent measurement.

4.2.5.2. Determination of the amines chemically accessible on the surface of PSilQ NPs

The number of surface accessible amines for Ce6-PSilQ NPs were obtained by Kaiser's Ninhydrin test. Briefly, 1 mg of Ce6 PSilQ NPs were dispersed in 1 mL of ethanol by ultrasonication at room temperature for 15 min. This dispersion was added to 4 mL of ninhydrin stock solution prepared at a concentration of 15 mg/mL (84 mM). The reaction mixture was stirred for 14 h at room temperature and subsequently centrifuged at 13000 rpm for 15 min. Supernatants from the samples

were collected and analyzed for absorbance at 570 nm. A standard curve was used to determine the number of amines (-NH_2) (nmol/mg) in Ce6-PSilQ-NPs.

4.2.5.3. Determination of the amount loaded of Ce6 and Dp44mT

Loading amounts of Ce6 and Dp44mT in the PSilQ NPs were analyzed using Thermo scientific UHPLC plus focused series LC/UV Vanquish diode array detector system. Supernatants (5 mL) were collected from the synthesis of Ce6-PSilQ or Dp44mT-Ce6-PSilQ NPs. The supernatants were concentrated at least 10-fold by rotary evaporation. A 10 µL aliquot of the concentrated stock was subsequently diluted in 10% ethanol. A 5 µL analyte was loaded on to a Waters Symmetry Shield RP18 100 A^o, 5 µm, 2.1 mm x 150 mm column. The mobile phase comprised of water and 0.1% formic acid as the aqueous phase and acetonitrile with 0.1% formic acid as the organic phase. The flow rate of the mobile phase was 0.25 mL/min. Analytes were eluted from the column starting at 10% organic phase with a linear gradient to 100% in 6 min. After a 3 min hold time at 100% organic, the column was returned to 10% organic in 4 min followed by an equilibration time of 5 min before the next analyte sample was loaded. Ce6 standards ranged from 40 to 200 ng/mL and the detection wavelength was set to 406 nm. Dp44mT standards ranged from 100 to 400 ng/mL and the detection wavelength was set to 340 nm. Three batches were tested, and the data is presented as the average ± SD.

4.2.5.4. Absorbance and Fluorescence

The absorbance and fluorescence of Ce6-PSilQ and Dp44mT-Ce6-PSilQ materials synthesized in this work were characterized by Cary 5000 UV-vis-NIR and Fluorolog spectrophotometers, respectively. The concentration of nanoparticles used in this analysis was 20 µg/mL (5.7 µM Ce6).

4.2.5.5. Determination of singlet oxygen (1O2) in solution

Singlet oxygen generation capacity of Ce6-PSilQ NPs was tested in solution using dimethyl anthracene (DMA) as the $^1O_2$ probe. The following protocol was followed, 2 mL of an aqueous

solution containing 50 µM DMA and Ce6-PSilQ NPs (20 µg/mL, 5.7 µM Ce6) or free Ce6 (0.5 µM Ce6) were placed in quartz cuvettes under dark conditions. The solution was then illuminated under red light (λ = 630 nm, fluence rate = 24.5 mW/cm^2) for 10 min. The irradiated suspension of Ce6-PSilQ NPs was centrifuged at 13,000 rpm for 15 min and the supernatant was gathered for analysis. The absorption spectra of the irradiated samples were recorded. The $^1O_2$ generation was qualitatively confirmed by absorbance intensities of DMA after irradiation.

4.2.6. Cell culture

Human colon cancer cell line HT29 was purchased from the American Type Culture Collection (ATCC, USA). HT29 cells were cultured in Dulbecco's modified Eagle's medium (DMEM, Thermo Fisher Scientific, Waltham, MA, USA) supplemented with 10% fetal bovine serum (Thermo Fisher Scientific), 1% penicillin/streptomycin (HyClone, Logan, UT, USA), 1% Glutamax (Gibco, Grand Island, New York) and 1% non-essential amino acids (NEAA, Quality Biological, Gaithersburg, Maryland). Cells were incubated in a humidified atmosphere of 5% CO_2 at 37 °C.

4.2.7. Stock solutions for PDT

Ce6 and Dp44mT were dissolved in DMSO as 1 mM stock solutions respectively and stored at −20 °C, protected from light. Working solutions of Ce6 and Dp44mT were prepared fresh at various concentrations in complete DMEM before adding to cells. DCFDA was dissolved as a 10 mM stock solution in DMSO, protected from light. A 10 µM working solution of DCFDA was prepared from the 10 mM stock in serum free DMEM before adding to cells. The prepared siRNA-Ce6-PSilQ NP stock solution (100 µM Ce6, 400 nM siRNA) was serially diluted in serum and antibiotic free DMEM in the concentration range of 4-40 nM range and added to cells for treatment.

4.2.8. Cellular uptake and intracellular localization of FITC-conjugated siRNA-Ce6-PSilQ NPs.

HT29 cells were cultured at a density of 20,000 cells per well in a 24-well plate containing 500 µL media and maintained for 24 h at 37 °C with 5% CO_2 in a humidified incubator. Cells were then treated with Ce6-PSilQ NPs (0.5 mL) at concentrations equivalent to 5 and 10 µM Ce6 and incubated for 12-14 h at 5% CO_2 atmosphere at 37°C. Afterwards, the cells were washed with phosphate buffer, followed by detachment of cells using 0.25% trypsin-EDTA. The cells were then suspended in DBPS for analysis with the flow cytometer (BD LSR ™ cell analyzer) using PE-Cy7-a channel. Ce6-PSilQ NPs equivalent to 10 µM Ce6 were complexed with 40 nM FITC conjugated control siRNA to give FITC-labeled $siRNA^{FITC}$-Ce6-PSilQ NPs. HT29 cells were seeded at 30,000 cells per well in a 24-well plate containing 500 µL complete DMEM and maintained for 24 h in a humidified incubator at 37 ^{o}C with 5 % CO_2. Cells were then treated with $siRNA^{FITC}$-Ce6-PSilQ NPs at Ce6 concentrations equivalent to 5 and 10 µM suspended in serum and antibiotic free DMEM and incubated for 24 h at 5% CO_2 atmosphere at 37 °C. Following treatment, the cells were washed with DPBS twice and harvested using trypsin. Cells were resuspended in DPBS for flow cytometry analysis using PE Cy7-A and FITC channels for Ce6 and $siRNA^{FITC}$, respectively. For confocal laser scanning microscopy, HT29 cells at a density of 100,000 cells per well were seeded onto a coverslip placed in 6-well plates and incubated at 37 °C with 5% CO_2 atmosphere to allow adhesion. After incubation time of 24 h, the cells were treated with $siRNA^{FITC}$-Ce6-PSilQ at a fixed concentration of 10 µM in 2 mL of serum and antibiotic free media for a period of 12-14 h. Cells were rinsed three times with cold PBS and nuclei were stained with Hoescht 33342 for 15 min at 37 ^{o}C in a humified incubator. After additional rinse with PBS, the coverslips were mounted onto the glass slides with media and imaged using an Olympus Fluoview FV 1000 confocal laser scanning microscope.

4.2.9. Phototoxicity assessment

The MTS cell proliferation assay was used to determine cell viability. HT29 cells (3,000 cells per well) were seeded into 96-well plates and incubated overnight at 37 °C. After that, the cells were treated with various concentrations of Ce6-PSilQ NPs or free Ce6 ranging from 1 to 5 µM Ce6 and incubated for 24 h at 37 ºC. To analyze cell viability with the combine treatment of PDT and autophagy inhibitor, Dp44mT-Ce6-PSilQ NPs or a 1:6 molar mixture of free Ce6 and Dp44mT were added at concentrations ranging from 1 to 20 µM based on Ce6. The cells were incubated for 24 h at 37 ºC. To evaluate the PDT in combination with siRNA induced gene silencing, siNeg-Ce6-PSilQ NPs or sip62-Ce6-PSilQ NPs were added at Ce6 concentrations ranging from 1 to 20 µM of Ce6 and 4 to 80 nM of siRNA. The treated cells were incubated for 24 h at 37 ºC. Next, cells were washed once with cold DPBS followed by irradiation with red light (633 nm, 25 mW/cm^2) for 20 min in cold DPBS. The solution was aspirated, and cells were resuspended in complete DMEM and incubated at 37 ºC for an additional 24 h. Subsequently, cells were incubated at 37 ºC with 20% v/v of the CellTiter 96® MTS solution in complete DMEM for 4 h. In parallel, one unirradiated duplicate plate was maintained for each treatment condition to serve as a control (dark) experiment. Finally, the optical density value of each well at 490 nm was measured using a Multiskan microplate reader. Cell viability (%) was calculated by analyzing absorbance values recorded at 490 nm using a microplate reader. Cell viability (%) was calculated as follows: viability = $(A_{sample} - A_{blank})/(A_{control} - A_{blank}) \times 100\%$, where A_{sample} , $A_{control}$ and A_{blank} denote absorbance values of the sample, control, and blank wells. The IC_{50} values are determined using GraphPad Prism (v8.3.0 for Windows, La Jolla, CA, USA), fitting the normalized viability data to a nonlinear regression.

4.2.10. Measurement of intracellular ROS level

HT29 cells were seeded in 6 well plates at a density of 50,000 cells per well and incubated at 37 °C for 24 h. After that, the cells were treated with Ce6-PSilQ NPs or free Ce6 at concentration equivalent to 2.4 µM Ce6 or Dp44mT-Ce6-PSilQ or a mixture of Dp44mT:Ce6 (1:6 molar) at concentrations equivalent to 2.4 µM Ce6 and 0.4 µM Dp44mT. The cells were incubated for 24 h at 37 ^{o}C. Next, cells were washed once with cold DPBS and incubated in serum free media containing 10 µM DCFDA for 30 min at 37 °C in the dark, and then cells were washed twice with DPBS and irradiated with red light (630 nm, 25 mW/cm^2) for 20 min in cold DPBS. Cells were collected by trypsinization and resuspended in DPBS before reading out ROS positive population by flow cytometry (BD Fortessa). In parallel, one unirradiated duplicate plate was maintained for each treatment condition to serve as a control (dark) experiment. DCFDA stained blank cells were seeded in each plate and used to determine the background fluorescence.

4.2.11. Autophagy Assessment by flow cytometry

HT29 cells were seeded in 6 well plates at a density of 50,000 cells per well and incubated at 37 °C for 24 h. After that, the cells were treated with Ce6-PSilQ NPs or free Ce6 at concentration equivalent to 2.4 µM Ce6 or Dp44mT- Ce6-PSilQ NPs or a mixture of Dp44mT:Ce6 (1:6 molar) at concentrations equivalent to 2.4 µM Ce6 and 0.4 µM Dp44mT . HT29 cells were cultured in serum free media to mimic serum starvation and promote macro autophagy. Serum starved cells treated with 10 µM chloroquine were used as a positive control group. The cells were incubated for 24 h at 37 ^{o}C. The cells were subsequently infected with the RFP-GFP-LC3 baculoviral (ThermoFisher Scientific) constructs using a concentration of 30 viral particles per cell. The infected cells were incubated for 16 h at 37 ^{o}C and 5% CO_2. Subsequently, the cells were irradiated using red light (630 nm, 25 mW/cm^2) for 20 min at room temperature after washing twice with

DPBS. RFP positive populations and GFP positive populations were read out by flow cytometry (BD Fortessa) 6 h after irradiation.

4.2.12. Autophagy Assessment by confocal microscopy

HT29 cells were seed in a 6 well plate with glass coverslips at a density of 25,000 cells per well and incubated at 37 °C for 24 h. After that, the cells were treated with Ce6-PSilQ NPs or Dp44mT-Ce6-PSilQ NPs at concentration equivalent to 1.2 µM Ce6 and incubated for 24 h at 37 ^{o}C. The cells were subsequently infected with the RFP-GFP-LC3 baculoviral (ThermoFisher Scientific) constructs using a concentration of 30 viral particles per cell. The infected cells were incubated for 16 h at 37 ^{o}C and 5% CO_2. Subsequently, the cells were irradiated using red light (630 nm, 25 mW/cm^2) for 20 min at room temperature after washing twice with DPBS. Cells were replenished with media for 6 h and after that the glass coverslips were washed once with DBPS and mounted onto glass slides for imaging autophagic vesicles by confocal microscopy (Olympus Fluoview).

4.2.13. In vitro analysis of cell apoptosis and necrosis

Annexin V-FITC with live/dead co-staining was used for the assessment of cell apoptosis. HT29 cells were seeded into 6-well plates at a density of 50,000 cells per well and incubated overnight at 37 °C. After that, the cells were treated with various concentrations of Ce6-PSilQ NPs or free Ce6 at concentration equivalent to 2.4 µM Ce6 and incubated for 24 h at 37 ^{o}C. To determine the apoptotic effect caused by the combined treatment of PDT and autophagy inhibitor, Dp44mT-Ce6-PSilQ NPs or a mixture of Ce6:Dp44mT (1:6 molar) at concentrations equivalent to 2.4 µM Ce6 and 0.4 µM Dp44mT were added. The inoculated cells were incubated for 24 h at 37 ^{o}C. Next, cells were washed once with cold DPBS followed by irradiation with red light (633 nm, 25 mW/cm^2) for 20 min in cold DPBS. The solution was removed and complete DMEM was added to the cells, which were incubated at 37 ^{o}C for an additional 24 h. Subsequently, the cells were washed once with DPBS and once with binding buffer (0.1x, BD biosciences). After that, the cells

were suspended in binding buffer, followed by the addition of 5 µL of Annexin V-FITC staining solution for 15 min, and then washed once with the binding buffer (0.1x). Afterwards, 5 µL SYTOX Blue (Thermo Fisher Scientific) staining solution was added for 5 min. Finally, the percentage of apoptotic cells was determined using flow cytometry directly after SYTOX Blue staining without an intermediate wash step. The cell apoptosis assessment for PDT in combination with sip62 was carried out using the following materials: siNeg-Ce6-PSilQ NPs or sip62-Ce6-PSilQ NPs at concentrations equivalent to 2.4 µM and 4.8 µM of Ce6 and 9.6 nM and 19.2 nM of sip62 duplexes. The cells were inoculated with the materials and incubated for 24 h at 37 ^{o}C. Next, cells were washed once with cold DPBS followed by irradiation with red light (633 nm, 25 mW/cm^2) for 20 min in cold DPBS. The solution was removed and complete DMEM was added to the cells, which were incubated at 37 ^{o}C for an additional 24 h. The cells were treated following the protocol described above to determine the percentage of apoptotic cells.

4.2.14. Relative mRNA expression

The knockdown of p62/SQSTM1 expression was evaluated by quantitative PCR. HT29 cells were grown in 6-well plates at a seeding density of 100,000 cells per well. The cells were maintained for 24 h at 37 ^{o}C and 5% CO_2 atmosphere. The cells were then treated for 24 h with Ce6-PSilQ NPs or siNeg-Ce6-PSilQ NPs or sip62-Ce6-PSilQ NPs at concentrations of 2.4 µM Ce6 and 9.6 nM siRNA. The cells were rinsed once with PBS, detached from tissue culture treated surface using cell dissociation buffer (Thermo Fisher Scientific), and collected via centrifugation. The isolation and purification of RNA from cells was carried out using Purelink RNA mini kit along with in column DNase I treatment. Purified RNA was eluted in nuclease free water and stored at -20 ^{o}C. The cDNA synthesis was performed using iScript cDNA synthesis kit (1708890, Bio-Rad). The extracted RNA was mixed with iScript reaction mix, iScript reverse transcriptase, and nuclease-free water as per the manufacturer's protocol. The complete reaction mix was incubated

in a thermal cycler programmed with the following protocol: 5 min priming at 25 ºC, 20 min reverse transcription at 46 ºC, and 1 min RT inactivation at 95 ºC. The contents were held at 4 ºC. After the cDNA synthesis, RT-PCR was performed using SYBR Green Supermix (Bio-Rad) and a CFX96 Real-Time System (Bio-Rad). A 20 µL solution was prepared using 10 µL of Universal SYBR Green Supermix, 1 µL of PrimePCR primer pair mix (Biorad), 100 ng of cDNA and nuclease free water. The solution was then subjected to the following protocol: an initial step of 95 ºC for 30 s for polymerase activation and DNA denaturation; followed by 35x cycles of 95 ºC for 15 s, 60 ºC for 30 s, and a fluorescence reading. The mRNA expression relative to untreated cells was then quantified in the Bio-Rad CFX Manager software using the ΔΔCq method with a GAPDH reference.

4.2.15. Statistics

All the experimental results in the manuscript are reported as mean ± standard deviation (SD) unless mentioned otherwise. For the analysis of nanoparticle size using TEM, 50 nanoparticles were evaluated using Image J. The hydrodynamic size, ζ-potential, and Kaiser's ninhydrin test were carried out in triplicates or more. The amount of Ce6 and Dp44mT loaded was analyzed in triplicates using three different batches of nanoparticles. Cellular uptake, apoptosis and autophagy assays were evaluated using flow cytometry with a minimum of 10000 singlets and quantified in triplicates. For the cell viability studies, GraphPad Prism was used to calculate the IC_{50} values (n=6). Statistical analysis was done by one-way ANOVA using Tukey's multiple comparison test. All the statistical analysis was performed using GraphPad Prism (v8.2.0) with a p-value < 0.05 considered to be statistically significant.

4.3. Results and discussion

4.3.1. Synthesis and physicochemical characterization of Ce6-PSilQ NPs

In this work, we fabricated Ce6-PSilQ NPs, Dp44mT-Ce6-PSilQ NPs and siRNA-Ce6-PSilQ NPs. These materials produce cancer cell death through the simultaneous combination of PDT and the inhibition of the pro-survival autophagy mechanism. First, we synthesized "in situ" the Ce6-silane precursor (Ce6-TES) through a conjugation reaction between Ce6 molecule and APTES. A reverse microemulsion approach was used for the fabrication of Ce6-PSilQ NPs using Ce6-TES. TEM images of the nanoparticles were analyzed to obtain the size and morphology of Ce6-PSilQ NPs, which are spherical with a diameter of 42.3 ± 7.1 nm (n=50) (Figure 34). The hydrodynamic diameter of Ce6-PSilQ NPs in PBS was determined to be 324.2 ± 2.9 nm (Figure 34). The ζ-potential was measured as +20.9 ± 0.4 mV.

In the case of Dp44mT-Ce6-PSilQ material, Dp44mT was added to the microemulsion during the first step before addition of the catalyst to maximize the loading of the molecule. To synthesize Dp44mT-Ce6-PSilQ NPs, the ratio 1:6 mol of Dp44mT:Ce6 was selected as the mixing ratio to be added to the reverse microemulsion during the formation of nanoparticles. The mixing ratio used is in the synergistic range of combination between Dp44mT and Ce6 for PDT as seen in table 2 (appendix). The TEM images were analyzed to obtain the size and morphology of Dp44mT-Ce6-PSilQ NPs, which are spherical with a diameter of 46.9 ± 8.9 nm (n=50) (appendix). The hydrodynamic diameter of Dp44mT-Ce6-PSilQ NPs in PBS was determined to be 376.1 ± 7.6 nm (Figure 34). The ζ-potential was measured as +21.8 ± 0.9 mV (Figure 34). Loading capacity of Dp44mT and Ce6 in Dp44mT-Ce6-PSilQ NPs were quantified as 1.2 ± 0.2 and 15.8 ± 1.6 % w/w (1:6 mol ratio) using reverse phase HPLC (data not shown). Fluorescence spectroscopy further confirm the presence of both Ce6 and Dp44mT as observed in Figure 34**f** with maximum peaks at 670 and 510 nm, respectively.

The siRNA- and sip62-Ce6-PSilQ NPs were prepared by taking advantage of the positive charge on the surface of the Ce6-PSilQ nanoparticles to electrostatically interact with siRNA. Due to the small amount of material (<50 nM) obtained through this method no further characterization of the nanoparticles was carried out.

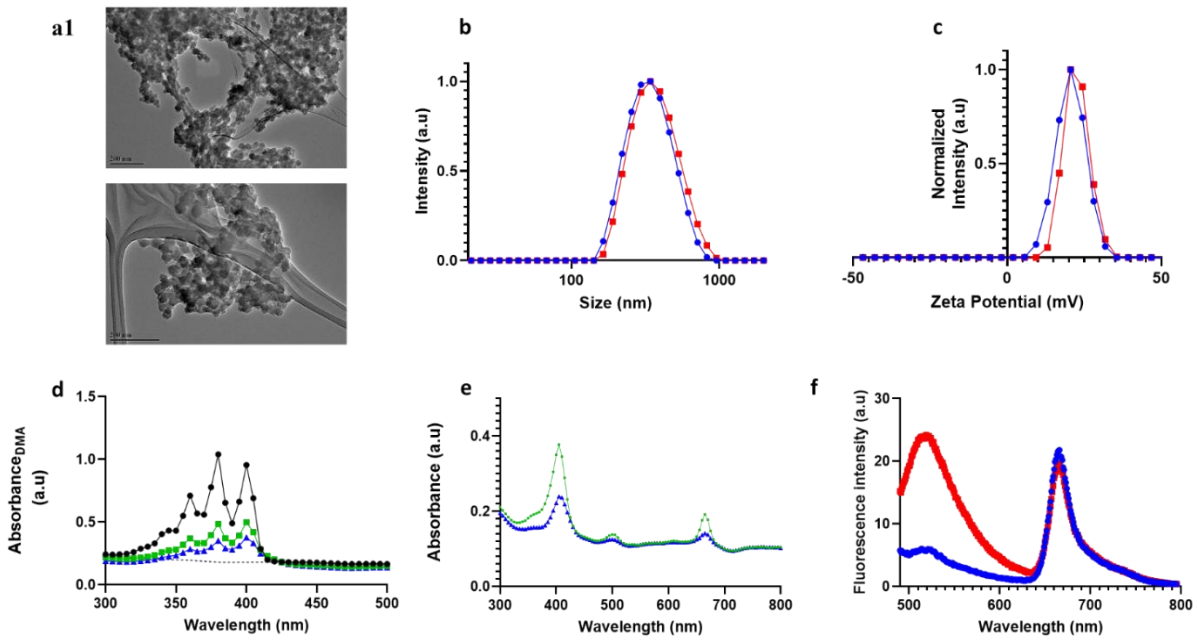

Figure 34. a) TEM images of Ce6-PSilQ NPs. b) Hydrodynamic diameter of Ce6-PSilQ (blue) and Dp44mT-Ce6-PSilQ (red) NPs as measured by DLS. C) ζ-potential of Ce6-PSilQ (blue) and Dp44mT-Ce6-PSilQ (red) NPs. d) Indirect determination of singlet oxygen formation using DMA for Ce6 (green) and Ce6-PSilQ NPs (blue). e) UV-vis spectra of Ce6 (green) and Ce6-PSilQ NPs (blue). f) Fluorescence spectra of Ce6-PSilQ (blue) and Dp44mT-Ce6-PSilQ (red) NPs.

Cellular uptake of Ce6 PSilQ NPs was analyzed using flow cytometry (Figure 35). Uptake efficiency of the particles was obtained as 33.0 ± 1.8 % Ce6 positive cells at 5 µM [Ce6]. Average uptake efficiency increased by 12% when concentration was increased to 10 µM [Ce6]. Confocal fluorescence imaging of Ce6 PSilQ NPs at 10 µM [Ce6] by HT29 cells revealed successful uptake of the nanoparticles at 37 ^{o}C after 12 h of incubation. The overlapping fluorescence between stained lysosomes (green) and Ce6 PSilQ NPs (red) in Figure 35b depicts localization of the NPs in lysosomes presumably by endolysosomal pathway. Ce6 PSilQ NPs can also been seen in the perinuclear space and cell membrane of HT29 cells.

4.3.2. Phototoxicity of Ce6-PSilQ NPs and Dp44mT-Ce6-PSilQ NPs in HT29 cells

The phototoxic profile of Ce6-PSilQ NPs and Dp44mT-Ce6-PSilQ NPs in HT29 cells was measured using MTS assay (Figure 37b). The IC50 values for Ce6-PSilQ NPs and Dp44mT-Ce6-PSilQ NPs post irradiation were obtained as 12.8 ± 0.7 µM [Ce6] and 3.3 ± 0.2 µM [Ce6]/0.5 ± 0.0 µM [Dp44mT], respectively. More than 90 % viability was observed in HT29 cells treated with Ce6 PSilQ NPs at 28 µM [Ce6] and Dp44mT Ce6 PSilQ NPs at 25 µM [Ce6]/ 4 µM [Dp44mT]. A five-fold reduction in the phototoxicity of Ce6 was observed in HT29 cells when delivered as Ce6 PSilQ NPs as opposed to DMSO solvated free Ce6. The results show an approximately four-fold decrease in the IC50 associated with Ce6 as a result of the combination with Dp44mT delivered to HT29 cells as a nano-formulation compared to Ce6 PSilQ NPs alone. Interestingly, the cytotoxicity related to Dp44mT is reduced when it is loaded to the Ce6-PSilQ NPs as observed in the dark toxicity profile of Dp44mT-Ce6-PSilQ (Figure 36c). This can be gathered from the IC50 concentration of free Dp44mT (~ 0.1 µM) (table 2 appendix) while Dp44mT Ce6 PSilQ NPs did not exhibit any cytotoxicity in HT29 cells (with >90% viability) for concentration range of 0.2-1 µM [Dp44mT].

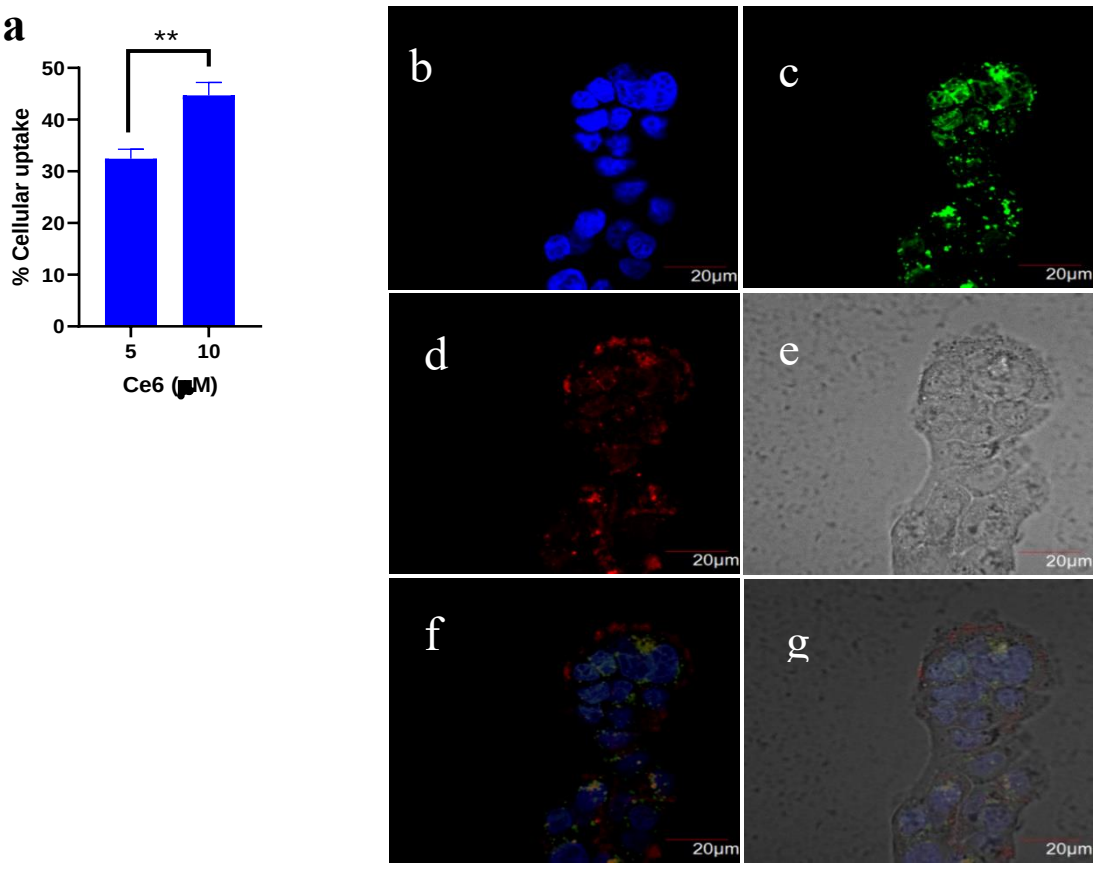

Figure 35. a) Cellular uptake of Ce6-PSilQ (blue) by HT29 cells. Confocal microscopy images of HT29 cells treated with Ce6 PSilQ NPs b) Hoescht 33342 channel c) Lysotracker green channel d) Ce6 PSilQ channel e) grayscale dpi channel f) merged blue, green, and red channels g) merged blue, green, red, and grayscale channels. Scale bar measures 20 μm.

4.3.3. ROS production related to Ce6-PSilQ and Dp44mT-Ce6-PSilQ nanoparticles

Production of ROS (type I) associated with PDT was measured in HT29 cells using DCFH-DA as a fluorescent ROS probe. DCFH-DA is deacetylated by cellular esterases to a non-fluorescent compound, which is later oxidized by ROS into fluorescent 2′,7′- dichlorofluorescein (DCF) . HT29 cells were treated with Ce6-PSilQ or Dp44mT-Ce6-PSilQ nanoparticles at 2.4 μM [Ce6]. Quantification of ROS generated after irradiation (630 nm, 25 mW/cm^2, 20 min) shows 32.8 ± 0.3 % and 44.3 ± 2.5 % of DCF positive cells for the Ce6-PSilQ and Dp44mT-Ce6-PSilQ NPs,

respectively (Figure 37**a**). In the case of free drugs, 22.4 ± 1.6 % and 94.2 ± 0.8 % of DCF positive cells were measured post irradiation for Ce6 and the physical mixture of Ce6/Dp44mT, respectively (Figure 37**a**). No significant ROS generation was observed for Ce6 and Ce6-PSilQ NPs in dark conditions (Figure 37**a)**. Interestingly, in the absence of light irradiation, Dp44mT-Ce6-PSilQ NPs and the mixture of Ce6/Dp44mT induced 14.3 ± 2.6% and 73.2 ± 2.1 % DCF positive cells, respectively. These results show that Dp44mT has also a major impact in the generation of ROS.

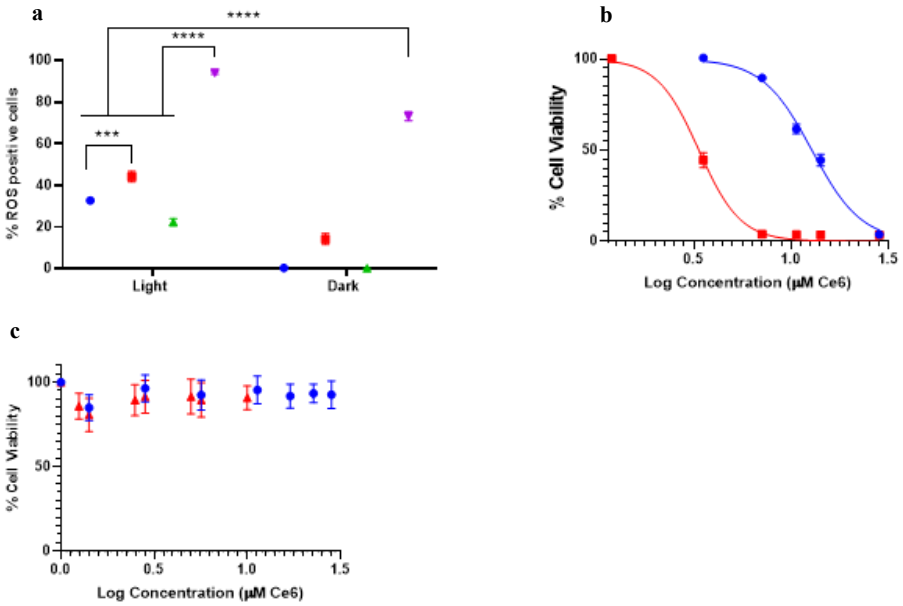

Figure 36. a) ROS production in HT29 cells treated with Ce6-PSilQ NPs (blue), Dp44mT-Ce6-PSilQ (red) NPs, Ce6 (green), Dp44mT/Ce6 (purple) b) Phototoxicity analysis of HT29 cells treated with Ce6-PSilQ NPs (blue), Dp44mT-Ce6-PSilQ (red) NPs c) Dark cytotoxicity analysis of HT29 cells treated with Ce6-PSilQ NPs (blue), Dp44mT-Ce6-PSilQ (red) NPs. Data are represented as mean ± SD. Statistics: two-way ANOVA using Tukey's multiple comparison test: **** $p \leq 0.001$, *** $p \leq 0.001$, ** $p \leq 0.01$, * $p \leq 0.05$, and ns: $p > 0.05$.

4.3.4. Effect of the combination Dp44mT-Ce6-PSilQ nanoparticles to inhibit autophagy

HT29 cells were modified to express mRFP GFP LC3, which allows measuring the autophagic flux. This probe makes it possible to distinguish autophagosomes (GFP-positive and RFP-positive LC3 punctae, which are yellow) from the more acidic autolysosomes (GFP-negative and RFP-positive LC3 punctae, which are red). Autophagy flux was indirectly estimated by RFP to GFP mean fluorescence intensity (MFI) ratio of 10,000 single HT29 cells for each sample by flow cytometry. Basal flux of untreated transduced HT29 cells was used as the baseline for normalization. As seen in **Figure 38a**, the normalized autophagy flux of Ce6-PSilQ NPs was 10.61 ± 0.98, which was reduced to 4.98 ± 0.62 for Dp44mT-Ce6-PSilQ NPs. Cells treated with 30 μM

of chloroquine were used as the positive control group for the assay expressing an MFI ratio of 2.4 ± 0.03[278]. The decrease in autophagy flux associated with Dp44mT-Ce6-PSilQ NPs when compared to Ce6-PSilQ NPs confirms the flux inhibitory role of Dp44mT in cellular autophagy. Reduction in autophagy flux was also observed for the free drugs treatment, from 4.72 ± 0.53 for free Ce6 to 1.57 ± 0.06 when combined with Dp44mT (**Figure 38a**). Autophagy flux of serum starved cells was measured as 4.05 ± 0.44 (Figure 38a) which was decreased by CQ to 2.40 ± 0.01. MFI ratios of unirradiated Ce6-PSilQ and Ce6 were detected in the range of 1.1-1.3 while Dp44mT-Ce6-PSilQ and Ce6/Dp44mT were in the range of 2.3-3.1. ROS generated by Dp44mT in both Dp44mT Ce6 PSilQ and Ce6/Dp44mT mixtures contribute to autophagy above basal levels. These results were further confirmed by confocal microscopy (**Figures appendix**).

4.3.5. Effect of the combination Dp44mT-Ce6-PSilQ nanoparticles on the PDT associated cell death pathways

The amount of apoptotic and/or necrotic cells produced due to PDT effect of Ce6-PSilQ and Dp44mT-Ce6-PSilQ NPs was analyzed by flow cytometry using the SYTOX Blue dead-cell nuclear stain assay and Annexin V Apoptosis detection Kit. Concentration of nanoparticles and free drugs evaluated in this experiment were 2.4 µM of Ce6 and 0.4 µM of Dp44mT. Cells treated with Ce6-PSilQ and Dp44mT- Ce6-PSilQ NPs in the presence of light (633 nm, 25 mW/cm^2, 20 min) showed 14.8 ± 1.0 % and 52.3 ± 0.4 % of Annexin-V-positive cells, respectively (**Figure 38b**). Dark controls for Ce6-PSilQ and Dp44mT-Ce6-PSilQ NPs, under the same concentrations, were used as negative controls showing less than 1.0 % and 3.7 ± 0.4 % of Annexin-V-positive cells, respectively (**Figure 38b**). HT29 cells treated with Ce6-PSilQ and Dp44mT-Ce6-PSilQ NPs in the presence of light showed 5.6 ± 0.2 % and 12.2 ± 0.3 % necrotic-positive cells, respectively (**Figure 38c**). In the absence of light, the treatment with these nanoparticles led to less than 1% necrotic-positive cells (**Figure 38c**). A similar apoptotic/necrotic analysis was performed for free

drugs. As depicted in (**Figure 38b**), HT29 cells treated with Ce6 or the combination Ce6/Dp44mT after light irradiation exhibited 58.7 ± 0.8 % and 84.0 ± 0.8 % of Annexin-V-positive cells, respectively. Dark controls for the same free drugs show less than 1 ± 0.4 % and 7.7 ± 0.4 % of Annexin-V-positive cells (**Figure 38b**). The percentages of HT29 cells undergoing necrosis under the treatment with Ce6 and the combination of Ce6/Dp44mT in presence of light were 15.4 ± 0.5 % and 5.1 ± 0.4 % of necrotic-positive cells (**Figure 38c**). Dark controls of the same free drugs showed 4.2 ± 1.3 % and 1.2 ± 0.2 %. ROS from Dp44mT alone (Figure 37a) in the unirradiated samples does not cause significant cell death (Figure 38b) . This indicates a co-dependent interaction between Ce6, Dp44mT and light for an improved therapeutic outcome.

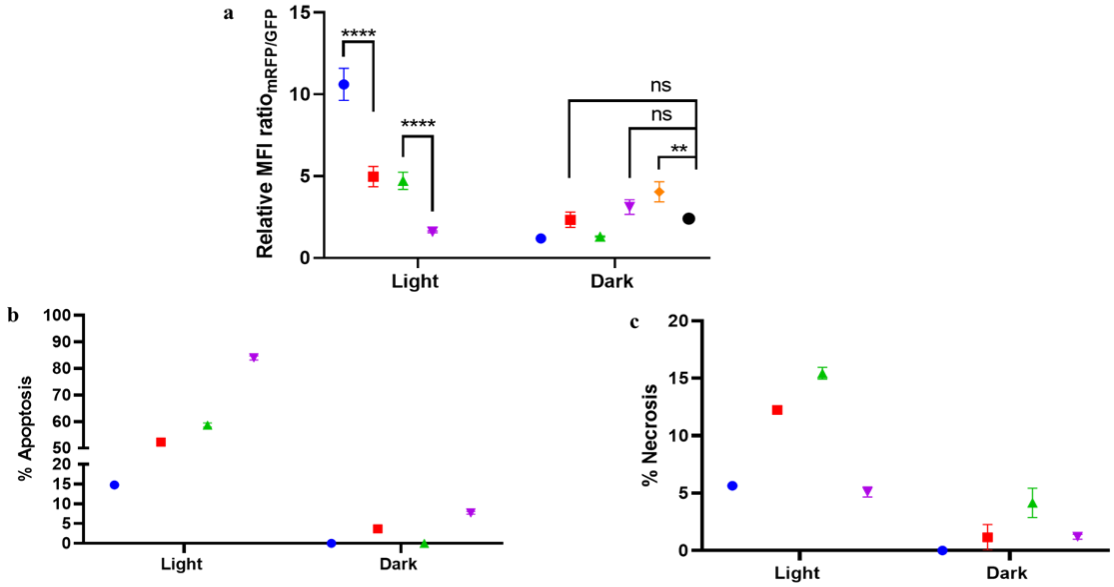

Figure 37. a) Autophagy flux analysis of HT29 cells treated with Ce6-PSilQ NPs (blue), Dp44mT-Ce6-PSilQ (red) NPs, Ce6 (green), Dp44mT/Ce6 (purple), serum starved (orange) and chloroquine (black). b) Apoptosis analysis of HT29 cells treated with Ce6-PSilQ NPs (blue), Dp44mT-Ce6-PSilQ (red) NPs, Ce6 (green) and Dp44mT/Ce6 (purple). c) Necrosis analysis of HT29 cells treated with Ce6-PSilQ NPs (blue), Dp44mT-Ce6-PSilQ (red) NPs, Ce6 (green) and Dp44mT/Ce6 (purple). Data are represented as mean ± SD. Statistics: two-way ANOVA using Tukey's multiple comparison test: **** $p \leq 0.001$, *** $p \leq 0.001$, ** $p \leq 0.01$, * $p \leq 0.05$, and ns: $p > 0.05$.

4.3.6. Effect of the combination sip62-Ce6-PSilQ nanoparticles to inhibit autophagy, phototoxicity and on the PDT associated cell death pathways

We evaluate the performance of sip62-Ce6-PSilQ NPs to inhibit autophagy by siRNA mediated silencing of p62 gene (sip62), and its impact on the PDT outcome of the nanoparticles in HT29 cells. First, we determined the siRNA cellular uptake efficiency using FITC-labeled RNA that does not have any silencing effect ($siNeg^{FITC}$). HT29 cells were treated with $siNeg^{FITC}$-Ce6-PSilQ NPs at 5 µM and 10 µM [Ce6] complexed to 40 nM and 20 nM $siNeg^{FITC}$, respectively. The results showed concentration dependent uptake of siNeg-Ce6-PSilQ (**Figure 39a**). 28.2 ± 0.14 % and 43.6 ± 1.7 % Ce6 positive cells were observed for the lower and higher concentrations respectively. Correspondingly, 14.8 ± 0.3 % and 24.8 ± 0.6 % siRNA transfection was observed for the two concentrations. No significant change was observed in the overall cellular uptake due to surface modification of Ce6-PSilQ NPs by siRNA coating.

siNeg-Ce6-PSilQ NPs was used as a negative control platform to account for any non-target specific effects of siRNA delivery. Gene silencing by sip62 was confirmed using quantitative RT-PCR and $\Delta\Delta C_q$ analysis. The relative p62 mRNA expression normalized to Ce6-PSilQ NPs show a significant difference for sip62-Ce6-PSilQ NPs (0.27 ± 0.03) compared to siNeg-Ce6-PSilQ NPs (0.82 ± 0.10) (*$p<0.01$.) (**Figure 39b**) as an indication of the silencing of p62 gene and most likely p62/SQSTM1 protein.

The phototoxic effect on HT29 cells treated with sip62-Ce6-PSilQ NPs was analyzed by MTS assay (**Figure 39c**) under light irradiation (633 nm, 25 mW/cm^2, 20 min). The IC_{50} values determined from the concentration-response curve for the sip62-Ce6-PSilQ, siNeg-Ce6-PSilQ and Ce6-PSilQ NPs are 10.3 ± 0.4 µM, 11.3 ± 0.5 µM and 12.8 ± 0.7 µM [Ce6], respectively. A trend is observed in these IC_{50} values with the following increased order of phototoxicity sip62-Ce6-

PSilQ > siNeg-Ce6-PSilQ > Ce6-PSilQ NPs; nevertheless, no significant difference was found between the IC_{50} values.

The analysis of the cell death mechanisms shows that sip62- and siNeg-Ce6-PSilQ NPs afforded 26.3 ± 0.1 % and 25.6 ± 0.7 % of Annexin-V-positive cells with concentrations of at 2.4 μM [Ce6] and 9.6 nM [siRNA] in the presence of light (633 nm, 25 mW/cm^2, 20 min) (**Figure 39d**). At higher concentrations, 4.8 μM [Ce6] and 19.2 nM [siRNA], sip62- and siNeg-Ce6-PSilQ NPs produced 37.4 ± 0.1 % and 35.0 ± 2.6 %of Annexin-V-positive cells, respectively. No significant change in apoptosis was observed due to the combination of p62 silencing and PDT. The analysis of necrosis associated with the treatment using sip62- and siNeg-Ce6-PSilQ NP afforded 5.6 ± 0.1 % and 2.6 ± 0.2 % of necrotic-positive cells, respectively at concentrations of 2.4 μM [Ce6] and 9.6 nM [siRNA]. At the higher concentrations, 4.8 μM [Ce6] and 19.2 nM [siRNA], sip62- and siNeg-Ce6-PSilQ NPs produced 17.8 ± 0.1 % and 11.5 ± 2.2 % of necrotic-positive cells. In this case, a trend on slightly higher amount of necrotic cells was found for the treatments with sip62-Ce6-PSilQ NPs (* $p<0.05$, ** $p< 0.01$.).

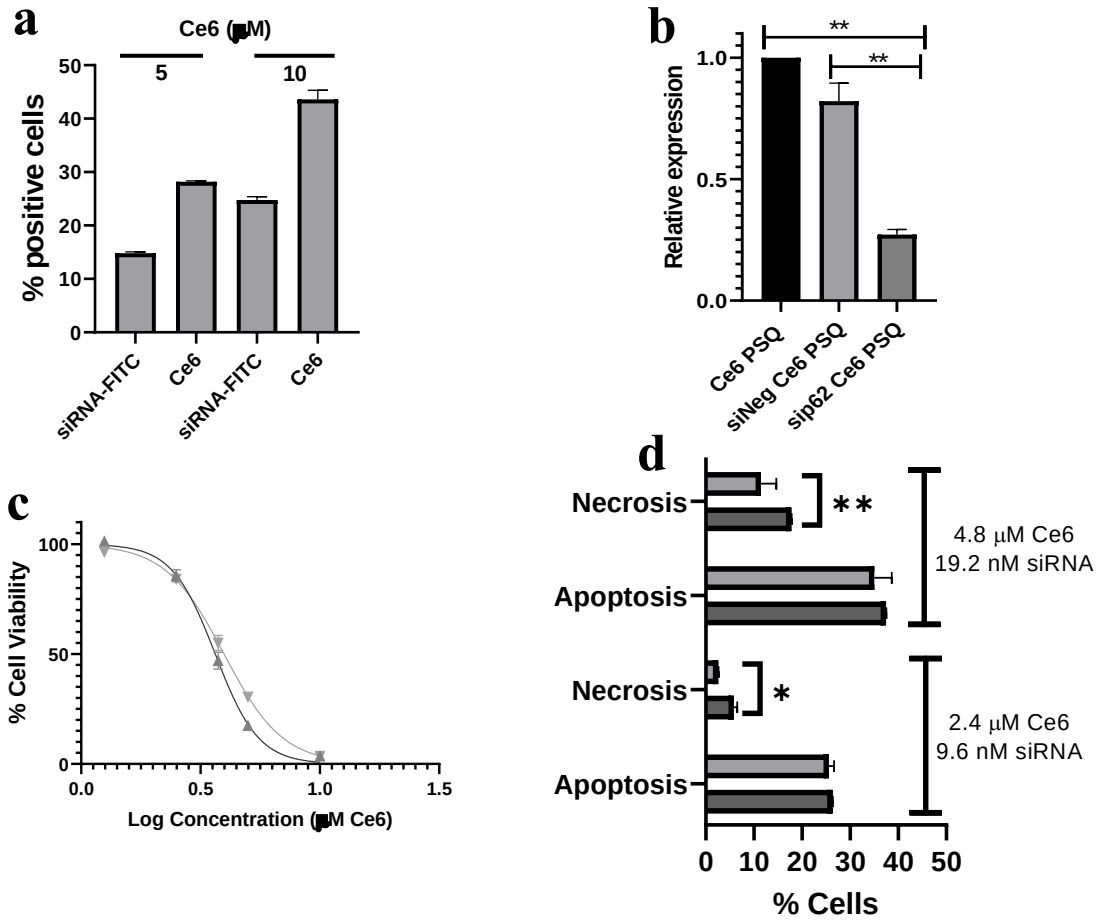

Figure 38. a) Cellular uptake of sip62-Ce6-PSilQ NPs in HT29 cells recorded in siRNA (FITC) and Ce6 (red) channels b) Silencing of p62 gene in HT29 cells after treatment with Ce6-PSilQ NPs (black), siNeg-Ce6-PSilQ NPs (light grey), and sip62-Ce6-PSilQ NPs (dark grey). c) Phototoxicity of siNeg-Ce6-PSilQ NPs (down triangles, light grey), and sip62-Ce6-PSilQ NPs (up triangles, dark grey) in HT29 cells. d) Apoptosis/necrosis analysis of HT29 cells treated with siNeg-Ce6-PSilQ NPs (horizontal bars, light grey) and sip62-Ce6-PSilQ NPs (dark grey) at different concentrations. Data are represented as mean ± SD. Statistics: two-way ANOVA using Tukey's multiple comparison test: *** $p \leq 0.001$, ** $p \leq 0.01$, * $p \leq 0.05$, and ns: $p > 0.05$.

4.3.7. Discussion

Photodynamic therapy triggers different type of cell death mechanisms with the most common being apoptosis and necrosis [102]. In addition to cancer cell death induced by PDT, intrinsic detoxification mechanisms to combat photooxidative stress are also activated. One such adaptive

response to PDT mediated extrinsic stress is autophagy [279]. The high reactivity of photogenerated ROS leads to selective autophagy to remove oxidatively damaged organelles and biomolecules [280]. Alternately, HIF-1α is another key player and, despite conferring adaptability to hypoxia which might lead to PDT resistance by promoting expression of the vacuole membrane protein 1 (VMP1), a protein capable of inducing the formation of autophagosomes [281]. Autophagy was found to protect PDT treated cells from oxidative damage triggered by various PSs like 5-ALA, hypercin, PhotofrinTM, protoporphyrin IX, TPPOH-SNPs and verteporfin [117]. Protective autophagy can be repressed through pharmacological agents such as Bafilomycin-A1, Chloroquine, 3-Methyladenine or Wortmannin and genetic intervention targeting autophagy elated genes such as ATG3, ATG5 or Beclin-1 and regulators like CHOP, as a combination strategy to quell PDT-resistance in tumor cells [109]. Although, there are some reports supporting autophagy associated cell death in PDT, in this account we are focused on investigating outcomes of nanoparticle mediated combination therapy involving PDT and negative regulation of autophagy using. The complexity of autophagy and numerous steps allows for several possibilities of therapeutic intervention. Two such approaches have been explained in this study, firstly using Dp44mT Ce6 PSilQ NPs and second using sip62 Ce6 PSilQ NPs.

In this study, we synthesized Ce6-PSilQ nanoparticles starting with the synthesis “in situ” of Ce6-silane precursor that is subsequently condensed into nanoparticles in a base catalyzed reverse microemulsion system. The nanoparticles obtained were spherical and with a diameter of 42.3 ± 7.1 nm. As reported previously, PSilQ nanomaterials are distinguished for reaching a high loading capacity of the therapeutic agent [273, 282]. In this case, the loading of Ce6 to PSilQ nanoparticles was determined to be 17.0 ± 4.0 %wt. There were no significant differences found in size, morphology and overall cargo loading capacity between Ce6 PSilQ and Dp44mT Ce6 PSilQ NPs.

Dp44mT values. The reduced absorption efficiency of Ce6 molecules immobilized in Ce6 PSilQ NPs compared to free solvated Ce6 directly impacts singlet oxygen production. This phenomenon was noticed for several conjugated forms of Ce6, and other PSs reported by others and our group [283, 284]. The presence of amine groups on the surface of Ce6 PSilQ NPs and Dp44mT Ce6 PSilQ NPs offers flexibility for surface modification using polyethylene glycol (PEG) and other targeting antibodies to increase specificity for in vivo applications.

We evaluated the in vitro properties of the Ce6-PSilQ nanoparticles in a human colorectal cancer (HT29) cell line. Several studies have showed promising results supporting the efficacy of PDT to treat colon cancer as an adjuvant therapy at different stages of the disease [285]. Flow cytometry and confocal microscopy showed that HT29 cells internalized the nanoparticles effectively (> 30% at 17 μg/mL) because of the positive surface charge imparted by amine groups. The partial co-localization of Ce6-PSilQ NPs in the lysosomes of HT29 cells can be seen from the overlapping fluorescence of Ce6 (red) and Lysotracker green in the confocal microscopy images (Figure 35). Cell internalization of PSilQ nanoparticles through the endosomal pathway has already been reported by our group [233].

The phototoxic performance of Ce6-PSilQ NPs in HT29 cells showed the typical dose-response associated to PDT (Figure 37b). In comparison with the parent PS agent; the phototoxicity of the Ce6-PSilQ nanoparticles is reduced approx. 5-fold as seen in the IC50 value for Ce6(~2.6 μM) compared to the nanoparticles (12.8 ± 0.7 μM). The reduction of the PDT effect of PSs encapsulated in PSilQ NPs have been previously reported. This difference is explained by the self-quenching effect of closely packed PSs in the nanoparticles, which directly impacts the generation of $^1O_2$ [286]. Nevertheless, the encapsulation of PSs in PSilQ NPs has major advantages for the PDT application of this platform in vivo [287]. The production of $^1O_2$ by Ce6-PSilQ material was

demonstrated in solution (Figure 34d). To confirm that other ROS are involved in the PDT effect in vitro, we used DCFH-DA to measure the presence of ROS such as hydroxyl, peroxyl radicals and hydrogen peroxide in HT29 cells. Flow cytometry data show that Ce6-PSilQ NPs generated 1.5-fold higher number of DCF-positive cells than the parent Ce6. The phototoxicity of Ce6 has been mainly related to the generation of $^1O_2$ and its localization in specific organelles [288]. Therefore, our results of higher generation of type I ROS by the Ce6-PSilQ NPs not necessarily implied better phototoxicity as we observed in Figure 4a. The analysis of the apoptosis and necrosis triggered by Ce6-PSilQ NPs and Ce6 show interesting differences in their cell death mechanism. Ce6 produced 4- and 3-fold higher number of apoptotic and necrotic cells, respectively than Ce6-PSilQ NPs ($p<0.0001$). It has been reported that Ce6 generates more necrotic cells at higher concentrations when cell membrane and partial lysosomal localization occurs [289, 290]. The direct impact of PDT generated ROS on mitochondria and subsequent release of cytochrome c is reported as the major checkpoint controlling the induction of apoptosis [291]. Additionally, permeabilization of lysosomes has shown to initiate cell death by the release of cathepsins and other hydrolases into the cytosol [292]. Cell death by LMP might assume either apoptotic or necrotic mechanisms depending on the occurrence of caspase activation. There was little to no apoptosis or necrosis observed in dark controls.

Annexin V assay showed that Ce6-PSilQ NPs triggered a greater proportion of necrotic cell death (necrosis: total cell death) compared to the parent Ce6. The necrotic fractions in SYTOX Blue positive population for Ce6 PSQ NPs was 9% greater than the parent Ce6 (****$p<0.0001$). This can be attributed to major lysosomal sub-localization of Ce6-PSilQ NPs and resultant LMP dependent cell death caused by ROS post irradiation.

Autophagy is described as a catabolic mechanism characterized by vesicles engulfing dysfunctional cellular components for degradation and recycling in lysosomes [112]. Autophagy is often observed as a consequence of excess intracellular ROS or oxidative stress. High autophagy flux implies a rapid rate of recycling of carbonylated proteins and damaged organelles after PDT [280]. Previous reports have shown that premature termination of active autophagy enhanced toxic effect of ROS in cancer cells [293]. In this work, we used Ce6-PSilQ NPs as a carrier to evaluate two different strategies that targets autophagy and are combined with PDT to eliminate cancer cells. First, we used a thiosemicarbazone-based autophagy inhibitor (Dp44mT), which one of its main consequences is to directly target the formation of autolysosome by preventing the fusion of lysosomes with autophagosomes. To account for that effect, we used a commercially available tandem sensor (PremoTM Tandem Autophagy sensor RFP-GFP-LC3 kit) that has the ability to monitor the various stages of autophagy through LC3B protein localization [294]. The sensor is a baculoviral construct that encodes an acid sensitive GFP with an acid insensitive RFP. The changes in pH due to the fusion of autophagosomes (neutral pH) with lysosomes (acidic pH) can be visualized by quantifying the loss of GFP as compared to RFP fluorescence intensity (autophagy flux) [295, 296]. In this study; as parameter for quantification, we measured the ratio of red to green mean fluorescence intensity of the transduced samples after PDT treatment using flow cytometry. The autophagy flux of HT29 cells treated with Ce6-PSilQ NPs was reduced by 47 % after treatment with Dp44mT-Ce6-PSilQ NPs as an indication of the inhibiting effect of Dp44mT on autophagy (**** $p \leq 0.0001$). More importantly, the PDT outcome of Dp44mT-Ce6-PSilQ NPs showed an increase of phototoxicity as demonstrated by the four-fold decrease in the IC50 value as compared to Ce6-PSilQ NPs alone. No cytotoxicity was observed in the absence of light with Ce6-PSilQ nor Dp44mT-Ce6-PSilQ NPs using the MTS assay [Figure 37b]. Apoptosis analysis

also provides confirmation on the enhancement of PDT effect due to the combined approach, Dp44mT-Ce6-PSilQ NPs afforded 3.5-fold more apoptotic-positive cells than Ce6-PSilQ NPs. A similar trend was observed for the free drugs. Necrosis analysis show a two-fold increase on the number of necrotic-positive cells associated with Dp44mT-Ce6-PSilQ NPs in comparison with Ce6-PSilQ NPs. Interestingly, the control MTS experiments for the free drugs, Ce6 and mixture Dp44mT/Ce6, resulted in high toxicity in the absence of light for the mixture. It is well-known that Dp44mT assumes a dual role through autophagosome initiation by excess ROS production in an iron-dependent manner in the lysosomes, which could induce cytotoxicity, and the inhibition of late-stage autophagy by lysosomal membrane permeabilization (LMP) [276] [297] [298]. The generation of ROS under dark conditions for the mixture Dp44mT/Ce6 was corroborated by our own experiments. Nevertheless, the ROS-positive cells were reduced 5-fold for the Dp44mT-Ce6-PSilQ NPs as an indication that the encapsulation of Dp44mT in the PSilQ platform reduces its generation of ROS, but the inhibitor has still enough capacity to afford the LMP to block autophagy post PDT. However, the absence of distinct autophagic vacuoles in Dp44mT Ce6 PSilQ treated cells indicates negative regulation of autophagy by presumably by more than one mechanism. These results validate that using PSilQ NPs to carry autophagy inhibitors improve the overall PDT effect.

Our second approach to inhibit the autophagy mechanism targets the p62/SQSTM1 autophagosome cargo protein by using siRNA. The sip62-Ce6-PSilQ NPs efficiently reduced the expression of p62 gene in HT29 cells (Figure 4a). Nevertheless, this silencing effect was not fully reflected in the phototherapeutic outcome of sip62-Ce6-PSilQ NPs against HT29 cells (Figure 4b). Only a minimal reduction in the IC_{50} values was observed for this material compared with the control experiments. The apoptosis analysis did not show much difference either (Figure 4c). This

can be explained by compensatory mechanisms in autophagy where cells recruit other autophagosome specific receptors like NBR1, NDP52 for binding and subsequent sequestration of PDT induced poly-ubiquitinated products of oxidation into autophagosomes for degradation upon fusion with lysosomes. Similar results were reported for shRNA-mediated knockdown of ATG5, which only partially blocked autophagic response resulting in a marginal improvement of Hela and MCF-7 cells sensitivity to PDT [276]. Interestingly, inhibition of p62 revealed a relatively higher fraction ($p<0.05$) of non-apoptotic cell death which aligns with observations by other groups where sip62 increased non-apoptotic cell death in multiple carcinoma cells in a siRNA concentration dependent manner [299].

4.4. Conclusion

The use of nanoparticulate-based platforms as codelivery system to enhance the PDT effect against cancer is a burgeoning field in nanomedicine. Herein, we designed, synthesized and characterized a PSilQ nanoparticles to carry Ce6 as PS agent and an autophagy inhibitor agent. We independently targeted the autophagy pathway at two different stages: early-stage using sip62 or late-stage with Dp44mT. Our results show that despite the efficient silencing of the p62 gene, which is associated with the p62/SQSTM1 autophagosome cargo protein, the final phototherapeutic outcome produced by sip62-Ce6-PSilQ NPs was not statistically different from the control experiments. The lack of additive effect is most likely due compensatory mechanisms in autophagy to overcome the effect of PDT. Recent reports have shown that complete knockout ATG5 utilizing CRISPR/Cas9 genome in HeLa cells resulted in a significant increase of PDT-mediated toxicity. This is a strategy worthy to explore in the future. Our second approach, which relies on Dp44mT-Ce6-PSilQ NPs that targets the late-stage of the autophagy mechanism, produced an additive interaction between Ce6 and Dp44mT. Our results for the autophagy flux, phototoxicity, and apoptosis/necrosis analysis demonstrated that Dp44mT-Ce6-PSilQ NPs efficiently eliminated

HT29 cells with the combine performance of the photosensitizer and the autophagy inhibitor. It is also important to point out that the encapsulation of the Dp44mT molecule inside the PSilQ platform reduced its cytotoxic effect related to ROS generation without decreasing its inhibitory capability. Overall, our study demonstrated that the use of multifunctional PSilQ system for the codelivery of PS agent and autophagy inhibitor enhances the photodynamic therapy against cancer cells. We envision that this approach can be combined with other therapies such as chemotherapy immunotherapy or photothermal therapy to further improve the use of PDT for the treatment of cancer.

4.5. Appendix - Autophagy regulation using Multimodal Chlorin e6-loaded Polysilsesquioxane Nanoparticles to Improve Photodynamic Therapy

Table 3 Physicochemical properties of Ce6 PSilQ NPs

	Z_{avg} (nm)	PDI	Zeta (mV)	NH_2 (nmol/ mg)
Ce6 PSilQ	324.2 ± 2.9	0.17 ± 0.02	+ 20.9 ± 0.4	1876 ± 234
Dp44mT Ce6 PSilQ	376.1 ± 7.6	0.22 ± 0.02	+ 21.8 ± 0.5	NA

Table 4. Combination indices of Ce6 and Dp44mT at various ratios

Ratio Dp44mT:Ce6 (µM:µM)	Ce6 (IC-50 µM)	Dp44mT (IC-50 µM)	Combination Index
0.0375	2.486	0.016	1.124
0.1	1.115	0.021	0.647
0.225	0.696	0.034	0.620
0.6	0.221	0.055	0.652
Dp44mT	-	0.097	
Ce6	2.590		

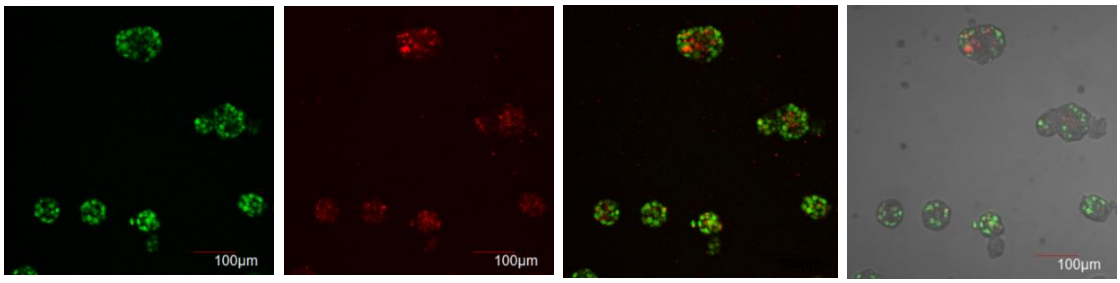

siNeg-FITC Ce6 Overlay Merge

Figure 39. Cellular uptake of siNeg^{FITC} Ce6 PSilQ NPs

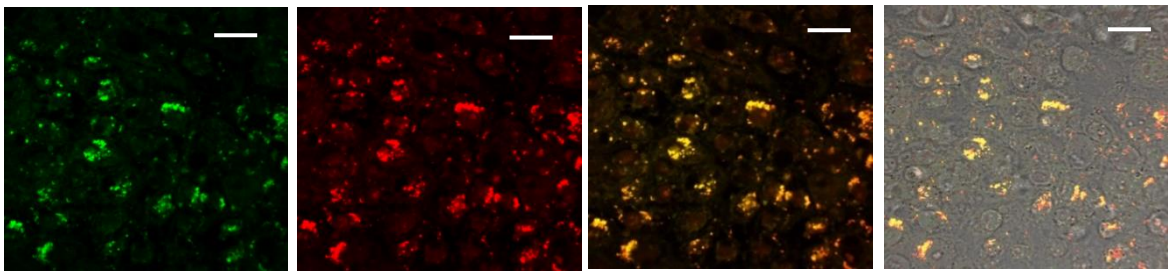

Figure 40 Confocal image of Autophagy flux observed in Ce6 PSilQ NPs after irradiation (Scale bar= 20 µm)

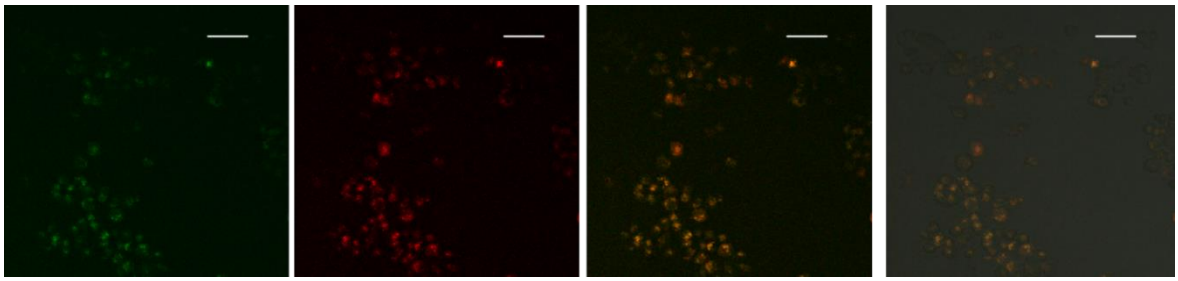

Figure 41 Confocal image of Autophagy flux observed in Dp44mT Ce6 PSilQ NPs after irradiation (Scale bar = 40 µm)

5. Conclusions and Future directions

5.1. Conclusions

Chapters 2-4 present the development of three silica-based nanoparticles (SiNPs) using a template aided and base catalyzed process. The two platforms, MSNP and PSilQ NPs were biocompatible and demonstrated safe intracellular delivery of drugs (DOX, Ce6 or Dp44mT). In addition, the particles were amenable to surface modification for loading nucleic acids that afford gene regulation. From a mechanistic standpoint, silica nanoparticles successfully induced RNAi to silence resistance causing genes while enabling cytotoxicity of loaded drugs (generation of toxic ROS or topoisomerase II inhibition). In this way, nanoparticles actuated multiple pathway intervention in diseased cells. Nanoparticles used for combination therapy depicted a different cellular behavior than equimolar physical mixtures of drugs did. It is conceivable that the pharmacokinetics (PK) and pharmacodynamics (PD) of individual drugs that constitute combination therapies are asynchronous *in vivo*. This is a possible cause for the low success rate of combination therapies. Nanoparticles offer great potential for spatiotemporal systemic co-delivery of two (or more) therapeutic moieties that biologically interact to produce an enhanced therapeutic effect.

This thesis presents the development of silica-based nanoparticles to be used for the treatment of cancer using different therapeutic approaches either alone or combined. In particular, two silica-based platforms are utilized, mesoporous silica and polysilsesquioxane nanoparticles. The two platforms, MSNP and PSilQ NPs were biocompatible and demonstrated efficient intracellular delivery of drugs. In addition, the particles were amenable to surface modification for loading gene silencing moieties such as siRNA duplexes or nucleic acid nanoparticles (NANPs), hence demonstrating capability for multimodal therapy.

5.2. Future Work

5.2.1. Combination of Nucleic Acid and Mesoporous Silica Nanoparticles: Optimization and Therapeutic Performance In Vitro

To expand the therapeutic capability of Bcl2-fNA-DOX-MS-NP platform, its evaluation in multidrug resistant cancer cells or Bcl2 gene inserted cells is needed. This evaluation is necessary since wildtype MDA MB 231 and A375 cells tested, were significantly responsive to doxorubicin indicating that Bcl2 expression in the cells was not significant enough to prevent apoptosis through drug resistance.

Further, to test transient transfection capabilities of PEG-PEI-MS-NP platform, the combination with other therapeutic NANPs can be tested. Expanding the use of this platform to other combinations of chemotherapy and expression/silencing of target genes, which can be relevant to other types of cancer is envisioned. Finally, for future translation of this delivery system, scaling-up studies and evaluation in preclinical models is mandatory.

5.2.2. Light-Activated Protoporphyrin IX-Based Polysilsesquioxane Nanoparticles Induce Ferroptosis in Melanoma Cells

This chapter provided initial evidence that supported the occurrence of ferroptosis in PSilQ NPs mediated PDT. Although lipid peroxidation and glutathione peroxidase inactivation are primary characteristics of ferroptosis, evaluation of the actual products of lipid peroxidation will provide greater support to our findings. Therefore, the formation of malondialdehyde (MDA) as a product of PDT can be analyzed for PpIX PSilQ NPs and free PpIX [300].

To take advantage of the knowledge that ferroptosis is involve in PSilQ mediated PDT, ferroptosis inducers can be encapsulated by co-condensation in the PSilQ nanoparticles to explore their

synergistic effect, and potentially reduce concentrations of photosensitizers required for the treatment. Some interesting combinations to explore on this front could be ferroptosis promoter erastin and PpIX as a chemo-PDT combination therapy [301], and siGpx4 transfection along with PpIX as an siRNA-PDT combination therapy to yield therapeutic benefit [302].

5.2.3. Autophagy regulation using Multimodal Chlorin e6-loaded Polysilsesquioxane Nanoparticles to Improve Photodynamic Therapy

Our results revealed that targeting p62 for autophagy inhibition did not yield successful results in boosting PDT efficacy. The possibility that loss of p62 (knockout), but not inhibition (knockdown) of expression can yield better results can be investigated. This would require the creation of p62 knockout (KO) clones of HT29 and other colon cancer cells using CRISPR-Cas9 system and relevant guide RNA (gRNA). PDT performance of Ce6 PSilQ NPs in p62 KO cells compared to wildtype cells can be evaluated.

The hypothesis that inhibition of p62 is likely compensated by heightened expression of other autophagosome related proteins (NBR1) to sustain autophagy for survival or by protective pathways (UPS, antioxidant response) post PDT offers another direction of further studies [235].

6. References

1. Singh, R. and J.W. Lillard, Jr., *Nanoparticle-based targeted drug delivery.* Exp Mol Pathol, 2009. **86**(3): p. 215-23.
2. Vivero-Escoto, J.L., et al., *Mesoporous silica nanoparticles for intracellular controlled drug delivery.* Small, 2010. **6**(18): p. 1952-67.
3. Liberman, A., et al., *Synthesis and surface functionalization of silica nanoparticles for nanomedicine.* Surface science reports, 2014. **69**(2-3): p. 132-158.
4. Du, X., et al., *Mesoporous silica nanoparticles with organo-bridged silsesquioxane framework as innovative platforms for bioimaging and therapeutic agent delivery.* Biomaterials, 2016. **91**: p. 90-127.
5. Han, C., et al., *Formation Mechanism of Monodispersed Polysilsesquioxane Spheres in One-Step Sol–Gel Method.* Langmuir, 2021. **37**(19): p. 5878-5885.
6. Yang, B., Y. Chen, and J. Shi, *Mesoporous silica/organosilica nanoparticles: Synthesis, biological effect and biomedical application.* Materials Science and Engineering: R: Reports, 2019. **137**: p. 66-105.
7. Bora, R.S., et al., *RNA interference therapeutics for cancer: challenges and opportunities (review).* Mol Med Rep, 2012. **6**(1): p. 9-15.
8. Elbashir, S.M., et al., *Duplexes of 21-nucleotide RNAs mediate RNA interference in cultured mammalian cells.* Nature, 2001. **411**(6836): p. 494-498.
9. Zamore, P.D., et al., *RNAi: Double-Stranded RNA Directs the ATP-Dependent Cleavage of mRNA at 21 to 23 Nucleotide Intervals.* Cell, 2000. **101**(1): p. 25-33.
10. Wang, B., et al., *Distinct passenger strand and mRNA cleavage activities of human Argonaute proteins.* Nature structural & molecular biology, 2009. **16**: p. 1259-66.
11. Lam, J.K.W., et al., *siRNA Versus miRNA as Therapeutics for Gene Silencing.* Molecular therapy. Nucleic acids, 2015. **4**(9): p. e252-e252.
12. Strumberg, D., et al., *Phase I clinical development of Atu027, a siRNA formulation targeting PKN3 in patients with advanced solid tumors.* International journal of clinical pharmacology and therapeutics, 2012. **50**: p. 76-8.
13. Grzelinski, M., et al., *RNA interference-mediated gene silencing of pleiotrophin through polyethylenimine-complexed small interfering RNAs in vivo exerts antitumoral effects in glioblastoma xenografts.* Human gene therapy, 2006. **17**(7): p. 751-766.
14. Zhang, M.M., et al., *The growth of siRNA-based therapeutics: Updated clinical studies.* Biochem Pharmacol, 2021. **189**: p. 114432.
15. Pecot, C.V., et al., *RNA interference in the clinic: challenges and future directions.* Nat Rev Cancer, 2011. **11**(1): p. 59-67.
16. Giladi, H., et al., *Small interfering RNA inhibits hepatitis B virus replication in mice.* Mol Ther, 2003. **8**(5): p. 769-76.
17. Xia, H., et al., *RNAi suppresses polyglutamine-induced neurodegeneration in a model of spinocerebellar ataxia.* Nat Med, 2004. **10**(8): p. 816-20.
18. Santel, A., et al., *RNA interference in the mouse vascular endothelium by systemic administration of siRNA-lipoplexes for cancer therapy.* Gene Ther, 2006. **13**(18): p. 1360-70.
19. Landen, C.N., Jr., et al., *Therapeutic EphA2 gene targeting in vivo using neutral liposomal small interfering RNA delivery.* Cancer Res, 2005. **65**(15): p. 6910-8.
20. Chen, S., et al., *Advances with RNA interference in Alzheimer's disease research.* Drug design, development and therapy, 2013. **7**: p. 117-25.

21. Penn, J.S., et al., *Vascular endothelial growth factor in eye disease.* Progress in retinal and eye research, 2008. **27**(4): p. 331-371.
22. Alvarez, R., et al., *RNA interference-mediated silencing of the respiratory syncytial virus nucleocapsid defines a potent antiviral strategy.* Antimicrob Agents Chemother, 2009. **53**(9): p. 3952-62.
23. Mansoori, B., S. Sandoghchian Shotorbani, and B. Baradaran, *RNA interference and its role in cancer therapy.* Adv Pharm Bull, 2014. **4**(4): p. 313-21.
24. Pai, S.I., et al., *Prospects of RNA interference therapy for cancer.* Gene Therapy, 2006. **13**(6): p. 464-477.
25. Cai, J.J., et al., *5-aminolevulinic acid mediated photodynamic therapy inhibits survival activity and promotes apoptosis of A375 and A431 cells.* Photodiagnosis and Photodynamic Therapy, 2018. **21**: p. 257-262.
26. Zhang, M., et al., *Silencing the epidermal growth factor receptor gene with RNAi may be developed as a potential therapy for non small cell lung cancer.* Genetic vaccines and therapy, 2005. **3**: p. 5-5.
27. Liu, Q., et al., *A novel HER2 gene body enhancer contributes to HER2 expression.* Oncogene, 2018. **37**(5): p. 687-694.
28. Yang, G., et al., *Inhibition of Breast and Ovarian Tumor Growth through Multiple Signaling Pathways by Using Retrovirus-mediated Small Interfering RNA against Her-2/neu Gene Expression *.* Journal of Biological Chemistry, 2004. **279**(6): p. 4339-4345.
29. Li, S., et al., *Rapid Inhibition of Cancer Cell Growth Induced by Lentiviral Delivery and Expression of Mutant-Template Telomerase RNA and Anti-telomerase Short-Interfering RNA.* Cancer Research, 2004. **64**(14): p. 4833.
30. Butz, K., et al., *siRNA targeting of the viral E6 oncogene efficiently kills human papillomavirus-positive cancer cells.* Oncogene, 2003. **22**(38): p. 5938-5945.
31. Abedini, M.R., et al., *Possible role of FLICE-like inhibitory protein (FLIP) in chemoresistant ovarian cancer cells in vitro.* Oncogene, 2004. **23**(42): p. 6997-7004.
32. Zangemeister-Wittke, U., *Antisense to apoptosis inhibitors facilitates chemotherapy and TRAIL-induced death signaling.* Ann N Y Acad Sci, 2003. **1002**: p. 90-4.
33. Taniai, M., et al., *Mcl-1 Mediates Tumor Necrosis Factor-Related Apoptosis-Inducing Ligand Resistance in Human Cholangiocarcinoma Cells.* Cancer Research, 2004. **64**(10): p. 3517.
34. Kappler, M., et al., *Knockdown of survivin expression by small interfering RNA reduces the clonogenic survival of human sarcoma cell lines independently of p53.* Cancer Gene Ther, 2004. **11**(3): p. 186-93.
35. Schiffelers, R.M., et al., *Cancer siRNA therapy by tumor selective delivery with ligand-targeted sterically stabilized nanoparticle.* Nucleic acids research, 2004. **32**(19): p. e149-e149.
36. Liu, J., et al., *CEACAM1 inhibits cell-matrix adhesion and promotes cell migration through regulating the expression of N-cadherin.* Biochem Biophys Res Commun, 2013. **430**(2): p. 598-603.
37. Xiong, Z., et al., *Downregulation of heparanase by RNA interference inhibits invasion and tumorigenesis of hepatocellular cancer cells in vitro and in vivo.* Int J Oncol, 2012. **40**(5): p. 1601-9.
38. Lapteva, N., et al., *CXCR4 knockdown by small interfering RNA abrogates breast tumor growth in vivo.* Cancer Gene Therapy, 2005. **12**(1): p. 84-89.
39. Dawczynski, K., et al., *Elevated serum insulin-like growth factor binding protein-2 is associated with a high relapse risk after hematopoietic stem cell transplantation in childhood AML.* Bone Marrow Transplantation, 2006. **37**(6): p. 589-594.

40. Kim, J.H., et al., *Blocking the immunosuppressive axis with small interfering RNA targeting interleukin (IL)-10 receptor enhances dendritic cell-based vaccine potency.* Clin Exp Immunol, 2011. **165**(2): p. 180-9.
41. Lee, Y.K., et al., *Galectin-3 silencing inhibits epirubicin-induced ATP binding cassette transporters and activates the mitochondrial apoptosis pathway via β-catenin/GSK-3β modulation in colorectal carcinoma.* PLoS One, 2013. **8**(11): p. e82478.
42. Duan, Z., K.A. Brakora, and M.V. Seiden, *Inhibition of ABCB1 (MDR1) and ABCB4 (MDR3) expression by small interfering RNA and reversal of paclitaxel resistance in human ovarian cancer cells.* Mol Cancer Ther, 2004. **3**(7): p. 833-8.
43. Boccard, S.G., et al., *Inhibition of DNA-repair genes Ercc1 and Mgmt enhances temozolomide efficacy in gliomas treatment: a pre-clinical study.* Oncotarget, 2015. **6**(30): p. 29456-29468.
44. July, L.V., et al., *Nucleotide-based therapies targeting clusterin chemosensitize human lung adenocarcinoma cells both in vitro and <em>in vivo</em&gt.* Molecular Cancer Therapeutics, 2004. **3**(3): p. 223.
45. Gantier, M.P., et al., *Rational design of immunostimulatory siRNAs.* Molecular therapy : the journal of the American Society of Gene Therapy, 2010. **18**(4): p. 785-795.
46. Xin, Y., et al., *Nano-based delivery of RNAi in cancer therapy.* Molecular Cancer, 2017. **16**(1): p. 134.
47. Setten, R.L., J.J. Rossi, and S.P. Han, *The current state and future directions of RNAi-based therapeutics.* Nat Rev Drug Discov, 2019. **18**(6): p. 421-446.
48. Dorsett, Y. and T. Tuschl, *siRNAs: applications in functional genomics and potential as therapeutics.* Nature Reviews Drug Discovery, 2004. **3**(4): p. 318-329.
49. Choudhury, S.R., et al., *Viral vectors for therapy of neurologic diseases.* Neuropharmacology, 2017. **120**: p. 63-80.
50. Wang, J., Y. Zheng, and M. Zhao, *Exosome-Based Cancer Therapy: Implication for Targeting Cancer Stem Cells.* Frontiers in Pharmacology, 2017. **7**.
51. Foldvari, M., et al., *Non-viral gene therapy: Gains and challenges of non-invasive administration methods.* Journal of Controlled Release, 2016. **240**: p. 165-190.
52. Akinc, A., et al., *Exploring polyethylenimine-mediated DNA transfection and the proton sponge hypothesis.* The journal of gene medicine, 2005. **7**: p. 657-63.
53. Moghimi, S.M., et al., *A two-stage poly(ethylenimine)-mediated cytotoxicity: implications for gene transfer/therapy.* Molecular Therapy, 2005. **11**(6): p. 990-995.
54. Patil, M.L., M. Zhang, and T. Minko, *Multifunctional triblock Nanocarrier (PAMAM-PEG-PLL) for the efficient intracellular siRNA delivery and gene silencing.* ACS nano, 2011. **5**(3): p. 1877-1887.
55. Han, H.D., et al., *Targeted gene silencing using RGD-labeled chitosan nanoparticles.* Clin Cancer Res, 2010. **16**(15): p. 3910-22.
56. Ewert, K.K., et al., *Cationic Liposomes as Vectors for Nucleic Acid and Hydrophobic Drug Therapeutics.* Pharmaceutics, 2021. **13**(9): p. 1365.
57. Torrecilla, J., et al., *Silencing of hepatitis C virus replication by a non-viral vector based on solid lipid nanoparticles containing a shRNA targeted to the internal ribosome entry site (IRES).* Colloids Surf B Biointerfaces, 2016. **146**: p. 808-17.
58. Torrecilla, J., et al., *Lipid Nanoparticles as Carriers for RNAi against Viral Infections: Current Status and Future Perspectives.* BioMed Research International, 2014. **2014**: p. 161794.
59. Ursic-Bedoya, R., et al., *Protection against lethal Marburg virus infection mediated by lipid encapsulated small interfering RNA.* The Journal of infectious diseases, 2014. **209**(4): p. 562-570.
60. Geisbert, T.W., et al., *Postexposure protection of non-human primates against a lethal Ebola virus challenge with RNA interference: a proof-of-concept study.* Lancet (London, England), 2010. **375**(9729): p. 1896-1905.

61. Heidari, R., et al., *siRNA delivery using intelligent chitosan-capped mesoporous silica nanoparticles for overcoming multidrug resistance in malignant carcinoma cells.* Scientific Reports, 2021. **11**(1): p. 20531.
62. Slita, A., et al., *Characterization of modified mesoporous silica nanoparticles as vectors for siRNA delivery.* Asian Journal of Pharmaceutical Sciences, 2018. **13**(6): p. 592-599.
63. Wang, M., et al., *Endosomal escape kinetics of mesoporous silica-based system for efficient siRNA delivery.* Int J Pharm, 2013. **448**(1): p. 51-7.
64. Tatiparti, K., et al., *siRNA Delivery Strategies: A Comprehensive Review of Recent Developments.* Nanomaterials (Basel), 2017. **7**(4).
65. Li, X., et al., *A mesoporous silica nanoparticle – PEI – Fusogenic peptide system for siRNA delivery in cancer therapy.* Biomaterials, 2013. **34**(4): p. 1391-1401.
66. Ngamcherdtrakul, W., et al., *Cationic Polymer Modified Mesoporous Silica Nanoparticles for Targeted SiRNA Delivery to HER2+ Breast Cancer.* Adv Funct Mater, 2015. **25**(18): p. 2646-2659.
67. Morry, J., et al., *Targeted Treatment of Metastatic Breast Cancer by PLK1 siRNA Delivered by an Antioxidant Nanoparticle Platform.* Mol Cancer Ther, 2017. **16**(4): p. 763-772.
68. Elbakry, A., et al., *Layer-by-layer assembled gold nanoparticles for siRNA delivery.* Nano Lett, 2009. **9**(5): p. 2059-64.
69. Wang, J., et al., *siRNA Delivery Using Dithiocarbamate-Anchored Oligonucleotides on Gold Nanorods.* Bioconjugate Chemistry, 2019. **30**(2): p. 443-453.
70. Alvarez-Erviti, L., et al., *Delivery of siRNA to the mouse brain by systemic injection of targeted exosomes.* Nature Biotechnology, 2011. **29**(4): p. 341-345.
71. Xu, M., et al., *Engineered exosomes: desirable target-tracking characteristics for cerebrovascular and neurodegenerative disease therapies.* Theranostics, 2021. **11**(18): p. 8926-8944.
72. Zhang, D., et al., *Exosome-Mediated Small RNA Delivery: A Novel Therapeutic Approach for Inflammatory Lung Responses.* Molecular Therapy, 2018. **26**(9): p. 2119-2130.
73. Afonin, K.A., et al., *Triggering of RNA Interference with RNA-RNA, RNA-DNA, and DNA-RNA Nanoparticles.* Acs Nano, 2015. **9**(1): p. 251-259.
74. Afonin, K.A., et al., *Design and self-assembly of siRNA-functionalized RNA nanoparticles for use in automated nanomedicine.* Nature Protocols, 2011. **6**(12): p. 2022-2034.
75. Pi, F., et al., *RNA nanoparticles harboring annexin A2 aptamer can target ovarian cancer for tumor-specific doxorubicin delivery.* Nanomedicine: Nanotechnology, Biology and Medicine, 2017. **13**(3): p. 1183-1193.
76. Halman, J.R., et al., *Functionally-interdependent shape-switching nanoparticles with controllable properties.* Nucleic Acids Res, 2017.
77. Afonin, K.A., et al., *In silico design and enzymatic synthesis of functional RNA nanoparticles.* Accounts of Chemical Research, 2014. **47**(6): p. 1731-1741.
78. Bui, M.N., et al., *Versatile RNA tetra-U helix linking motif as a toolkit for nucleic acid nanotechnology.* Nanomedicine, 2017.
79. Monferrer, A., et al., *Versatile kit of robust nanoshapes self-assembling from RNA and DNA modules.* Nat Commun, 2019. **10**(1): p. 608.
80. Afonin, K.A., B. Lindsay, and B.A. Shapiro, *Engineered RNA Nanodesigns for Applications in RNA Nanotechnology.* DNA RNA Nanotechnol, 2015. **1**(1): p. 1-15.
81. Afonin, K.A., et al., *Co-transcriptional assembly of chemically modified RNA nanoparticles functionalized with siRNAs.* Nano Lett, 2012. **12**(10): p. 5192-5.
82. Guo, P., *The emerging field of RNA nanotechnology.* Nature nanotechnology, 2010. **5**(12): p. 833-842.
83. Grimm, D. and M.A. Kay, *Combinatorial RNAi: a winning strategy for the race against evolving targets?* Mol Ther, 2007. **15**(5): p. 878-88.

84. Grabow, W.W., et al., *Self-assembling RNA nanorings based on RNAI/II inverse kissing complexes.* Nano Lett, 2011. **11**(2): p. 878-87.
85. Bacellar, I.O., et al., *Photodynamic Efficiency: From Molecular Photochemistry to Cell Death.* Int J Mol Sci, 2015. **16**(9): p. 20523-59.
86. Kwiatkowski, S., et al., *Photodynamic therapy – mechanisms, photosensitizers and combinations.* Biomedicine & Pharmacotherapy, 2018. **106**: p. 1098-1107.
87. Prażmo, E., et al., *Photodynamic Therapy As a Promising Method Used in the Treatment of Oral Diseases.* Advances in Clinical and Experimental Medicine, 2016. **25**: p. 799-807.
88. Gunaydin, G., M.E. Gedik, and S. Ayan, *Photodynamic Therapy for the Treatment and Diagnosis of Cancer–A Review of the Current Clinical Status.* Frontiers in Chemistry, 2021. **9**.
89. Gheewala, T., T. Skwor, and G. Munirathinam, *Photosensitizers in prostate cancer therapy.* Oncotarget, 2017. **8**(18): p. 30524-30538.
90. Kwiatkowski, S., et al., *Photodynamic therapy - mechanisms, photosensitizers and combinations.* Biomed Pharmacother, 2018. **106**: p. 1098-1107.
91. Mallidi, S., et al., *Beyond the Barriers of Light Penetration: Strategies, Perspectives and Possibilities for Photodynamic Therapy.* Theranostics, 2016. **6**(13): p. 2458-2487.
92. Donohoe, C., et al., *Cell death in photodynamic therapy: From oxidative stress to anti-tumor immunity.* Biochimica et Biophysica Acta (BBA) - Reviews on Cancer, 2019. **1872**(2): p. 188308.
93. Dai, L., et al., *Serum 8-hydroxydeoxyguanosine, a marker of oxidative DNA damage, is associated with mortality independent of inflammation in chronic kidney disease.* Eur J Intern Med, 2019. **68**: p. 60-65.
94. Dos Santos, A.F., et al., *Distinct photo-oxidation-induced cell death pathways lead to selective killing of human breast cancer cells.* Cell Death & Disease, 2020. **11**(12): p. 1070.
95. Yang, S. and G. Lian, *ROS and diseases: role in metabolism and energy supply.* Molecular and cellular biochemistry, 2020. **467**(1-2): p. 1-12.
96. Sachet, M., Y.Y. Liang, and R. Oehler, *The immune response to secondary necrotic cells.* Apoptosis : an international journal on programmed cell death, 2017. **22**(10): p. 1189-1204.
97. Lan, G., et al., *Nanoscale Metal-Organic Framework Overcomes Hypoxia for Photodynamic Therapy Primed Cancer Immunotherapy.* J Am Chem Soc, 2018. **140**(17): p. 5670-5673.
98. Mishchenko, T.A., et al., *Ferroptosis and Photodynamic Therapy Synergism: Enhancing Anticancer Treatment.* Trends Cancer, 2021. **7**(6): p. 484-487.
99. Wu, Y., et al., *Ferroptosis in Cancer Treatment: Another Way to Rome.* Frontiers in oncology, 2020. **10**: p. 571127-571127.
100. Oliveira, C.S., et al., *Major determinants of photoinduced cell death: Subcellular localization versus photosensitization efficiency.* Free Radical Biology and Medicine, 2011. **51**(4): p. 824-833.
101. Peskova, N.N., et al., *The localization of the photosensitizer determines the dynamics of the secondary production of hydrogen peroxide in cell cytoplasm and mitochondria.* Journal of Photochemistry and Photobiology B: Biology, 2021. **219**: p. 112208.
102. Mokoena, D.R., B.P. George, and H. Abrahamse, *Photodynamic Therapy Induced Cell Death Mechanisms in Breast Cancer.* International journal of molecular sciences, 2021. **22**(19): p. 10506.
103. Turubanova, V.D., et al., *Immunogenic cell death induced by a new photodynamic therapy based on photosens and photodithazine.* Journal for ImmunoTherapy of Cancer, 2019. **7**(1): p. 350.
104. Broekgaarden, M., et al., *Tumor cell survival pathways activated by photodynamic therapy: a molecular basis for pharmacological inhibition strategies.* Cancer metastasis reviews, 2015. **34**(4): p. 643-690.
105. Klaassen, C.D. and S.A. Reisman, *Nrf2 the rescue: effects of the antioxidative/electrophilic response on the liver.* Toxicology and applied pharmacology, 2010. **244**(1): p. 57-65.

106. Åkerfelt, M., R.I. Morimoto, and L. Sistonen, *Heat shock factors: integrators of cell stress, development and lifespan.* Nature Reviews Molecular Cell Biology, 2010. **11**(8): p. 545-555.
107. Lee, A.-H., N.N. Iwakoshi, and L.H. Glimcher, *XBP-1 regulates a subset of endoplasmic reticulum resident chaperone genes in the unfolded protein response.* Molecular and cellular biology, 2003. **23**(21): p. 7448-7459.
108. Zhao, H., et al., *Blocking autophagy enhances the pro-apoptotic effect of bufalin on human gastric cancer cells through endoplasmic reticulum stress.* Biology Open, 2017. **6**(10): p. 1416-1422.
109. Dewaele, M., et al., *Autophagy pathways activated in response to PDT contribute to cell resistance against ROS damage.* J Cell Mol Med, 2011. **15**(6): p. 1402-14.
110. Rubinsztein, D.C. and R.A. Frake, *Yoshinori Ohsumi's Nobel Prize for mechanisms of autophagy: from basic yeast biology to therapeutic potential.* J R Coll Physicians Edinb, 2016. **46**(4): p. 228-233.
111. Filomeni, G., D. De Zio, and F. Cecconi, *Oxidative stress and autophagy: the clash between damage and metabolic needs.* Cell death and differentiation, 2015. **22**(3): p. 377-388.
112. Kocaturk, N.M. and D. Gozuacik, *Crosstalk Between Mammalian Autophagy and the Ubiquitin-Proteasome System.* Front Cell Dev Biol, 2018. **6**: p. 128.
113. Szokalska, A., et al., *Proteasome inhibition potentiates antitumor effects of photodynamic therapy in mice through induction of endoplasmic reticulum stress and unfolded protein response.* Cancer research, 2009. **69**(10): p. 4235-4243.
114. Levy, J.M.M., C.G. Towers, and A. Thorburn, *Targeting autophagy in cancer.* Nature Reviews Cancer, 2017. **17**(9): p. 528-542.
115. Koustas, E., et al., *Autophagy-related Proteins as a Prognostic Factor of Patients With Colorectal Cancer.* American journal of clinical oncology, 2019. **42**(10): p. 767-776.
116. Nakayama, S., et al., *p62/sequestosome 1 in human colorectal carcinoma as a potent prognostic predictor associated with cell proliferation.* Cancer medicine, 2017. **6**(6): p. 1264-1274.
117. Reiners, J.J., Jr., et al., *Assessing autophagy in the context of photodynamic therapy.* Autophagy, 2010. **6**(1): p. 7-18.
118. Garg, A.D., et al., *ROS-induced autophagy in cancer cells assists in evasion from determinants of immunogenic cell death.* Autophagy, 2013. **9**(9): p. 1292-307.
119. Domagala, A., et al., *Inhibition of autophagy sensitizes cancer cells to Photofrin-based photodynamic therapy.* BMC Cancer, 2018. **18**(1): p. 210.
120. Levy, J.M.M., et al., *Autophagy Inhibition Improves Chemosensitivity in BRAF^{V600E} Brain Tumors.* Cancer Discovery, 2014. **4**(7): p. 773.
121. Classen, F., et al., *Autophagy induced by ionizing radiation promotes cell death over survival in human colorectal cancer cells.* Experimental Cell Research, 2019. **374**(1): p. 29-37.
122. Gunaydin, G., M.E. Gedik, and S. Ayan, *Photodynamic Therapy—Current Limitations and Novel Approaches.* Frontiers in Chemistry, 2021. **9**.
123. Lin, L., et al., *Nano-photosensitizers for enhanced photodynamic therapy.* Photodiagnosis and Photodynamic Therapy, 2021. **36**: p. 102597.
124. Abrahamse, H. and M.R. Hamblin, *New photosensitizers for photodynamic therapy.* The Biochemical journal, 2016. **473**(4): p. 347-364.
125. Debele, T.A., S. Peng, and H.-C. Tsai, *Drug Carrier for Photodynamic Cancer Therapy.* International journal of molecular sciences, 2015. **16**(9): p. 22094-22136.
126. Qin, M., et al., *Methylene blue covalently loaded polyacrylamide nanoparticles for enhanced tumor-targeted photodynamic therapy.* Photochemical & photobiological sciences : Official journal of the European Photochemistry Association and the European Society for Photobiology, 2011. **10**: p. 832-41.

127. Matthew Peterson, C., et al., *Combination Chemotherapy and Photodynamic Therapy with N-(2-Hydroxypropyl)methacrylamide Copolymer-bound Anticancer Drugs Inhibit Human Ovarian Carcinoma Heterotransplanted in Nude Mice.* Cancer Research, 1996. **56**(17): p. 3980.
128. Hong, S.H. and Y. Choi, *Mesoporous silica-based nanoplatforms for the delivery of photodynamic therapy agents.* Journal of pharmaceutical investigation, 2018. **48**(1): p. 3-17.
129. Vines, J.B., et al., *Gold Nanoparticles for Photothermal Cancer Therapy.* Frontiers in Chemistry, 2019. **7**.
130. Bouramtane, S., et al., *Porphyrin-xylan-coated silica nanoparticles for anticancer photodynamic therapy.* Carbohydrate Polymers, 2019. **213**: p. 168-175.
131. Lin, C.-H., et al., *Hydrophobicity-Tuned Periodic Mesoporous Organo-Silica Nanoparticles for Photodynamic Therapy.* International Journal of Molecular Sciences, 2020. **21**(7).
132. Hone, D., et al., *Generation of Cytotoxic Singlet Oxygen via Phthalocyanine-Stabilized Gold Nanoparticles: A Potential Delivery Vehicle for Photodynamic Therapy.* Langmuir, 2002. **18**: p. 2985-2987.
133. Oo, M., et al., *5-Aminolevulinic acid-conjugated gold nanoparticles for photodynamic therapy of cancer.* Nanomedicine (London, England), 2009. **3**: p. 777-86.
134. Deng, K., et al., *Recent Progress in Near Infrared Light Triggered Photodynamic Therapy.* Small, 2017. **13**(44): p. 1702299.
135. Chen, G., et al., *Upconversion Nanoparticles: Design, Nanochemistry, and Applications in Theranostics.* Chemical Reviews, 2014. **114**(10): p. 5161-5214.
136. Wang, C., L. Cheng, and Z. Liu, *Upconversion nanoparticles for photodynamic therapy and other cancer therapeutics.* Theranostics, 2013. **3**(5): p. 317-30.
137. Feng, Y., et al., *Assembly of upconversion nanophotosensitizer in vivo to achieve scatheless real-time imaging and selective photodynamic therapy.* Biomaterials, 2019. **201**.
138. Lee, S.Y., et al., *Near-Infrared Light-Triggered Photodynamic Therapy and Apoptosis Using Upconversion Nanoparticles With Dual Photosensitizers.* Frontiers in bioengineering and biotechnology, 2020. **8**: p. 275-275.
139. Ai, F., et al., *A core-shell-shell nanoplatform upconverting near-infrared light at 808 nm for luminescence imaging and photodynamic therapy of cancer.* Scientific Reports, 2015. **5**(1): p. 10785.
140. Lee, S.Y., et al., *Near-Infrared Light-Triggered Photodynamic Therapy and Apoptosis Using Upconversion Nanoparticles With Dual Photosensitizers.* Frontiers in Bioengineering and Biotechnology, 2020. **8**.
141. Subhan, M.A., et al., *Recent Advances in Tumor Targeting via EPR Effect for Cancer Treatment.* Journal of Personalized Medicine, 2021. **11**(6): p. 571.
142. Rosenblum, D., et al., *Progress and challenges towards targeted delivery of cancer therapeutics.* Nature Communications, 2018. **9**(1): p. 1410.
143. Chen, Z., et al., *Zinc phthalocyanine conjugated with the amino-terminal fragment of urokinase for tumor-targeting photodynamic therapy.* Acta Biomater, 2014. **10**(10): p. 4257-68.
144. Stuchinskaya, T., et al., *Targeted photodynamic therapy of breast cancer cells using antibody-phthalocyanine-gold nanoparticle conjugates.* Photochem Photobiol Sci, 2011. **10**(5): p. 822-31.
145. Bharathiraja, S., et al., *Chlorin e6 conjugated silica nanoparticles for targeted and effective photodynamic therapy.* Photodiagnosis Photodyn Ther, 2017. **19**: p. 212-220.
146. Bayat Mokhtari, R., et al., *Combination therapy in combating cancer.* Oncotarget, 2017. **8**(23): p. 38022-38043.
147. Palanikumar, L., et al., *Spatiotemporally and Sequentially-Controlled Drug Release from Polymer Gatekeeper–Hollow Silica Nanoparticles.* Scientific Reports, 2017. **7**(1): p. 46540.

148. Zhang, R.X., et al., *Nanomedicine of synergistic drug combinations for cancer therapy - Strategies and perspectives.* Journal of controlled release : official journal of the Controlled Release Society, 2016. **240**: p. 489-503.
149. Mayer, L.D., P. Tardi, and A.C. Louie, *CPX-351: a nanoscale liposomal co-formulation of daunorubicin and cytarabine with unique biodistribution and tumor cell uptake properties.* Int J Nanomedicine, 2019. **14**: p. 3819-3830.
150. Tardi, P.G., et al., *Drug ratio-dependent antitumor activity of irinotecan and cisplatin combinations in vitro and in vivo.* Mol Cancer Ther, 2009. **8**(8): p. 2266-75.
151. Albain, K.S., et al., *Gemcitabine plus Paclitaxel versus Paclitaxel monotherapy in patients with metastatic breast cancer and prior anthracycline treatment.* J Clin Oncol, 2008. **26**(24): p. 3950-7.
152. Meng, H., et al., *Use of a lipid-coated mesoporous silica nanoparticle platform for synergistic gemcitabine and paclitaxel delivery to human pancreatic cancer in mice.* ACS Nano, 2015. **9**(4): p. 3540-57.
153. Cheng, Z., et al., *Nanomaterials for cancer therapy: current progress and perspectives.* Journal of Hematology & Oncology, 2021. **14**(1): p. 85.
154. Darvishi, B., L. Farahmand, and A.K. Majidzadeh, *Stimuli-Responsive Mesoporous Silica NPs as Non-viral Dual siRNA/Chemotherapy Carriers for Triple Negative Breast Cancer.* Mol Ther Nucleic Acids, 2017. **7**: p. 164-180.
155. Martinelli, C. and M. Biglietti, *Nanotechnological approaches for counteracting multidrug resistance in cancer.* Cancer Drug Resistance, 2020. **3**(4): p. 1003-1020.
156. Wang, Y., et al., *Co-delivery of drugs and DNA from cationic core-shell nanoparticles self-assembled from a biodegradable copolymer.* Nat Mater, 2006. **5**(10): p. 791-6.
157. Hu, Q., et al., *Co-Delivery of Paclitaxel and Interleukin-12 Regulating Tumor Microenvironment for Cancer Immunochemotherapy.* Adv Healthc Mater, 2020. **9**(10): p. e1901858.
158. Kwon, S.S., et al., *Cell penetrating peptide conjugated liposomes as transdermal delivery system of Polygonum aviculare L. extract.* Int J Pharm, 2015. **483**(1-2): p. 26-37.
159. Pishavar, E., M. Ramezani, and M. Hashemi, *Co-delivery of doxorubicin and TRAIL plasmid by modified PAMAM dendrimer in colon cancer cells, in vitro and in vivo evaluation.* Drug Development and Industrial Pharmacy, 2019. **45**(12): p. 1931-1939.
160. Zhou, Y., et al., *Mesoporous silica nanoparticles for drug and gene delivery.* Acta Pharmaceutica Sinica B, 2018. **8**(2): p. 165-177.
161. Zhou, X., et al., *Dual-Responsive Mesoporous Silica Nanoparticles Mediated Codelivery of Doxorubicin and Bcl-2 SiRNA for Targeted Treatment of Breast Cancer.* The Journal of Physical Chemistry C, 2016. **120**(39): p. 22375-22387.
162. Meng, H., et al., *Codelivery of an optimal drug/siRNA combination using mesoporous silica nanoparticles to overcome drug resistance in breast cancer in vitro and in vivo.* ACS nano, 2013. **7**(2): p. 994-1005.
163. Spring, B.Q., et al., *The role of photodynamic therapy in overcoming cancer drug resistance.* Photochemical & photobiological sciences : Official journal of the European Photochemistry Association and the European Society for Photobiology, 2015. **14**(8): p. 1476-1491.
164. Wang, T., et al., *Multifunctional hollow mesoporous silica nanocages for cancer cell detection and the combined chemotherapy and photodynamic therapy.* ACS Appl Mater Interfaces, 2011. **3**(7): p. 2479-86.
165. Chang, J.E., et al., *Anticancer efficacy of photodynamic therapy with hematoporphyrin-modified, doxorubicin-loaded nanoparticles in liver cancer.* J Photochem Photobiol B, 2014. **140**: p. 49-56.

166. Juneja, R., et al., *Multimodal Polysilsesquioxane Nanoparticles for Combinatorial Therapy and Gene Delivery in Triple-Negative Breast Cancer.* ACS Appl Mater Interfaces, 2019. **11**(13): p. 12308-12320.
167. Zhang, W., et al., *Co-Delivery of Cisplatin Prodrug and Chlorin e6 by Mesoporous Silica Nanoparticles for Chemo-Photodynamic Combination Therapy to Combat Drug Resistance.* ACS Appl Mater Interfaces, 2016. **8**(21): p. 13332-40.
168. Bumcrot, D., et al., *RNAi therapeutics: a potential new class of pharmaceutical drugs.* Nat Chem Biol, 2006. **2**(12): p. 711-9.
169. Adams, D., et al., *Patisiran, an RNAi Therapeutic, for Hereditary Transthyretin Amyloidosis.* N Engl J Med, 2018. **379**(1): p. 11-21.
170. Chan, A., et al., *Preclinical Development of a Subcutaneous ALAS1 RNAi Therapeutic for Treatment of Hepatic Porphyrias Using Circulating RNA Quantification.* Mol Ther Nucleic Acids, 2015. **4**: p. e263.
171. Guo, P., *The emerging field of RNA nanotechnology.* Nat Nanotechnol, 2010. **5**(12): p. 833-42.
172. Seeman, N.C., *Nanomaterials based on DNA.* Annu Rev Biochem, 2010. **79**: p. 65-87.
173. Parlea, L., et al., *Cellular Delivery of RNA Nanoparticles.* ACS Comb Sci, 2016. **18**(9): p. 527-47.
174. Afonin, K.A., et al., *Computational and experimental characterization of RNA cubic nanoscaffolds.* Methods (San Diego, Calif.), 2014. **67**(2): p. 256-265.
175. Kireeva, M.L., et al., *Cotranscriptional Production of Chemically Modified RNA Nanoparticles.* Methods Mol Biol, 2017. **1632**: p. 91-105.
176. Afonin, K.A., et al., *In vitro assembly of cubic RNA-based scaffolds designed in silico.* Nature Nanotechnology, 2010. **5**(9): p. 676-682.
177. Johnson, M.B., et al., *Programmable Nucleic Acid Based Polygons with Controlled Neuroimmunomodulatory Properties for Predictive QSAR Modeling.* Small, 2017. **13**(42).
178. Rackley, L., et al., *RNA Fibers as Optimized Nanoscaffolds for siRNA Coordination and Reduced Immunological Recognition.* Adv Funct Mater, 2018. **28**(48): p. 1805959.
179. Ke, W., et al., *RNA-DNA fibers and polygons with controlled immunorecognition activate RNAi, FRET and transcriptional regulation of NF-kappaB in human cells.* Nucleic Acids Res, 2019. **47**(3): p. 1350-1361.
180. Chandler, M. and K.A. Afonin, *Smart-Responsive Nucleic Acid Nanoparticles (NANPs) with the Potential to Modulate Immune Behavior.* Nanomaterials (Basel), 2019. **9**(4).
181. Hong, E., et al., *Structure and Composition Define Immunorecognition of Nucleic Acid Nanoparticles.* Nano Lett, 2018. **18**(7): p. 4309-4321.
182. Hong, E., et al., *Toll-Like Receptor-Mediated Recognition of Nucleic Acid Nanoparticles (NANPs) in Human Primary Blood Cells.* Molecules, 2019. **24**(6).
183. Chandler, M., et al., *Innate immune responses triggered by nucleic acids inspire the design of immunomodulatory nucleic acid nanoparticles (NANPs).* Curr Opin Biotechnol, 2019. **63**: p. 8-15.
184. Khisamutdinov, E.F., et al., *Enhancing immunomodulation on innate immunity by shape transition among RNA triangle, square and pentagon nanovehicles.* Nucleic Acids Res, 2014. **42**(15): p. 9996-10004.
185. Guo, S., et al., *Tuning the size, shape and structure of RNA nanoparticles for favorable cancer targeting and immunostimulation.* Wiley Interdiscip Rev Nanomed Nanobiotechnol, 2020. **12**(1): p. e1582.
186. Roark, B.K., et al., *Fluorescence blinking as an output signal for biosensing.* ACS sensors, 2016. **1**(11): p. 1295-1300.
187. Alibakhshi, M.A., et al., *Picomolar Fingerprinting of Nucleic Acid Nanoparticles Using Solid-State Nanopores.* ACS Nano, 2017.

188. Goldsworthy, V., et al., *Fluorogenic RNA Aptamers: A Nano-platform for Fabrication of Simple and Combinatorial Logic Gates.* Nanomaterials (Basel), 2018. **8**(12).
189. Halman, J.R., et al., *A cationic amphiphilic co-polymer as a carrier of nucleic acid nanoparticles (Nanps) for controlled gene silencing, immunostimulation, and biodistribution.* Nanomedicine, 2020. **23**: p. 102094.
190. Cruz-Acuna, M., et al., *Magnetic nanoparticles loaded with functional RNA nanoparticles.* Nanoscale, 2018. **10**(37): p. 17761-17770.
191. Paris, J.L., A. Baeza, and M. Vallet-Regi, *Overcoming the stability, toxicity, and biodegradation challenges of tumor stimuli-responsive inorganic nanoparticles for delivery of cancer therapeutics.* Expert Opin Drug Deliv, 2019. **16**(10): p. 1095-1112.
192. Baeza, A., D. Ruiz-Molina, and M. Vallet-Regi, *Recent advances in porous nanoparticles for drug delivery in antitumoral applications: inorganic nanoparticles and nanoscale metal-organic frameworks.* Expert Opin Drug Deliv, 2017. **14**(6): p. 783-796.
193. Vivero-Escoto, J.L., R.C. Huxford-Phillips, and W. Lin, *Silica-based nanoprobes for biomedical imaging and theranostic applications.* Chem Soc Rev, 2012. **41**(7): p. 2673-85.
194. Croissant, J.G., Y. Fatieiev, and N.M. Khashab, *Degradability and Clearance of Silicon, Organosilica, Silsesquioxane, Silica Mixed Oxide, and Mesoporous Silica Nanoparticles.* Adv Mater, 2017. **29**(9).
195. Cha, W., et al., *Mesoporous Silica Nanoparticles as Carriers for Intracellular Delivery of Nucleic Acids and Subsequent Therapeutic Applications.* Molecules, 2017. **22**(5).
196. Castillo, R.R., A. Baeza, and M. Vallet-Regi, *Recent applications of the combination of mesoporous silica nanoparticles with nucleic acids: development of bioresponsive devices, carriers and sensors.* Biomater Sci, 2017. **5**(3): p. 353-377.
197. Pinese, C., et al., *Sustained delivery of siRNA/mesoporous silica nanoparticle complexes from nanofiber scaffolds for long-term gene silencing.* Acta Biomater, 2018. **76**: p. 164-177.
198. Vivero-Escoto, J.L., et al., *Nanoparticle mediated silencing of tenascin C in hepatic stellate cells: effect on inflammatory gene expression and cell migration.* J Mater Chem B, 2019. **7**(46): p. 7396-7405.
199. Shlyakhtenko, L.S., A.A. Gall, and Y.L. Lyubchenko, *Mica functionalization for imaging of DNA and protein-DNA complexes with atomic force microscopy.* Methods Mol Biol, 2013. **931**: p. 295-312.
200. Shlyakhtenko, L.S., et al., *Silatrane-based surface chemistry for immobilization of DNA, protein-DNA complexes and other biological materials.* Ultramicroscopy, 2003. **97**(1-4): p. 279-287.
201. Vivero-Escoto, J.L. and M. Elnagheeb, *Mesoporous Silica Nanoparticles Loaded with Cisplatin and Phthalocyanine for Combination Chemotherapy and Photodynamic Therapy in vitro.* Nanomaterials (Basel), 2015. **5**(4): p. 2302-2316.
202. Dreau, D., et al., *Mucin-1-Antibody-Conjugated Mesoporous Silica Nanoparticles for Selective Breast Cancer Detection in a Mucin-1 Transgenic Murine Mouse Model.* J Biomed Nanotechnol, 2016. **12**(12): p. 2172-2184.
203. Alvarez-Berrios, M.P. and J.L. Vivero-Escoto, *In vitro evaluation of folic acid-conjugated redox-responsive mesoporous silica nanoparticles for the delivery of cisplatin.* Int J Nanomedicine, 2016. **11**: p. 6251-6265.
204. Shen, J., et al., *Mesoporous silica nanoparticles loading doxorubicin reverse multidrug resistance: performance and mechanism.* Nanoscale, 2011. **3**(10): p. 4314-22.
205. Shahabi, S., et al., *Enhancing Cellular Uptake and Doxorubicin Delivery of Mesoporous Silica Nanoparticles via Surface Functionalization: Effects of Serum.* ACS Appl Mater Interfaces, 2015. **7**(48): p. 26880-91.

206. Meng, H., et al., *Engineered design of mesoporous silica nanoparticles to deliver doxorubicin and P-glycoprotein siRNA to overcome drug resistance in a cancer cell line.* ACS Nano, 2010. **4**(8): p. 4539-50.
207. Asadi, J., et al., *Enhanced imaging of lipid rich nanoparticles embedded in methylcellulose films for transmission electron microscopy using mixtures of heavy metals.* Micron, 2017. **99**: p. 40-48.
208. De Carlo, S. and J.R. Harris, *Negative staining and cryo-negative staining of macromolecules and viruses for TEM.* Micron, 2011. **42**(2): p. 117-31.
209. Kawasaki, T. and T. Kawai, *Toll-like receptor signaling pathways.* Front Immunol, 2014. **5**: p. 461.
210. Hu, Z., et al., *Anti-radiation damage effect of polyethylenimine as a toll-like receptor 5 targeted agonist.* J Radiat Res, 2013. **54**(2): p. 243-50.
211. Cubillos-Ruiz, J.R., et al., *Polyethylenimine-based siRNA nanocomplexes reprogram tumor-associated dendritic cells via TLR5 to elicit therapeutic antitumor immunity.* J Clin Invest, 2009. **119**(8): p. 2231-44.
212. Shishido, Y., et al., *Antitumor Effect of 5-Aminolevulinic Acid Through Ferroptosis in Esophageal Squamous Cell Carcinoma.* Annals of Surgical Oncology: p. 11.
213. Wang, J., et al., *More effective nanomedicines through particle design.* Small, 2011. **7**(14): p. 1919-31.
214. Walker, W.A., M. Tarannum, and J.L. Vivero-Escoto, *Cellular Endocytosis and Trafficking of Cholera Toxin B-Modified Mesoporous Silica Nanoparticles.* J Mater Chem B, 2016. **4**(7): p. 1254-1262.
215. Bharti, C., et al., *Mesoporous silica nanoparticles in target drug delivery system: A review.* Int J Pharm Investig, 2015. **5**(3): p. 124-33.
216. Xu, C., et al., *Photo-controlled release of paclitaxel and model drugs from RNA pyramids.* Nano research, 2019. **12**(1): p. 41-48.
217. Shu, Y., et al., *RNA-based micelles: A novel platform for paclitaxel loading and delivery.* Journal of Controlled Release, 2018. **276**: p. 17-29.
218. Shen, J., et al., *Engineering functional inorganic-organic hybrid systems: advances in siRNA therapeutics.* Chem Soc Rev, 2018. **47**(6): p. 1969-1995.
219. Pakunlu, R.I., et al., *Enhancement of the efficacy of chemotherapy for lung cancer by simultaneous suppression of multidrug resistance and antiapoptotic cellular defense: novel multicomponent delivery system.* Cancer Res, 2004. **64**(17): p. 6214-24.
220. Tabuchi, Y., et al., *Resistance to paclitaxel therapy is related with Bcl-2 expression through an estrogen receptor mediated pathway in breast cancer.* Int J Oncol, 2009. **34**(2): p. 313-9.
221. Deng, Z.J., et al., *Layer-by-layer nanoparticles for systemic codelivery of an anticancer drug and siRNA for potential triple-negative breast cancer treatment.* ACS Nano, 2013. **7**(11): p. 9571-84.
222. Chen, A.M., et al., *Co-delivery of doxorubicin and Bcl-2 siRNA by mesoporous silica nanoparticles enhances the efficacy of chemotherapy in multidrug-resistant cancer cells.* Small, 2009. **5**(23): p. 2673-7.
223. Pan, Q.S., et al., *In Situ Synthesis of Ultrathin ZIF-8 Film-Coated MSNs for Codelivering Bcl 2 siRNA and Doxorubicin to Enhance Chemotherapeutic Efficacy in Drug-Resistant Cancer Cells.* ACS Appl Mater Interfaces, 2018. **10**(39): p. 33070-33077.
224. Tekedereli, I., et al., *Therapeutic Silencing of Bcl-2 by Systemically Administered siRNA Nanotherapeutics Inhibits Tumor Growth by Autophagy and Apoptosis and Enhances the Efficacy of Chemotherapy in Orthotopic Xenograft Models of ER (-) and ER (+) Breast Cancer.* Mol Ther Nucleic Acids, 2013. **2**: p. e121.
225. Looi, C.Y., et al., *Induction of apoptosis in melanoma A375 cells by a chloroform fraction of Centratherum anthelminticum (L.) seeds involves NF-kappaB, p53 and Bcl-2-controlled mitochondrial signaling pathways.* BMC Complement Altern Med, 2013. **13**: p. 166.

226. Xu, Z.H., et al., *Colorimetric determination of polyamidoamine dendrimers and their derivates using a simple and rapid ninhydrin assay.* Analytical Letters, 2008. **41**(3): p. 444-455.
227. Shi, X., et al., *Recent advances in photodynamic therapy for cancer and infectious diseases.* Wiley Interdiscip Rev Nanomed Nanobiotechnol, 2019. **11**(5): p. e1560.
228. Obaid, G., et al., *Photonanomedicine: a convergence of photodynamic therapy and nanotechnology.* Nanoscale, 2016. **8**(25): p. 12471-503.
229. Alsaab, H.O., et al., *Progress in Clinical Trials of Photodynamic Therapy for Solid Tumors and the Role of Nanomedicine.* Cancers (Basel), 2020. **12**(10).
230. Vega, D.L., P. Lodge, and J.L. Vivero-Escoto, *Redox-Responsive Porphyrin-Based Polysilsesquioxane Nanoparticles for Photodynamic Therapy of Cancer Cells.* Int J Mol Sci, 2015. **17**(1).
231. Vivero-Escoto, J.L. and D.L. Vega, *Stimuli-responsive protoporphyrin IX silica-based nanoparticles for photodynamic therapy in vitro.* RSC Adv., 2014. **4**(28): p. 14400-14407.
232. Vivero-Escoto, J., et al., *Porphyrin-based polysilsesquioxane nanoparticles to improve photodynamic therapy for cancer treatment*. SPIE BiOS. Vol. 8931. 2014: SPIE.
233. Lyles, Z.K., et al., *Biodegradable Silica-Based Nanoparticles with Improved and Safe Delivery of Protoporphyrin IX for the In Vivo Photodynamic Therapy of Breast Cancer.* Advanced Therapeutics, 2020. **3**(7): p. 2000022.
234. Reiners, J.J., et al., *Assessing autophagy in the context of photodynamic therapy.* Autophagy, 2010. **6**(1): p. 7-18.
235. Rubio, N., et al., *p38(MAPK)-regulated induction of p62 and NBR1 after photodynamic therapy promotes autophagic clearance of ubiquitin aggregates and reduces reactive oxygen species levels by supporting Nrf2-antioxidant signaling.* Free Radic Biol Med, 2014. **67**: p. 292-303.
236. Dixon, S.J., et al., *Ferroptosis: an iron-dependent form of nonapoptotic cell death.* Cell, 2012. **149**(5): p. 1060-72.
237. Wang, S., et al., *A mini-review and perspective on ferroptosis-inducing strategies in cancer therapy.* Chinese Chemical Letters, 2019. **30**(4): p. 847-852.
238. Li, J., et al., *PDT-Enhanced Ferroptosis by a Polymer Nanoparticle with pH-Activated Singlet Oxygen Generation and Superb Biocompatibility for Cancer Therapy.* Biomacromolecules, 2021. **22**(3): p. 1167-1176.
239. Gao, M., et al., *Triggered ferroptotic polymer micelles for reversing multidrug resistance to chemotherapy.* Biomaterials, 2019. **223**: p. 119486.
240. Gomes, A., E. Fernandes, and J.L.F.C. Lima, *Fluorescence probes used for detection of reactive oxygen species.* Journal of Biochemical and Biophysical Methods, 2005. **65**(2): p. 45-80.
241. Aranda, A., et al., *Dichloro-dihydro-fluorescein diacetate (DCFH-DA) assay: A quantitative method for oxidative stress assessment of nanoparticle-treated cells.* Toxicology in Vitro, 2013. **27**(2): p. 954-963.
242. Saxena, S., et al., *Connective tissue fibroblasts from highly regenerative mammals are refractory to ROS-induced cellular senescence.* Nat Commun, 2019. **10**(1): p. 4400.
243. Drummen, G.P.C., et al., *C11-BODIPY581/591, an oxidation-sensitive fluorescent lipid peroxidation probe: (micro)spectroscopic characterization and validation of methodology.* Free Radical Biology and Medicine, 2002. **33**(4): p. 473-490.
244. Indran, I.R., et al., *Recent advances in apoptosis, mitochondria and drug resistance in cancer cells.* Biochimica et Biophysica Acta (BBA) - Bioenergetics, 2011. **1807**(6): p. 735-745.
245. Li, B., et al., *Emerging mechanisms and applications of ferroptosis in the treatment of resistant cancers.* Biomed Pharmacother, 2020. **130**: p. 110710.
246. Siano, P., et al., *Evaluation of Polyhedral Oligomeric Silsesquioxane Porphyrin Derivatives on Photodynamic Therapy.* Molecules, 2020. **25**(21).

247. Rocca, J.D., et al., *Polysilsesquioxane nanoparticles for triggered release of cisplatin and effective cancer chemoradiotherapy.* Nanomedicine: Nanotechnology, Biology and Medicine, 2015. **11**(1): p. 31-38.
248. Wang, M.-R., et al., *An efficient S-NO-polysilsesquioxane nano-platform for the co-delivery of nitric oxide and an anticancer drug.* Chemical Communications, 2015. **51**(86): p. 15649-15652.
249. Rocca, J., et al., *Polysilsesquioxane Nanoparticles for Targeted Platin-Based Cancer Chemotherapy by Triggered Release.* Angewandte Chemie (International ed. in English), 2011. **50**: p. 10330-4.
250. Li, Z., et al., *Robust Photodynamic Therapy Using 5-ALA-Incorporated Nanocomplexes Cures Metastatic Melanoma through Priming of CD4(+)CD8(+) Double Positive T Cells.* Advanced Science, 2019. **6**(5): p. 18.
251. Chiu, S.M. and N.L. Oleinick, *Dissociation of mitochondrial depolarization from cytochrome c release during apoptosis induced by photodynamic therapy.* Br J Cancer, 2001. **84**(8): p. 1099-106.
252. Xue, L.-y., S.-m. Chiu, and N.L. Oleinick, *Photochemical destruction of the Bcl-2 oncoprotein during photodynamic therapy with the phthalocyanine photosensitizer Pc 4.* Oncogene, 2001. **20**(26): p. 3420-3427.
253. Kessel, D., *Promotion of PDT efficacy by a Bcl-2 antagonist.* Photochemistry and photobiology, 2008. **84**(3): p. 809-814.
254. Juneja, R., et al., *Combination of Nucleic Acid and Mesoporous Silica Nanoparticles: Optimization and Therapeutic Performance In Vitro.* ACS Appl Mater Interfaces, 2020. **12**(35): p. 38873-38886.
255. Wang, F., A. Salvati, and P. Boya, *Lysosome-dependent cell death and deregulated autophagy induced by amine-modified polystyrene nanoparticles.* 2018. **8**(4): p. 170271.
256. Akter, S., et al., *Photodynamic therapy by lysosomal-targeted drug delivery using talaporfin sodium incorporated into inactivated virus particles.* Laser Ther, 2019. **28**(4): p. 245-256.
257. Boya, P. and G. Kroemer, *Lysosomal membrane permeabilization in cell death.* Oncogene, 2008. **27**(50): p. 6434-51.
258. Girotti, A.W., *Photosensitized oxidation of membrane lipids: reaction pathways, cytotoxic effects, and cytoprotective mechanisms.* Journal of Photochemistry and Photobiology B-Biology, 2001. **63**(1-3): p. 103-113.
259. Farmer, E.E. and M.J. Mueller, *ROS-Mediated Lipid Peroxidation and RES-Activated Signaling.* Annual Review of Plant Biology, 2013. **64**(1): p. 429-450.
260. Suryo Rahmanto, A., D.I. Pattison, and M.J. Davies, *Photo-oxidation-induced inactivation of the selenium-containing protective enzymes thioredoxin reductase and glutathione peroxidase.* Free Radic Biol Med, 2012. **53**(6): p. 1308-16.
261. Homma, T., S. Kobayashi, and J. Fujii, *Induction of ferroptosis by singlet oxygen generated from naphthalene endoperoxide.* Biochemical and Biophysical Research Communications, 2019. **518**(3): p. 519-525.
262. Zilka, O., et al., *On the Mechanism of Cytoprotection by Ferrostatin-1 and Liproxstatin-1 and the Role of Lipid Peroxidation in Ferroptotic Cell Death.* ACS Central Science, 2017. **3**(3): p. 232-243.
263. Castano, A.P., T.N. Demidova, and M.R. Hamblin, *Mechanisms in photodynamic therapy: part two-cellular signaling, cell metabolism and modes of cell death.* Photodiagnosis and photodynamic therapy, 2005. **2**(1): p. 1-23.
264. Inguscio, V., E. Panzarini, and L. Dini, *Autophagy Contributes to the Death/Survival Balance in Cancer PhotoDynamic Therapy.* Cells, 2012. **1**(3): p. 464-491.
265. Yun, H.R., et al., *Roles of Autophagy in Oxidative Stress.* International journal of molecular sciences, 2020. **21**(9): p. 3289.

266. Martins, W.K., et al., *Autophagy Regulation and Photodynamic Therapy: Insights to Improve Outcomes of Cancer Treatment.* Frontiers in oncology, 2021. **10**: p. 610472-610472.
267. Shaid, S., et al., *Ubiquitination and selective autophagy.* Cell Death & Differentiation, 2013. **20**(1): p. 21-30.
268. Yang, Z. and D.J. Klionsky, *An overview of the molecular mechanism of autophagy.* Current topics in microbiology and immunology, 2009. **335**: p. 1-32.
269. Lim, S.M., E.A. Mohamad Hanif, and S.-F. Chin, *Is targeting autophagy mechanism in cancer a good approach? The possible double-edge sword effect.* Cell & Bioscience, 2021. **11**(1): p. 56.
270. Muchowicz, A., et al., *Proteasome Inhibition Potentiates Antitumor Effects of Photodynamic Therapy in Mice through Induction of Endoplasmic Reticulum Stress and Unfolded Protein Response.* Cancer research, 2009. **69**: p. 4235-43.
271. Zuluaga, M.-F. and N. Lange, *Combination of Photodynamic Therapy with Anti-Cancer Agents.* Current medicinal chemistry, 2008. **15**: p. 1655-73.
272. Yang, Y.-L., K. Lin, and L. Yang, *Progress in Nanocarriers Codelivery System to Enhance the Anticancer Effect of Photodynamic Therapy.* Pharmaceutics, 2021. **13**(11): p. 1951.
273. Juan, L.V.-E., et al. *Porphyrin-based polysilsesquioxane nanoparticles to improve photodynamic therapy for cancer treatment*. in *Proc.SPIE*. 2014.
274. Vega, D.L., P. Lodge, and J.L. Vivero-Escoto, *Redox-Responsive Porphyrin-Based Polysilsesquioxane Nanoparticles for Photodynamic Therapy of Cancer Cells.* International Journal of Molecular Sciences, 2016. **17**(1): p. 56.
275. Dib, S., et al., *Porphyrin-based bridged silsesquioxane nanoparticles for targeted two-photon photodynamic therapy of zebrafish xenografted with human tumor.* Cancer Reports, 2019. **2**(5): p. e1186.
276. Gutierrez, E., D.R. Richardson, and P.J. Jansson, *The anticancer agent di-2-pyridylketone 4,4-dimethyl-3-thiosemicarbazone (Dp44mT) overcomes prosurvival autophagy by two mechanisms: persistent induction of autophagosome synthesis and impairment of lysosomal integrity.* The Journal of biological chemistry, 2014. **289**(48): p. 33568-33589.
277. Chen, S., et al., *Targeting SQSTM1/p62 induces cargo loading failure and converts autophagy to apoptosis via NBK/Bik.* Molecular and cellular biology, 2014. **34**(18): p. 3435-3449.
278. Mauthe, M., et al., *Chloroquine inhibits autophagic flux by decreasing autophagosome-lysosome fusion.* Autophagy, 2018. **14**(8): p. 1435-1455.
279. Catalani, E., et al., *Oxidative Stress and Autophagy as Key Targets in Melanoma Cell Fate.* Cancers, 2021. **13**(22): p. 5791.
280. Rubio, N., et al., *Spatiotemporal autophagic degradation of oxidatively damaged organelles after photodynamic stress is amplified by mitochondrial reactive oxygen species.* Autophagy, 2012. **8**(9): p. 1312-1324.
281. Rodríguez, M.E., et al., *A novel HIF-1α/VMP1-autophagic pathway induces resistance to photodynamic therapy in colon cancer cells.* Photochem Photobiol Sci, 2017. **16**(11): p. 1631-1642.
282. Vadarevu, H., et al., *Light-Activated Protoporphyrin IX-Based Polysilsesquioxane Nanoparticles Induce Ferroptosis in Melanoma Cells.* Nanomaterials (Basel, Switzerland), 2021. **11**(9): p. 2324.
283. Bharathiraja, S., et al., *Chlorin e6 conjugated silica nanoparticles for targeted and effective photodynamic therapy.* Photodiagnosis and Photodynamic Therapy, 2017. **19**: p. 212-220.
284. Lv, J., et al., *Mitochondria-targeting multifunctional nanoplatform for cascade phototherapy and hypoxia-activated chemotherapy.* Journal of Nanobiotechnology, 2022. **20**(1): p. 42.
285. Sundaram, P. and H. Abrahamse, *Effective Photodynamic Therapy for Colon Cancer Cells Using Chlorin e6 Coated Hyaluronic Acid-Based Carbon Nanotubes.* Int J Mol Sci, 2020. **21**(13).

286. Juneja, R., et al., *Multimodal Polysilsesquioxane Nanoparticles for Combinatorial Therapy and Gene Delivery in Triple-Negative Breast Cancer.* ACS Applied Materials & Interfaces, 2019. **11**(13): p. 12308-12320.
287. Vivero-Escoto, J.L., et al., *Biodegradable polysilsesquioxane nanoparticles as efficient contrast agents for magnetic resonance imaging.* Small (Weinheim an der Bergstrasse, Germany), 2013. **9**(20): p. 3523-3531.
288. Gilson, R.C., et al., *Trafficking of a Single Photosensitizing Molecule to Different Intracellular Organelles Demonstrates Effective Hydroxyl Radical-Mediated Photodynamic Therapy in the Endoplasmic Reticulum.* Bioconjugate chemistry, 2019. **30**(5): p. 1451-1458.
289. Luo, W., et al., *Subcellular location and photodynamic therapeutic effect of chlorin e6 in the human tongue squamous cell cancer Tca8113 cell line.* Oncology letters, 2015. **9**(2): p. 551-556.
290. Yoo, J.-O., et al., *Differential cytotoxic responses to low- and high-dose photodynamic therapy in human gastric and bladder cancer cells.* Journal of Cellular Biochemistry, 2011. **112**(10): p. 3061-3071.
291. Kroemer, G., L. Galluzzi, and C. Brenner, *Mitochondrial Membrane Permeabilization in Cell Death.* Physiological Reviews, 2007. **87**(1): p. 99-163.
292. Boya, P. and G. Kroemer, *Lysosomal membrane permeabilization in cell death.* Oncogene, 2008. **27**(50): p. 6434-6451.
293. Colturato-Kido, C., et al., *Inhibition of Autophagy Enhances the Antitumor Effect of Thioridazine in Acute Lymphoblastic Leukemia Cells.* Life, 2021. **11**(4).
294. Perez-Neut, M., et al., *Activation of hERG3 channel stimulates autophagy and promotes cellular senescence in melanoma.* Oncotarget; Vol 7, No 16, 2016.
295. Gump, J. and A. Thorburn, *Soting cells for basal and induced autophagic flux by quantitative ratiometric flow cytometry.* Autophagy, 2014. **10**.
296. Kim, S., S. Choi, and D. Kang, *Quantitative and qualitative analysis of autophagy flux using imaging.* BMB reports, 2020. **53**(5): p. 241-247.
297. Lovejoy, D.B., et al., *Antitumor activity of metal-chelating compound Dp44mT is mediated by formation of a redox-active copper complex that accumulates in lysosomes.* Cancer Res, 2011. **71**(17): p. 5871-80.
298. Mrozek-Wilczkiewicz, A., et al., *Iron Chelators and Exogenic Photosensitizers. Synergy through Oxidative Stress Gene Expression.* J Cancer, 2017. **8**(11): p. 1979-1987.
299. Nihira, K., et al., *An inhibition of p62/SQSTM1 caused autophagic cell death of several human carcinoma cells.* Cancer science, 2014. **105**(5): p. 568-575.
300. Tsikas, D., *Assessment of lipid peroxidation by measuring malondialdehyde (MDA) and relatives in biological samples: Analytical and biological challenges.* Anal Biochem, 2017. **524**: p. 13-30.
301. Zhu, T., et al., *Ferroptosis Promotes Photodynamic Therapy: Supramolecular Photosensitizer-Inducer Nanodrug for Enhanced Cancer Treatment.* Theranostics, 2019. **9**(11): p. 3293-3307.
302. Dewaele, M., et al., *Autophagy pathways activated in response to PDT contribute to cell resistance against ROS damage.* Journal of cellular and molecular medicine, 2011. **15**(6): p. 1402-1414.